Rotational Symmetry and Phase Dynamics in Topological Superconductors

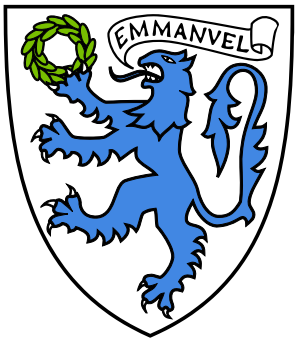

Elis Ifor Roberts

Supervisor: Prof. Benjamin Béri

Department of Physics
University of Cambridge

This thesis is submitted for the degree of
Doctor of Philosophy

Emmanuel College

November 2022

Declaration

This thesis is the result of my own work and includes nothing which is the outcome of work done in collaboration except as declared in the preface and specified in the text. It is not substantially the same as any work that has already been submitted, or is being concurrently submitted, for any degree, diploma or other qualification at the University of Cambridge or any other University or similar institution except as declared in the preface and specified in the text. It does not exceed the prescribed word limit for the relevant Degree Committee.

Elis Ifor Roberts
November 2022

Abstract

Topological superconductors are phases of matter that cannot be adiabatically connected to a trivial superconductor without closing the bulk gap or breaking some fundamental symmetry. Intimately tied to topological superconductors are Majorana bound states. These are neutral zero-energy quasiparticles, localised to boundaries or defects, that are highly sought after as ingredients for quantum computation.

In the first part of this thesis, we consider two-dimensional crystalline superconductors with discrete rotational symmetry. These can host zero-dimensional Majorana bound states at their corners, indicative of so-called second-order topology. We establish a bulk-boundary correspondence linking the presence of such Majorana bound states to bulk topological invariants based on momentum-space rotation representations. We thus establish when a topological crystalline superconductor protected by rotational symmetry displays second-order topological superconductivity. Our approach is based on stacked Dirac Hamiltonians, using which we relate transitions between topological phases to the transformation properties between adjacent gapped boundaries. We find that in addition to the bulk rotational invariants, the presence of Majorana bound states in a given geometry depends on the interplay between weak topological invariants and the location of the rotation centre relative to the lattice.

In the second part of the thesis, we couple a quantum particle to a topology-changing fermionic bath. Generically, coupling to a bath suppresses the particle's amplitude to tunnel between potential minima, even at zero temperature. While this effect can be neglected for gapped baths, our bath has minima that correspond to different bath topologies. This enforces the bath to undergo gap closing along the tunnelling path. We develop a field theory for this quantum tunnelling problem, linking the instantons describing tunnelling in a bath of d space dimensions to topological boundary modes of systems in $d+1$ dimensions. We study in detail a $d = 1$ example, inspired by planar Josephson junctions where the particle coordinate is the superconducting phase whose value sets the electronic topology. We find that the topology change suppresses tunnelling by a factor scaling exponentially with the system size. This translates to a correspondingly enhanced suppression of the energy splitting for the lowest-lying states, despite these being linear combinations of states near potential minima where the bath is gapped. Our results help to estimate the influence of charging

energy on topological phases arising due to the Josephson effect and, conversely, to assess the potential utility of such topological systems as superconducting qubits. For moderate-sized baths, the incomplete suppression of tunnelling opens the prospect of quantum-mechanical superpositions of many-body states of different topology, including superpositions of states with and without Majorana fermions.

i'm rhieni

Acknowledgements

First and foremost, I would like to thank Benjamin for his formative guidance and support during my PhD. I have benefited immensely from his insightful wisdom, patience and thoughtfulness as a mentor. I always left meetings with fresh perspectives and optimism about things I had been struggling with. I am especially grateful to him for opening my eyes to what differentiates good scientific writing from bad and how much I still have to learn in this regard. I appreciate his and the EPSRC's faith in me as a researcher.

Alongside Benjamin, I have received endless support from my collaborator and friend, Jan. He always met my requests for help with helpful explanations, technical insight and humour. I also thank him for allowing me privileged access to *The Universe in a Python Script*—`models3.py`. A further thanks goes to him and Ollie for proofreading the introduction of this thesis at short notice.

TCM has been a wonderful environment to study physics. Among many interesting seminars were Dima's reliably enjoyable morning lectures, which I appreciate. I am also obliged to Michael Rutter for his computing support and accommodation of my fussy need for high-resolution displays. The coffee area was also a consistent source of interesting conversation, for which I thank Danny, Angela, Michael, Clara, Andrea, Simon, Jack, Benji, Ivona, Pieter, Andrew and numerous others. In particular, I am grateful to Ollie, Max and Alice for their friendship during afternoon snack breaks and outside.

Beyond TCM, my life has been enriched by many others. Wednesdays were characterised by the food vans crew including Olivia, Leon and Ben. These also featured my good friend Taketomo, there since the NatSci days, who introduced me to the entertaining spectacle that is the Molecular Engineering group. Even further from physics, I am indebted to Emmanuel College Boat Club for being integral to my years at Cambridge and exposing me to the fulfilment that endurance sports can bring. I attribute many especially fond memories to the Mays crew of 2022.

Thanks also to Batuhan, Callum and Basil for their camaraderie during lockdown and beyond. Your absence would have made the pandemic much less tolerable. I am also deeply grateful to Lara for making my last year at Cambridge a joy, and for hosting me as I wrote parts of this thesis.

Underpinning all that I have enjoyed in life is the support and love of my family. *Diolch i Mam, Dad, Iddon a gweddill fy nheulu am bopeth. Caru chi.*

Table of contents

List of figures xv

List of tables xvii

1 Introduction 1
- 1.1 Topological Classification of Superconductors . . . 2
  - 1.1.1 Topology in Free Fermion Systems . . . 4
  - 1.1.2 Bogoliubov-de-Gennes Hamiltonians . . . 6
  - 1.1.3 Majorana Zero Modes . . . 7
  - 1.1.4 Crystalline Symmetry Enriched Topological Classification . . . 14
  - 1.1.5 Higher-Order Topology . . . 22
- 1.2 Practical Aspects of Topological Superconductors . . . 24
  - 1.2.1 Charging Energy in Mesoscopic Superconductors . . . 25
- 1.3 Tunnelling and Instantons . . . 29
  - 1.3.1 Euclidean Solutions . . . 29
  - 1.3.2 The Dilute Instanton Gas for Periodic Potentials . . . 32
- 1.4 Thesis Outline . . . 37

2 Second-order bulk-boundary correspondence in rotationally symmetric topological superconductors 39
- 2.1 Motivation . . . 39
- 2.2 Bulk Topological Classification . . . 41
  - 2.2.1 Importance of Rotation Centre . . . 44
- 2.3 Stacked Dirac Models and Boundary Theory . . . 49
  - 2.3.1 Stacked Dirac Models . . . 49
  - 2.3.2 Rotation Eigenvalues and Signed Representations . . . 50
  - 2.3.3 Dirac Stacks for Topological Interfaces . . . 53
  - 2.3.4 Effective Edge Theory . . . 55

2.3.5 Boundary Mass Terms . . . 57
2.4 Bulk Rotation Invariants and Corner Majoranas . . . 60
2.4.1 Path Independence . . . 61
2.4.2 Constructing Topological Index for Corner States . . . 62
2.5 Other Rotational Symmetries . . . 64
2.5.1 Twofold Symmetry . . . 65
2.5.2 Sixfold Symmetry . . . 66
2.5.3 Other Rotation Representations for the Superconducting Order Parameter . . . 67
2.6 Examples . . . 69
2.7 Conclusion . . . 72

3 Quantum tunnelling in the presence of a topology-changing fermionic bath 75
3.1 Motivation . . . 75
3.2 Model . . . 77
3.3 Tunnelling and Instantons . . . 79
3.3.1 Path Integral . . . 80
3.3.2 The Instanton Gas . . . 80
3.3.3 Integrating Out Fermions . . . 83
3.4 Tunnelling Suppression via Topology in $d+1$ Dimensions . . . 84
3.4.1 Sharp Instanton Limit . . . 85
3.5 Tunnelling Suppression from a Variational Approach . . . 90
3.5.1 Fermionic Factor as a Generalisation of the Ground State Potential . . . 90
3.5.2 Variational Instanton Strategy . . . 92
3.5.3 Evaluating Time-Ordered Exponentials with Scattering Matrices . . . 94
3.5.4 Results . . . 97
3.6 Conclusion . . . 99

4 Summary and Outlook 103

References 107

Appendix A Additional Derivations for Bulk-Boundary Correspondence 117
A.1 Restrictions on Choice of Unit Cell . . . 117
A.2 Derivation of The Edge Theory . . . 120
A.2.1 Effective Boundary Hamiltonian . . . 120
A.2.2 Surface Projections of Rotation Representations . . . 122

A.2.3 Edge Projection of Particle-Hole Operator 124

Appendix B Additional Proofs about The Fermionic Determinant 127

B.1 Jackiw-Rebbi Derivation of Edge Mode Spectrum 127

B.2 Proof that Fermions Guarantee Suppression 129

List of figures

1.1 Topologically inequivalent dimerised limits of the Kitaev chain. 9
1.2 Kitaev chains with periodic boundary conditions. 11
1.3 Chiral Dirac modes in a Corbino disc geometry. 14
1.4 Wyckoff positions and Brillouin zone for a p2mm wallpaper group. 18
1.5 Symmetric deformation between two high-symmetry point Hamiltonians. . 19
1.6 Compatibility relations example in a wallpaper group. 20
1.7 Codimensionality of higher-order gapless surface states. 23
1.8 Circuit diagram and spectrum of a Cooper pair box. 28
1.9 Effect of offset charge on the spectrum of a Cooper pair box. 29
1.10 One-dimensional barrier potential. 30
1.11 Inverted cosine potential and the instanton solution. 34
1.12 Typical phase profile in the dilute instanton gas approximation. 35

2.1 Brillouin zone for C_4-symmetric models. 42
2.2 Rotation eigenvalues for C_2 and C_4 symmetry. 43
2.3 Options for the rotation centre in a C_4-symmetric lattice. 45
2.4 Typical edge spectrum of a 2D superconductor. 56
2.5 Brillouin zone for C_2- and C_6-symmetric models. 64
2.6 Phase diagram for a C_4-symmetric superconductor on a lattice. 70
2.7 Low energy spectrum for a C_4-symmetric superconductor on a lattice. . . . 71
2.8 Finite lattice models with two different fourfold rotation centres. 72

3.1 Single-particle energies of a phase-controlled 1D Kitaev chain. 78
3.2 Edge modes for an instanton-anti-instanton with antiperiodic boundary conditions. 86
3.3 Edge modes for an instanton-anti-instanton with open boundary conditions. 87
3.4 Plot of effective potential in the action after accounting for eigenstate evolution. 93

3.5 Scaling of tunnelling amplitude with system size for phase-controlled Kitaev chain. 97
3.6 Schematic of a superposition between topologically inequivalent ground states. 101

A.1 C_4-symmetric lattices with different rotation centres. 120

List of tables

2.1 Correspondence between fourfold rotation eigenvalues and bulk masses and rotation representations. 51
2.3 Correspondence between representations at fourfold fixed points for C_4 symmetries with different centres. 57
2.4 Correspondence between representations at twofold fixed points for C_4 symmetries with different centres. 57
2.5 Relation between bulk and edge rotation representations. 58

Chapter 1

Introduction

Phases of matter are familiar to all of us. In our daily lives, it is obvious that ice cubes from a freezer at $-18°$C are indistinguishable from those kept at $-17°$C, but very distinguishable from what comes out of a $5°$C refrigerator. That water and other classical matter exist in distinct stable phases depending on their temperature and pressure was understood early on. With the development of quantum mechanics, however, it became evident that there are phases of matter that have macroscopic properties inconsistent with any classical description.

Superconductors are one such example. Below a certain temperature, they manage to evade dissipation and conduct current with zero resistance. Superfluidity and Bose-Einstein condensation are other exotic examples. In all these cases, the rules of quantum mechanics that apply to the constituent particles cannot be detached from the mechanism by which the phases form. This is even true of ferromagnetism, which we encounter at room temperature. A unified framework for understanding both quantum and classical phases was provided by Landau with the concept of spontaneous symmetry breaking. In this framework the underlying Hamiltonian, which governs the dynamics of all degrees of freedom, has a particular symmetry, whereas states in different phases have a different (lower) symmetry. When water is in liquid form, its molecules do not have fixed relative position: at any instant, the molecules are randomly distributed and the liquid looks the same when displaced by an arbitrary distance. In this sense a liquid has continuous translational symmetry, which is shared by the Hamiltonian because the rules of electromagnetism are homogenous. Contrast this to ice, where molecules are arranged in a regular lattice such that it is invariant only when translated by a discrete lattice vector. Solids therefore have discrete translational symmetry unlike the Hamiltonian, and transitioning from a liquid to a solid counts as spontaneous symmetry breaking. The same principles of identifying broken symmetries to classify phases apply to all of the systems above. For example, in a superconducting phase it is the global $\mathrm{U}(1)$ gauge symmetry that is broken. The success of this theory led physicists to believe that

symmetry breaking could explain phase transitions in all contexts. Yet, at zero temperature there turn out to be distinct quantum phases of matter that have the *same* symmetry. The difference instead lies in the pattern of entanglement in their ground states, and can be differentiated by borrowing concepts from topology.

Topology is a branch of mathematics that concerns itself with properties of objects that are preserved under continuous deformation. When this object is geometrical, such deformations can be anything that doesn't involve tearing, gluing or passing the object through itself. With a more flexible notion of 'continuous deformation', one can study topology in other contexts, even physical systems. The philosophy of studying 'topological phases of matter' is to apply topology to the many-body ground state $|\Omega\rangle$, relevant to gapped quantum systems near zero temperature. (We interchangeably label a gapped system by its Hamiltonian or ground state, depending on which is convenient.) The aim is to gather up systems into equivalence classes based on which systems—composed of fermions or bosons in a certain dimension—are continuously deformable into each other, labelled by *topological invariants* that one can calculate from the quantum states. What is remarkable is that systems that are *topologically equivalent* also have qualitatively similar experimental observables, which justifies thinking of them as *quantum phases of matter*.

In this thesis, we are interested in superconductors that can simultaneously be topological phases of matter. These have many potential exciting consequences, particularly in quantum information, and their realisation is a major goal of modern condensed matter physics. We will elucidate two separate links between topological nontriviality in superconductors and observable features, with relevance to modern experimental platforms.

1.1 Topological Classification of Superconductors

The labelling of a phase as 'topological' can have many different meanings in condensed matter physics, but in this thesis it will have one meaning that we now try to place in context. The first thing to point out is that we must narrow our considerations to a privileged class of quantum states; otherwise, any two states in a Hilbert space can be trivially deformed into each other by taking a linear superposition interpolating between the two that necessarily lives in the same space. All states are therefore connected when there are no restrictions.

One sensible restriction is to states that are the ground states of gapped local Hamiltonians.[1] The ground states of these systems satisfy an *area law* of entanglement [2] saying that

[1] Being 'gapped' has the precise definition of a sequence of Hamiltonians approaching the thermodynamic limit possessing no eigenvalues in a certain energy window [1]. This is needed because any finite system has a discrete spectrum and hence a gap in the naïvest sense. We keep in mind only the principle of this proper definition, however.

entanglement entropy between a subregion $\mathcal{A}$ and its contiguous complement $\bar{\mathcal{A}}$ grows at most linearly with the size of the boundary of $\mathcal{A}$, which immediately places many restrictions on the state. Interpolating between two generic states may therefore necessitate passing through a state that cannot be the ground state of a gapped local Hamiltonian, which provides a way for this space to be disconnected and nontrivial. Each disconnected component is called a *phase*, and a phase transition necessarily comes with a gap closing. Consider two states $|\Omega_0\rangle$ and $|\Omega_1\rangle$ that are the ground states of gapped local Hamiltonians $\hat{H}_0$ and $\hat{H}_1$, respectively. Expressed in terms of their Hamiltonians, these are in the same phase if there is a smooth path $\hat{H}_t$ for $0 \leq t \leq 1$ connecting them, such that $\hat{H}_t$ remains gapped and local throughout. This means $|\Omega_0\rangle$ and $|\Omega_1\rangle$ are connected through an adiabatic evolution that does not close the gap.[2] In Chen *et al.*'s definition, there is one phase that stands out as trivial, namely the *short-range entangled* (SRE) phase containing states connected to an unentangled direct-product state in real space. The remaining states (still satisfying an area law) are called *long-range entangled* (LRE), and their equivalence classes map out the *topological order*. Topologically ordered states can host phenomena such as fractional charge, anyons with non-Abelian exchange statistics, ground state degeneracy (that depends on the topology of the underlying manifold, e.g., the genus in two dimensions) or gapless edge excitations [4, 1]. This is not the topology of interest in this thesis, however, because we require an extra ingredient: *symmetry*.

Many condensed matter systems possess symmetries—be they fine-tuned or not—so rather than consider states of otherwise arbitrary gapped local Hamiltonians, one can restrict oneself to Hamiltonians that have certain symmetries. One then redefines equivalence to be in terms of smooth paths $\hat{H}_t$ that remain gapped and *possess the same symmetry* throughout. Under this definition, ground states can be in different phases even if they do not spontaneously break a symmetry of the system, going beyond Landau's classification. The nontrivial SRE phases that do not break a symmetry of the system are called *symmetry-protected topological* (SPT) phases since they could all be connected to a product state if the symmetry requirement on adiabatic evolution were relaxed. In this sense, SPT phases are less robust, but still possess interesting phenomena such as gapless edge excitations.

The taxonomy we have discussed thus far has applied equally to *interacting* Hamiltonians, so long as the interactions are local. From now on, however, we will only be discussing the topology of *non-interacting* Hamiltonians involving fermions, i.e., 'free-fermion SPTs' according to the above terminology. Since the properties of these systems are entirely captured

[2] This adiabatic evolution is generated by unitary evolution under a different local Hamiltonian $\hat{H}'_t$, $|\Omega_1\rangle = \mathcal{T}[e^{-i\int_0^1 dt\, \hat{H}'_t}]|\Omega_0\rangle$ (where $\mathcal{T}$ denotes time-ordering), which is a more practical condition for distinguishing SRE states from LRE states (defined below) [3].

by single-particle Hamiltonian matrices, their classification is much easier and, in some ways, complete. This classification scheme also extends to BCS superconductors with minimal modification by treating the Bogoliubov-de-Gennes (BdG) Hamiltonian on the same level as a single-particle Hamiltonian, even though superconductivity derives from interaction.[3]

1.1.1 Topology in Free Fermion Systems

The integer quantum Hall effect (IQHE) was the first condensed matter system whose properties were found to be topological in origin, occurring for a two-dimensional (2D) electron gas in the presence of a magnetic field [7]. The quantised Hall conductance was explained by an integer topological invariant called the *Chern number* that can be calculated solely from the single-particle eigenstates [8]. The fundamental quantity of this invariant (and many others) is the non-Abelian *Berry connection*—a differential 1-form—defined[4] for Bloch eigenstates,[5] $|u^\alpha(\mathbf{k})\rangle$, as [10]

$$\mathcal{A}^{\alpha\beta} = \langle u^\alpha(\mathbf{k})|du^\beta(\mathbf{k})\rangle = \langle u^\alpha(\mathbf{k})|\nabla_{\mathbf{k}} u^\beta(\mathbf{k})\rangle \cdot d\mathbf{k} \equiv \sum_i \mathcal{A}_i^{\alpha\beta}\, dk^i, \tag{1.1}$$

where the band indices α, β run over *occupied* bands only. From this, one may define a gauge-invariant *Berry curvature*

$$\mathcal{F}^{\alpha\beta} = d\mathcal{A}^{\alpha\beta} + (\mathcal{A}\wedge\mathcal{A})^{\alpha\beta} = \sum_{ij} (\partial_{k^i}\mathcal{A}_j - \partial_{k^j}\mathcal{A}_i + [\mathcal{A}_i, \mathcal{A}_j])^{\alpha\beta}\, dk^i \wedge dk^j \tag{1.2}$$

where $\wedge$ denotes the exterior product (an antisymmetric product of differential forms). The first Chern number is then given by integrating the diagonal components of the Berry curvature over the first Brillouin zone (BZ)

$$\mathrm{Ch} = \frac{i}{2\pi}\int_{\mathrm{BZ}} \mathrm{Tr}\{\mathcal{F}\} \in \mathbb{Z}. \tag{1.3}$$

Since the IQHE, nontrivial topology has been found to be much more ubiquitous than originally thought following the discovery of topological insulators (TIs) with spin-orbit

[3] Tangentially, Wen noticed that all realistic superconductors are technically LRE when coupled to a dynamical electromagnetic gauge field because they lack a gauge-invariant local order parameter [6], but this is not what we mean when we label our superconductors as topological.

[4] Strong topological invariants are most easily expressed in momentum space, even though their protection does not hinge on translation symmetry. There are also *weak* invariants, encountered in Chapter 2, where translation symmetry is actually necessary [9].

[5] In this basis $\hat{H} = \sum_{\mathbf{k}\in\mathrm{BZ}} \sum_{\alpha\beta} \hat{c}^\dagger_\alpha(\mathbf{k})\, \mathcal{H}_{\alpha\beta}(\mathbf{k})\, \hat{c}_\beta(\mathbf{k})$ and $\mathcal{H}(\mathbf{k})|u^\alpha(\mathbf{k})\rangle = E_\alpha|u^\alpha(\mathbf{k})\rangle$, which are periodic upon adding reciprocal lattice vectors $\mathbf{k} \to \mathbf{k}+\mathbf{G}$.

coupling [9, 11, 12]. These materials can have topological invariants that, although definable in terms of the Berry connection, are very different from the Chern number. These are namely the $\mathbb{Z}_2$-valued first- and second-descendant invariants [13]. In fact, the group structure of the invariants follows directly from a system's dimension and behaviour under some fundamental non-spatial (antiunitary) symmetries: time-reversal (TR), particle-hole (PH) and chiral symmetry.[6] These define an Altland-Zirnbauer (AZ) symmetry class [14]. The symmetry classes and associated group structures are mapped out exhaustively in the *tenfold way*, acting as a "periodic table" of topological insulators and superconductors which was a great triumph in the field [15–18]. This table has its own rich structure that we will not be exposed to because our later chapters involve only one or two symmetry classes.

A key tenet of this table is that the classification is stable under the addition of trivial bands, which means that all of the groups are Abelian under stacking, i.e., under $\mathcal{H}_0 \oplus \mathcal{H}_1 = \begin{bmatrix} \mathcal{H}_0 & 0 \\ 0 & \mathcal{H}_1 \end{bmatrix}$. Trivial bands correspond to insulators in their atomic limit such that they have no structure in momentum space, being examples of the direct-product states mentioned in Sec. 1.1. The motivation for this condition is that real materials, with their many core and unfilled atomic orbitals, can have bands far below or above the Fermi energy; these could in principle get closer to the Fermi energy and hybridise with the relevant bands as the Hamiltonian is deformed. Concretely, two Hamiltonians $\mathcal{H}_0$ and $\mathcal{H}_1$ are *stably equivalent* if there exist some trivial bands $\mathcal{E}_0$ and $\mathcal{E}_1$ such that $\mathcal{H}_0 \oplus \mathcal{E}_0$ is strictly equivalent to $\mathcal{H}_1 \oplus \mathcal{E}_1$. Strict equivalence between $\mathcal{H}_0$ and $\mathcal{H}_1$ that have the same number of bands requires a smooth path of symmetric Hamiltonians $\mathcal{H}_t = (1-t)\mathcal{H}_0 + t\mathcal{H}_1$ to remain gapped for $0 \leq t \leq 1$. The 'gap' being preserved here is the finite energy difference between the νth and $(\nu+1)$th bands, where the Fermi energy lies. Requiring stability means that the appropriate 'difference' between Hamiltonians is captured through the mathematics of what is called K-theory [17].

The main reason that the tenfold way invariants are of immense interest is the *bulk-boundary correspondence*, which guarantees gapless states at the boundaries of systems that have topologically nontrivial bulk invariants [10]. In some ways, this correspondence is not surprising: we have presented topological inequivalence as an obstruction to adiabatically connecting systems without closing a gap, while a boundary may be equally viewed as the variation of a parameter in space that interpolates between the bulk material and the trivial vacuum. The anomalous Hall conductance in the IQHE is itself an example of bulk-boundary correspondence because it is mediated by chiral edge states whose presence and direction are governed by the Chern number. We will soon encounter more examples extending to superconductors.

[6] These are fundamental because they classify the irreducible blocks of any Hamiltonian brought into diagonal form by a unitary symmetry [10], but we revisit this reasoning in Sec. 1.1.4 when we strongly enforce unitary symmetries.

1.1.2 Bogoliubov-de-Gennes Hamiltonians

The superconductors we encounter in this thesis will all be described at the level of BCS mean-field theory [19]. At this level, the superconducting Hamiltonian may be described by an effectively single-particle BdG Hamiltonian

$$\hat{H} = \frac{1}{2}\sum_{\alpha\beta} \hat{\xi}^\dagger_\alpha \mathcal{H}_{\alpha\beta} \hat{\xi}_\beta, \tag{1.4}$$

where $\hat{\xi}_\alpha = (\hat{c}_\alpha, \hat{c}^\dagger_\alpha)^T$ is the Nambu spinor for site/orbital α and $\mathcal{H} = \mathcal{H}^\dagger$ is a Hermitian matrix. Inherent to any BdG system is a redundancy known as *particle-hole* (PH) symmetry. This is because $\hat{\xi}_\alpha$ and $\hat{\xi}^\dagger_\alpha$ are not independent, but instead linked to each other through $(\sigma_1 \hat{\xi}_\alpha)^T = \hat{\xi}^\dagger_\alpha$, which yields the PH condition[7]

$$\sigma_1 \mathcal{H}^* \sigma_1 = -\mathcal{H}. \tag{1.5}$$

We view this as the anticommutation of $\mathcal{H}$ with an antiunitary operator $\Xi = \mathcal{K}\sigma_1$ which is a local unitary operator composed with complex conjugation $\mathcal{K}$.[8] This means that the BdG Hamiltonian may be written in block form

$$\mathcal{H} = \begin{bmatrix} H_0 & \Delta \\ -\Delta^* & -H_0^T \end{bmatrix}, \tag{1.6}$$

where $H_0 = H_0^\dagger$ represents the normal part, and $\Delta = -\Delta^T$ the pairing terms. When PH symmetry Ξ is the superconductor's only symmetry and $\Xi^2 = +1$, we say it is in Class D [10].

The PH constraint (1.5) is reflected in the excitation spectrum of the superconductor, given by the eigenvalues of $\mathcal{H}$:

$$\mathcal{H}\psi_E = E\psi_E \quad \Longrightarrow \quad \mathcal{H}(\Xi\psi_E) = -E(\Xi\psi_E). \tag{1.7}$$

That is, any eigenvector with energy E has a PH conjugate eigenvector with energy $-E$. Their corresponding Bogoliubov operators $\hat{\zeta}^\dagger_E$ (obeying fermionic anticommutation relations

[7] Pauli matrices are denoted by $\sigma_{i=1,2,3}$ throughout this thesis. Here, $\sigma_1 = \left[\begin{smallmatrix} 0 & 1 \\ 1 & 0 \end{smallmatrix}\right]$ acts on PH orbital space.

[8] One often works in momentum space with Nambu basis $\hat{\xi}_\alpha(\mathbf{k}) = (\hat{c}_\alpha(\mathbf{k}), \hat{c}^\dagger_\alpha(-\mathbf{k}))^T$, in which case the reversal of momentum $\mathbf{k}$ under PH conjugation means that the symmetry relation is instead

$$\sigma_1 \mathcal{H}^*(\mathbf{k}) \sigma_1 = -\mathcal{H}(-\mathbf{k}).$$

$\{\hat{\zeta}_E, \hat{\zeta}^\dagger_{E'}\} = \delta_{EE'}$) are not all independent either, since

$$\hat{\zeta}^\dagger_E = \hat{\xi}^\dagger \psi_E = (\hat{\xi}^\dagger \sigma_1)(\sigma_1 \psi_E) = (\sigma_1 \hat{\xi})^\dagger (\sigma_1 \psi_E) = \hat{\xi}^T \psi^*_{-E} = \hat{\zeta}_{-E}. \tag{1.8}$$

[This again emphasises that the doubling of the number of degrees of freedom in Eq. (1.4) is only artificial.] The Hamiltonian is diagonal in these Bogoliubov fermions, which we can write purely in terms of positive-energy quasiparticles (also called canonical modes):

$$\hat{H} = \frac{1}{2}\sum_{E_\alpha} E_\alpha \hat{\zeta}^\dagger_{E_\alpha} \hat{\zeta}_{E_\alpha} = \frac{1}{2}\sum_{E_\alpha>0} E_\alpha \left(\hat{\zeta}^\dagger_{E_\alpha} \hat{\zeta}_{E_\alpha} - \hat{\zeta}^\dagger_{-E_\alpha} \hat{\zeta}_{-E_\alpha}\right) = \sum_{E_\alpha>0} E_\alpha \hat{\zeta}^\dagger_{E_\alpha} \hat{\zeta}_{E_\alpha} - \frac{1}{2}\sum_{E_\alpha>0} E_\alpha. \tag{1.9}$$

From this it is clear that the ground state $|\Omega\rangle$ should be annihilated by each $\hat{\zeta}_{E_\alpha>0}$, such that the ground state energy is $E_{\mathrm{GS}} = -\frac{1}{2}\sum_{E_\alpha>0} E_\alpha$.[9] Denote by $\hat{U}$ the unitary Bogoliubov transformation that relates positive-energy quasiparticles to the underlying fermions through $\hat{\zeta}_{E_\alpha>0} = \hat{U}\hat{c}_\alpha\hat{U}^\dagger$ for all α. The ground state is thus $|\Omega\rangle = \hat{U}|0\rangle$ relative to the fermionic vacuum $|0\rangle$ [20]. (For superconductors, therefore, the relevant gap that determines the ground state and hence the topology is that centred around $E = 0$.) The operator $\hat{U}$ can either preserve or flip the total parity $\hat{P} = (-1)^{\hat{N}}$: $[\hat{P}, \hat{U}] = 0$ or $\{\hat{P}, \hat{U}\} = 0$.[10] Hence, our statement about the ground state energy requires care when restricting ourselves to a specific parity sector, because the true ground state $|\Omega\rangle$ may not have even parity like $|0\rangle$. Ground state parity turns out to be integral to the notion of topology in zero- and one-dimensional Class D superconductors, as we see in the next section.

1.1.3 Majorana Zero Modes

For a non-interacting parity-preserving lattice Hamiltonian such as Eq. (1.4), one may always write it in a form that is bilinear in some *Majorana operators* formally defined as

$$\hat{\gamma}_{2j-1} = \hat{c}_j + \hat{c}^\dagger_j, \qquad \hat{\gamma}_{2j} = -i(\hat{c}_j - \hat{c}^\dagger_j) \tag{1.10}$$

[9] For this reason, the BdG representation of a charge-conserving free-fermion system technically requires an extra term $\hat{c}^\dagger H_0 \hat{c} \to \hat{\xi}^\dagger \mathcal{H} \hat{\xi} + \frac{1}{2}\mathrm{Tr}[H_0]$ to reproduce the same ground state energy. This offset is generally immaterial, but an important exception is when the spectrum of H_0 is not bounded from above (e.g., in a quadratically dispersing Fermi sea filled up to some chemical potential), in which case $E_{\mathrm{GS}} = -\infty$ without it. All our superconducting systems will be defined from the start by Eq. (1.4), however, so we need not worry about this energy offset.

[10] In terms of the Majorana operators below, $\hat{U}$ maps any Majorana operator to a linear combination of Majorana operators ($\hat{U}\hat{\gamma}_\alpha\hat{U}^\dagger = \sum_\beta W_{\alpha\beta}\hat{\gamma}_\beta$ where $W^T W = 1$) and hence has definite parity [20]. Its generators are rotations $e^{\frac{\theta}{2}\hat{\gamma}_\alpha\hat{\gamma}_\beta}$ and reflections $\hat{\gamma}_\alpha$. This form of the ground state agrees with the familiar coherent state of Cooper pairs $\hat{c}^\dagger_{\mathbf{k}}\hat{c}^\dagger_{-\mathbf{k}}$, provided one separately treats inversion symmetric momenta where $\mathbf{k} = -\mathbf{k}$.

which are Hermitian $(\hat{\gamma}_\alpha)^\dagger = \hat{\gamma}_\alpha$, and satisfy an anticommutation relation

$$\{\hat{\gamma}_\alpha, \hat{\gamma}_\beta\} = 2\delta_{\alpha\beta} \tag{1.11}$$

unlike ordinary fermions. The parity operator takes the form $\hat{P} = \prod_j (-i\hat{\gamma}_{2j-1}\hat{\gamma}_{2j})$. In this Majorana basis, the Hamiltonian is

$$\hat{H} = \frac{i}{4}\sum_{\alpha\beta} \hat{\gamma}_\alpha A_{\alpha\beta}\hat{\gamma}_\beta, \tag{1.12}$$

where $A = -A^T$ is a real antisymmetric matrix, which may be brought into canonical form [21] by an orthogonal transformation W such that

$$WAW^T = \begin{bmatrix} 0 & E_1 & & & \\ -E_1 & 0 & & & \\ & & \ddots & & \\ & & & 0 & E_N \\ & & & -E_N & 0 \end{bmatrix}. \tag{1.13}$$

Of course, there can be nothing profound that results from simply changing basis—rather, the interest is in Majorana operators that behave independently as excitations of a condensed matter system (or fundamental field, if they are to also excite high-energy physicists [22]). As long as a Majorana has a degenerate local partner, reversing the construction (1.10) will always yield a single conventional fermion, which is the obstacle that any physical realisation has to overcome. Consider again the superconductor in Eq. (1.7) when there is a zero mode ψ_0 with $E = 0$. If this is locally non-degenerate, then we must have $\Xi\psi_0 \propto \psi_0$ (on account of PH conjugation being local), or specifically $\Xi\psi_0 = \psi_0$ in the right gauge. By Eq. (1.8), we conclude that such a zero energy Bogoliubov quasiparticle $\hat{\zeta}_0 = \hat{\zeta}_0^\dagger$ would be its own antiparticle, and hence a Majorana zero mode (MZM). The enormous challenge of Majorana experiments is to both engineer superconductors that possess locally non-degenerate zero modes, and perform measurements on them that conclusively exclude more mundane mid-gap states [23, 24].

One Dimension

Theoretically, it is very easy to construct a model superconductor in one dimension (1D) that possesses MZMs. One ubiquitous toy model is called the Kitaev chain [25], which suffices

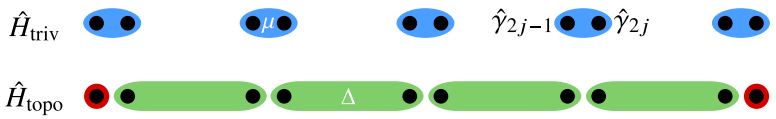

Fig. 1.1 A cartoon showing the two topologically inequivalent dimerised limits of the Kitaev chain. With open boundary conditions (OBC), the topological phase supports Majorana zero modes (MZMs) at its ends, shown in red.

to highlight the inextricable link between MZMs and the bulk topology that underlies their robustness. It will also be a building block for examples that appear in Chapters 2 and 3.

For some spinless electrons $\hat{c}_j$ on a 1D lattice, construct a Hamiltonian

$$\hat{H}_{\text{Kitaev}} = \sum_j \left[-w \left(\hat{c}_j^\dagger \hat{c}_{j+1} + \hat{c}_{j+1}^\dagger \hat{c}_j \right) - \mu \left(\hat{c}_j^\dagger \hat{c}_j - 1/2 \right) + \Delta \hat{c}_j \hat{c}_{j+1} + \Delta^* \hat{c}_{j+1}^\dagger \hat{c}_j^\dagger \right], \tag{1.14}$$

consisting of a hopping term with amplitude w, a uniform onsite chemical potential μ and p-wave pairing with superconducting gap $\Delta = |\Delta| e^{i\phi}$. Changing to a basis of Majorana operators using Eq. (1.10) [gauging away $e^{i\phi}$ through $\hat{c}_j \to e^{-i\phi/2} \hat{c}_j$ for simplicity], we arrive at

$$\hat{H}_{\text{Kitaev}} = \frac{i}{2} \sum_j \left[-\mu \hat{\gamma}_{2j-1} \hat{\gamma}_{2j} + (w + |\Delta|)\, \hat{\gamma}_{2j} \hat{\gamma}_{2j+1} + (-w + |\Delta|)\, \hat{\gamma}_{2j-1} \hat{\gamma}_{2j+2} \right]. \tag{1.15}$$

It is instructive to consider a dimerised limit of this model where $w = |\Delta|$ and $\mu = 0$, with a simple Hamiltonian

$$\hat{H}_{\text{topo}} = i\, |\Delta| \sum_j \hat{\gamma}_{2j} \hat{\gamma}_{2j+1}. \tag{1.16}$$

Now specify a chain that is finite with L sites, having open boundary conditions (OBC) as illustrated in Figure 1.1. Notice that two Majorana operators $\hat{\gamma}_1 \equiv \hat{\gamma}'$ and $\hat{\gamma}_{2L} \equiv \hat{\gamma}''$ do not appear in the Hamiltonian and hence commute with it: $[\hat{\gamma}'^{(\prime)}, \hat{H}_{\text{topo}}] = 0$, equivalent to the single-particle Hamiltonian having two locally non-degenerate zero modes. That is, this limit of the Kitaev chain with OBC supports two MZMs on its ends, separated by a gapped bulk. This can be viewed as the *fractionalisation* of a regular fermion. The opposite, trivial, limit $\hat{H}_{\text{triv}} = -i \frac{\mu}{2} \sum_j \hat{\gamma}_{2j-1} \hat{\gamma}_{2j}$ (at $w = |\Delta| = 0$ and $\mu < 0$) pairs Majorana operators on the same site and so leaves no Majoranas unpaired.

Importantly, the MZMs persist even when the parameters w, Δ and μ are perturbed away from this finely tuned point (and do not spontaneously appear near the other fine-tuned trivial point), so long as the gap does not close and $L \gg 1$. Whereas gapping out the Majoranas (i.e., moving them symmetrically away from zero energy) in $\hat{H}_{\text{topo}}$ would require

a *non-local* term $\propto i\hat{\gamma}'\hat{\gamma}''$, MZMs typically have finite spatial extent (decaying as $e^{-|x-x_0|/\xi}$ with some characteristic length ξ), meaning they are effectively coupled through local terms in the Hamiltonian if the MZM wavefunctions overlap [25]. (This is unwanted if trying to experimentally realise true MZMs.) This splitting scales as $t \propto e^{-L/\xi}$, where ξ depends on the relative strength of the energy scales in the Hamiltonian (1.14). The effective splitting term $(i/2)t\hat{\gamma}'\hat{\gamma}''$ counts the cost of occupying a non-local fermionic mode $\hat{d} = (\hat{\gamma}' + i\hat{\gamma}'')/2$. Hence, up to a correction exponentially small in the size of the system, the many-body spectrum is degenerate when in the topological phase, with degenerate states differing in their $\hat{d}^\dagger\hat{d}$ occupancy.

In more sophisticated Majorana networks the system supports many pairs of MZMs—N of them, say—leading to a 2^{N-1}-fold ground state degeneracy when conserving parity. In proposals that use MZMs as "topological qubits", this defines a computational subspace in which one can perform qubit operations. Fundamental to these operations is the fact that MZMs obey non-Abelian statistics [26, 27], on which we shall not elaborate. Indeed, it is the prospect of MZMs as ingredients for stable qubits that means that in the zoo of gapless modes classified by the tenfold way, none have received as much commercial attention as MZMs in topological superconductors [28].

Relating Majorana Zero Modes to an Invariant

Seeing that these emergent MZMs show some robustness motivates looking for nontrivial topology in the bulk Hamiltonian, which we do by following Kitaev's original paper [25]. Start with an open chain of length L hosting MZMs $\hat{\gamma}'$ and $\hat{\gamma}''$ on its ends (much like $\hat{H}_{\text{topo}}$, but not necessarily in the zero correlation length limit). Since the bulk is gapped, the parity operator may be replaced by $\hat{P} = s(L)(-i\hat{\gamma}'\hat{\gamma}'')$ where $s(L) = \pm 1$. Define the two ground states to be $|\Omega^L_\alpha\rangle$ for $\alpha = 0, 1$ with parities $s(L)(-1)^\alpha$. Now turn on a direct coupling $\hat{H}_L = iu\hat{\gamma}''\hat{\gamma}'$ between the ends that essentially closes the chain, seen in Figure 1.2, such that its (now non-degenerate) ground state $|\Omega^L\rangle$ is $|\Omega^L_1\rangle$ if $u > 0$, and $|\Omega^L_0\rangle$ if $u < 0$. The parity is hence given by $\hat{P}|\Omega^L\rangle = -s(L)\operatorname{sgn} u\,|\Omega^L\rangle$. The crucial finding will be that the presence or absence of MZMs in an open chain is encoded in the behaviour of the overall ground state parity of compositions of closed chains.

Consider two open chains A and B of lengths L_A and L_B, respectively, supporting MZMs on their ends. There are two ways to join these up, either as two disconnected loops or as one long loop (shown in Figure 1.2):

$$\hat{H}_{L_A} \oplus \hat{H}_{L_B} = iu\left[\hat{\gamma}''_A\hat{\gamma}'_A + \hat{\gamma}''_B\hat{\gamma}'_B\right], \quad \text{or} \tag{1.17}$$

$$\hat{H}_{L_A+L_B} = iu\left[\hat{\gamma}''_A\hat{\gamma}'_B + \hat{\gamma}''_B\hat{\gamma}'_A\right], \tag{1.18}$$

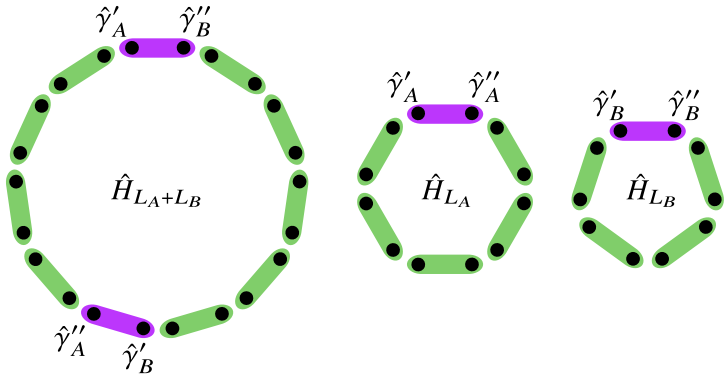

Fig. 1.2 Two topological Kitaev chains of lengths $L_A = 6$ and $L_B = 5$ closed up in two distinct ways, either as one big ring $\hat{H}_{L_A+L_B}$ or two smaller rings $\hat{H}_{L_A} \oplus \hat{H}_{L_B}$. Majoranas that are close together belong to the same site. Though common, graphically representing a hybridisation $i\hat{\gamma}''\hat{\gamma}'$ with undirected bonds is ambiguous because $i\hat{\gamma}''\hat{\gamma}' \neq i\hat{\gamma}'\hat{\gamma}''$. Here, the bonds $i\hat{\gamma}''\hat{\gamma}'$ are directed anti-clockwise when their coefficients are positive.

having ground states $|\Omega^{L_A} \otimes \Omega^{L_B}\rangle$ and $|\Omega^{L_A+L_B}\rangle$, respectively. Their parities under the total parity operator $\hat{P} = s(L_1)s(L_2)(-i\hat{\gamma}'_A\hat{\gamma}''_A)(-i\hat{\gamma}'_B\hat{\gamma}''_B)$ have *opposite* sign:[11]

$$\hat{P}|\Omega^{L_A} \otimes \Omega^{L_B}\rangle = s(L_1)s(L_2)|\Omega^{L_A} \otimes \Omega^{L_B}\rangle, \tag{1.19}$$

$$\hat{P}|\Omega^{L_A+L_B}\rangle = -s(L_1)s(L_2)|\Omega^{L_A+L_B}\rangle. \tag{1.20}$$

This is in contrast to the ground states of equivalent loops formed with trivial superconducting chains, whose parities would have the *same* sign because the chains are always gapped. We therefore have

$$\langle\Omega^{L_A+L_B}|\hat{P}|\Omega^{L_A+L_B}\rangle = \nu\,\langle\Omega^{L_A} \otimes \Omega^{L_B}|\hat{P}|\Omega^{L_A} \otimes \Omega^{L_B}\rangle, \tag{1.21}$$

where $\nu = -1, +1$ distinguishes between the presence or absence of MZMs, respectively. This distinction holds when forming closed chains of any translationally invariant 1D superconductor, which is useful because it makes no reference to a boundary.

Recalling our discussions in Sec. 1.1.2, the ground state parity is determined by whether the unitary operator $\hat{U}$ that brings the BdG Hamiltonian into its canonical form is parity preserving or not. This depends on whether the corresponding orthogonal transformation W in the Majorana basis is purely rotational, in which case $\operatorname{sgn}\det W = 1$. This quantity can be

[11] Both parities are independent of $\operatorname{sgn} u$ because there are two u links, while the sign difference follows because $(-i\hat{\gamma}'_A\hat{\gamma}''_A)(-i\hat{\gamma}'_B\hat{\gamma}''_B) = -(-i\hat{\gamma}'_A\hat{\gamma}''_B)(-i\hat{\gamma}'_B\hat{\gamma}''_A)$.

cast directly in terms of the Majorana Hamiltonian through a function called the *Pfaffian*[12], defined for antisymmetric matrices, which satisfies $\mathrm{Pf}\,(A)^2 = \det(A)$ and

$$\mathrm{Pf}\,(WAW^T) = \mathrm{Pf}\,(A)\,\det(W). \tag{1.22}$$

We can immediately apply to this to the canonical form in Eq. (1.13) to conclude[13] that

$$\langle\Omega|\hat{P}|\Omega\rangle = \mathrm{sgn}\det(W) = \mathrm{sgn}\,\mathrm{Pf}\,(A). \tag{1.23}$$

All that remains is to apply this parity formula to closed chains by switching to momentum space. For a translationally invariant superconductor with L sites and periodic boundary conditions (PBC), one finds that in terms of its Fourier-transformed Majorana Hamiltonian A_q [25],

$$\langle\Omega|\hat{P}|\Omega\rangle = \mathrm{sgn}\,\mathrm{Pf}\,(A) = \begin{cases} \mathrm{sgn}\,\mathrm{Pf}\,(A_{k=0})\,\mathrm{sgn}\,\mathrm{Pf}\,(A_{k=\pi}) & L \text{ even} \\ \mathrm{sgn}\,\mathrm{Pf}\,(A_{k=0}) & L \text{ odd.} \end{cases} \tag{1.24}$$

This features only momenta $k = -k$, where A_k is antisymmetric. Looking at the nontriviality condition (1.21), one may check that[14]

$$\nu = \mathrm{sgn}\,\mathrm{Pf}\,(A_{k=0})\,\mathrm{sgn}\,\mathrm{Pf}\,(A_{k=\pi}) \tag{1.25}$$

is the appropriate definition for the topological invariant. (The same invariant may also be written in Chern-Simons form as an integral over the BZ involving the Berry connection [29], but the above form has the advantage of being manifestly gauge invariant.) It is quite easy to argue that this is a topological property on the grounds that it cannot change unless the gap closes, but showing why $\nu = -1$ and $\nu = 1$ differ in the presence or absence of MZMs, as we have reviewed, required more finesse. This is a theme of Chapter 2, where even with knowledge of the topological invariants, more work is needed to deduce the nature of boundary states. Equation (1.24) also determines a key feature of our effective model's spectrum in Chapter 3, which is that switching from periodic to anti-periodic boundary conditions changes the ground state parity in the topological phase.

[12]The Pfaffian of a $2N \times 2N$ antisymmetric matrix A is given by

$$\mathrm{Pf}(A) = \frac{1}{2^N N!} \sum_{\sigma \in S_{2N}} \mathrm{sgn}(\sigma) \prod_{\alpha=1}^{N} A_{\sigma_{2\alpha-1},\sigma_{2\alpha}},$$

where S_{2N} is the permutation group for $2N$ elements.

[13]The canonical form has non-negative elements on the upper diagonal, so its Pfaffian is positive.

[14]An odd L is always the sum of an odd and even number, whereas an even L is composed of two even or two odd numbers.

Two Dimensions

MZMs can also appear in 2D superconductors with $p_x + ip_y$-wave pairing [30]. In 2D Class D superconductors, the topological invariant is the Chern number (1.3), where 'occupied' states are negative-energy BdG states. Like in the IQHE, a nonzero Chern number is associated with chiral edge modes. A minimal continuum model is a two-band Dirac Hamiltonian

$$\mathcal{H}(\mathbf{k}) = k_1\sigma_1 + k_2\sigma_2 + m\sigma_3 \equiv \boldsymbol{h}_\mathbf{k}\cdot\boldsymbol{\sigma}, \tag{1.26}$$

which is a good low-energy description near most gap closings. This evidently has PH symmetry $\Xi = \mathcal{K}\sigma_1$ (but not TR symmetry). Its spectrum easily follows from the anticommutation relations $\{\sigma_i, \sigma_j\} = 2\delta_{ij}$, giving $E^2(\mathbf{k}) = |\boldsymbol{h}_\mathbf{k}|^2$ which has a gap closing at $m = 0$. Provided $|m| > 0$, its wavefunctions are determined (up to a gauge choice) by the unit vector $\hat{\boldsymbol{h}}_\mathbf{k} \equiv \boldsymbol{h}_\mathbf{k}/h_\mathbf{k}$. The Berry curvature is then $\mathrm{Tr}\{\mathcal{F}\} = (-i/2)\hat{\boldsymbol{h}}_\mathbf{k}\cdot d\hat{\boldsymbol{h}}_\mathbf{k}\times d\hat{\boldsymbol{h}}_\mathbf{k}$ which we may interpret as the solid angle traced out by $\hat{\boldsymbol{h}}_\mathbf{k}$ over a small patch of momenta [10]. We cannot integrate $(i/2\pi)\int_{\mathrm{BZ}}\mathrm{Tr}\{\mathcal{F}\}$ over a compact manifold to give an integer, however, because Eq. (1.26) is a continuum model without a lattice or BZ. Instead, the closest we have is

$$\mathrm{Ch} = \frac{i}{2\pi}\int_{\mathbb{R}^2}\mathrm{Tr}\{(\mathcal{F})\} = \frac{1}{2}\,\mathrm{sgn}\,m. \tag{1.27}$$

Thus, the Dirac Hamiltonian can be used to describe only topological phase *transitions* of $\Delta\mathrm{Ch} = \pm 1$ by taking $m \to -m$. This is tied to the band structure approximation (1.26) only being valid in an isolated patch of the BZ, whose $|\mathbf{k}| \to \infty$ behaviour would be regularised by a lattice. If $\boldsymbol{h}_\mathbf{k}$ did originate from a lattice model, $\mathrm{Ch} \neq 0$ would obstruct finding a smooth gauge for wavefunctions throughout the BZ.

We can deduce the presence of chiral modes at interfaces of topologically distinct Dirac Hamiltonians through what is known as the Jackiw-Rebbi approach [31]. This finds mid-gap eigenmodes of the Schrödinger equation for Eq. (1.26) slowly undergoing a band inversion in real-space with $m = m(\mathbf{r})$. It can also deduce MZMs at interfaces in 1D, complementing the previous subsection. We use the results of such an approach extensively in Chapter 2 (and to a lesser extent in Chapter 3) when we quote the spectra of effective boundary Hamiltonians. Appendices A.2.2 and B.1 demonstrate this approach in action and are self-contained, so serve the purpose of an introduction.

The resulting edge states are called chiral Majorana modes, which we depict in Fig 1.3, but they are not inherently MZMs because that further requires zero energy. They disperse as $E(k_\parallel) \propto k_\parallel$, where $k_\parallel$ is the momentum along the boundary, but $k_\parallel$ is quantised according to the geometry of the boundary. Hence, MZMs will not occur in a simple circular sample

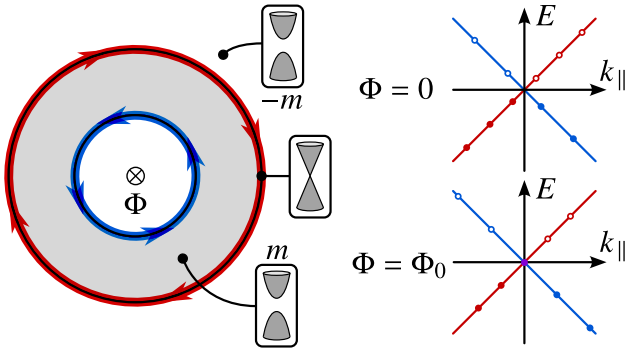

Fig. 1.3 A figure showing a 2D Dirac model shaped as an annulus with inner and outer radii R_{in} and R_{out}, respectively. The annulus and surrounding material have mass terms of opposite sign, so the bulk Hamiltonian has a gap closing at the edges, leading to chiral edge modes whose dispersions are shown on the right. The annulus may be threaded by a flux Φ which modifies the boundary conditions of fermions traversing the edges so that edge momentum is quantised as $k_{\parallel} = (2n+1+\Phi/\Phi_0)/2R_i$ with $n \in \mathbb{Z}$. When Φ is an even multiple of the flux quantum $\Phi_0 = h/2e$, there are states with $E(k_{\parallel} = 0) = 0$ localised on the inner and outer edges that are MZMs, provided that they are far enough apart not to hybridise.

of $p_x + ip_y$ superconductor because fermions on the boundary obey antiperiodic boundary conditions [30, 23]. The boundary conditions can be modified through a magnetic field, however, such as by threading an annular sample (referred to as a Corbino disc), as in Fig. 1.3 with $h/2e$ flux. Then, Majorana modes with opposite chirality form on the inner and outer edges that do intersect $E = 0$, giving two MZMs. The same argument may be used to conclude that vortices in a type-II $p_x + ip_y$ superconductor (from a penetrating flux) bind localised MZMs [30, 32].

1.1.4 Crystalline Symmetry Enriched Topological Classification

Even though it may sound from Sec. 1.1.1 as if equilibrium topological classification of every possible non-interacting fermionic Hamiltonian is complete, restricting oneself to only three symmetries often fails to capture all possible topological features of a system, however. This is because realistic systems may also possess other unitary symmetries which can lead to an even richer classification. Most notable are *crystalline symmetries*, inherited from how the ions are stably arranged in space. One expects a radical change to the map of equivalence classes because adding a symmetry requirement will forbid certain Hamiltonians entirely, and of the Hamiltonians that remain after this purge, previous symmetry- and gap-preserving interpolations between them may become disallowed, fracturing the original equivalence classes. (This is analogous to the diversification of SRE states into SPT phases that was mentioned in Sec. 1.1.) We will soon present a more grounded view of this enrichment,

where a unitary symmetry block-diagonalises the single-particle Hamiltonian so that each block (or pair of blocks) must be characterised by their own invariants.

The most obvious crystalline symmetry to include is translational symmetry, leading to what are called *weak* topological phases [9]. Whereas the surface states of *strong* topological phases (those with AZ symmetries) are robust to disorder, charge-density-wave perturbations can gap out the surfaces of weak topological phases, as we see in action in Chapter 2. The search for new types of topological phases has since expanded to all symmorphic [33, 34] and nonsymmorphic [35] space group symmetries.

As well as enriching classification, crystalline symmetries can also simplify the calculation of tenfold-way invariants, as is famously the case with the Fu-Kane parity criterion [36] in inversion-symmetric TIs. We shall rediscover another such example in Chapter 2 for the Chern number modulo a small integer. In these cases one can avoid integrating Bloch wavefunctions over the whole BZ when calculating invariants such as Eq. (1.3), which numerically would require a sufficiently dense mesh of $\mathbf{k}$ points. Modern classifications of topological crystalline systems take this idea further by defining invariants that have no tenfold-way counterparts, quantised only by virtue of the crystalline symmetries.[15]

Unfortunately, obtaining the full classification with crystalline symmetries is, understandably, much more difficult. It requires the generalisation of K-theory to so-called *equivariant* K-theory [38–40] and although this formalism has been increasingly developed, the full classification for all space groups and AZ classes is yet to be completed. Furthermore, this mathematical framework is abstracted from familiar physical concepts and does not always provide calculable invariants. In the meantime, efforts have been made to bridge between the full classification and more accessible features of the band structure [38], with great progress made by favouring ease of calculation over exhaustivity.

The current approach to classifying topological crystalline insulators is to systematically determine whether there is an obstruction to deforming the ground state into a product state of exponentially localized Wannier functions at atomic sites (filled atomic orbitals) [41]. There are often many mutually distinct arrangements of such Wannier functions at atomic sites compatible with the same crystalline symmetry that all count as trivial. Stable topology implies an obstruction of this kind, but the converse may not be true: systems with an obstructed atomic limit may possess only *fragile topology* [42]. A set of bands has fragile topology if it is strictly inequivalent to some trivial bands, but made strictly *equivalent* if we allow for adding some trivial bands below the Fermi energy.[16] Fragile topological systems

[15] In fact, even the $\mathbb{Z}_2$ Fu-Kane invariant may be promoted to a $\mathbb{Z}_4$ invariant with inversion symmetry [37].

[16] Even fragile topology has to persist upon adding trivial bands *above* the Fermi energy if it is to be a physically reasonable definition because any bounded tight binding model can never include all the high energy orbitals; moreover, such bands do not change the many-body ground state. This also distinguishes fragile

are not expected to have protected gapless boundary states because the bulk topology can be trivialised by adding atomic insulators with gapped boundaries; instead, their signatures are more subtle [44] and are still an open question. We will not encounter fragile topology later in this thesis, so it is mentioned in this section only for context. Even the bulk-boundary correspondence for stable topological crystalline systems is less robust than in the tenfold way because the boundary itself must also respect the crystalline symmetries, and nonsymmetric boundaries are generically gapped [45, 46].

Two methods have emerged as ways to efficiently determine whether a band structure is topological, but (as well as in how they are calculated) they differ in whether the topology they diagnose is stable or not. The workhorses in both methods are the crystalline symmetry representations at high-symmetry points (HSPs) in the BZ. One method uses 'split elementary band representations' [47] to diagnose (possibly fragile) topology, where determining the connectivity of the band structure from the irreducible representations at HSPs can be efficiently mapped to a graph-theoretic problem [47].[17] The other method using *symmetry indicators* [48] diagnoses stable topology by construction, but misses out on certain topological phases by putting them in the same category as trivial atomic insulators. It is the symmetry indicator approach (generalised to superconductors) that we utilise in Chapter 2, so warrants more discussion.

Symmetry Indicators for Band Topology

Symmetry representations have always played a large role in band theory, and we now outline a way that they relate to topology [41]. The information fed into this classification scheme, once the crystalline and fundamental symmetries are specified, will be the symmetry representations at HSPs in the BZ. Clearly this is much less information than the full bundle of Bloch wavefunctions throughout the BZ, so the classification will be only a 'snapshot' of the full one, but a useful one nonetheless. The starting point will be a set of band labels at the HSPs, which will later define a (quasi-)vector space of crystalline topological phases.

Start with a Bloch Hamiltonian $\mathcal{H}(\mathbf{k})$ which has symmetry group G. We generally care about only the point group elements of G because translations just give phases for the Bloch states. There is a projective representation $U_g(\mathbf{k})$ for $g \in G$ such that

$$\mathcal{H}(\mathbf{k}) = U_g(\mathbf{k})\mathcal{H}(g\mathbf{k})U_g^\dagger(\mathbf{k}), \tag{1.28}$$

topology from *Hopf insulators*, which rely on nontrivial mappings between certain spaces, e.g. two-band insulators in 3D without symmetries that should be trivial according to the tenfold way [43].

[17] That this method cannot guarantee stable topology was noticed later as the concept of fragility was introduced [42].

where $U_g(\mathbf{k})$ is a unitary matrix.[18] This representation is 'projective' because the transformation rule (1.28) determines $U_g(\mathbf{k})$ only up to a phase factor. These phases can be made consistent only up to a sign [49] which defines the factor system

$$U_g(\mathbf{k})U_{g'}(\mathbf{k}) = z_{gg'}U_{gg'}(\mathbf{k}), \qquad z_{gg'} = \pm 1. \tag{1.29}$$

The factor system $z_{gg'} = 1$ occurs when there is spin rotation symmetry, and is labelled the 'spinless' case because spatial rotation (which also acts on spin) could be combined with a pure spin rotation in the other direction to render it effectively spinless [50]. The other case is relevant for 'spinful' systems, such as those with spin-orbit coupling. One way around needing a factor system is to not start with projective representations of the space group in the first place, and instead non-projectively represent a double-covered space group $\tilde{G}$ which also features total fermion parity $\hat{P}$ as a group element. This is because, fundamentally, every electron acquires a Berry phase of $e^{i\pi}$ under 2π rotation. This is the approach that we take in Chapter 2 where, because we are dealing with a spinful system, a 2π rotation has representation $-\mathbb{1}$, which influences the rest of the analysis.

The symmetry relation at certain points in the BZ is special. HSPs, $\mathbf{k}_s$, are momenta that are mapped to themselves under some (non-translational) elements of G *modulo* a reciprocal lattice vector $\mathbf{G}$, i.e., $g\mathbf{k}_s = \mathbf{k}_s + \mathbf{G}$, shown for an example space group in Fig. 1.4 (γ). Thus, at HSPs we have

$$\mathcal{H}(\mathbf{k}_s) = U_g(\mathbf{k}_s)\mathcal{H}(\mathbf{k}_s)U_g^\dagger(\mathbf{k}_s) \tag{1.30}$$

for some point group elements g belonging to the nontrivial *little group* $G_{\mathbf{k}_s} \subset G$ of $\mathbf{k}_s$ (also called the *stabiliser subgroup*). Suppose that $|\psi^\alpha(\mathbf{k}_s)\rangle$ is an energy eigenstate of $\mathcal{H}(\mathbf{k}_s)$ with energy $E_{\mathbf{k}_s}$, degenerate with $(d-1)$ other states so that $\alpha = 1, \ldots, d$ labels the degenerate subspace. Since $U_g(\mathbf{k}_s)$ commutes with $\mathcal{H}(\mathbf{k}_s)$ for $g \in G_{\mathbf{k}_s}$, it must map degenerate eigenstates to each other as

$$\hat{U}_g(\mathbf{k}_s)|\psi^\beta(\mathbf{k}_s)\rangle = \sum_\alpha [u_g(\mathbf{k}_s)]_{\alpha\beta}|\psi^\alpha(\mathbf{k}_s)\rangle. \tag{1.31}$$

The unitary matrices $u_g(\mathbf{k}_s)$ satisfy the same relations as Eq. (1.29), so furnish a d-dimensional representation of $G_{\mathbf{k}_s}$. Unless the degeneracy is accidental, $u_g(\mathbf{k}_s)$ is an *irreducible* representation (irrep). There can be n distinct irreps $u_g^i(\mathbf{k}_s)$ of the same little group, each being $d_i(\mathbf{k}_s)$-dimensional. Any representation of $G_{\mathbf{k}_s}$ can be decomposed as the direct sum of irreps

[18] Promoting this representation for normal Hamiltonians to one for BdG Hamiltonians further requires knowing how the superconducting pairing term $\Delta(\mathbf{k})$ behaves under symmetry, but we save this discussion for when we encounter it in Chapter 2. Similarly, the origin of the momentum dependence of $U_g(\mathbf{k})$, namely the translational component of g, is saved until then because it is most easily seen through example.

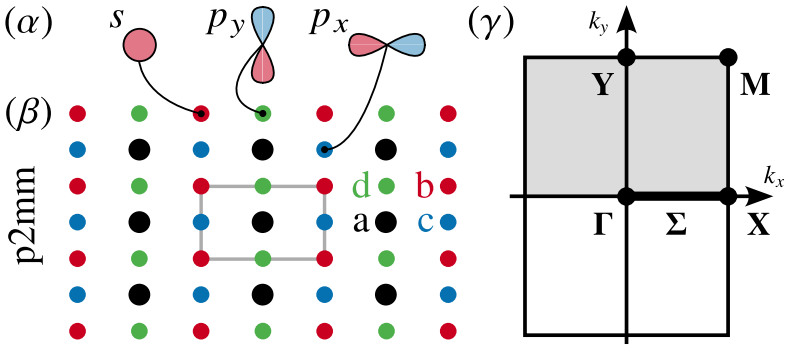

Fig. 1.4 Real- and momentum-space representations of the wallpaper group p2mm. This space group features two perpendicular mirror planes and C_2 rotation symmetry about the out-of-plane axis. Its maximal Wyckoff positions (i.e., HSPs in real space) {a, b, c, d} are shown in (β). Atomic limits are constructed by placing filled orbitals [such as those shown in (α)] at the these positions in various symmetric combinations. These orbitals furnish representations of the dihedral point group D_2 which get transformed into momentum-space representations. (γ) shows the BZ for the lattice, along with its HSPs and a mirror symmetric line $\mathbf{\Sigma}$ referenced later.

$\{u_g^i(\mathbf{k}_s)\}$ with multiplicities $\{N_i(\mathbf{k}_s)\}$, so the most general symmetry representation is

$$U_g(\mathbf{k}_s) \simeq \mathrm{diag}\,[u_g^1(\mathbf{k}_s) \otimes \mathbb{1}_{N_1(\mathbf{k}_s)}, \ldots, u_g^n(\mathbf{k}_s) \otimes \mathbb{1}_{N_n(\mathbf{k}_s)}], \tag{1.32}$$

with "$\simeq$" allowing for a similarity transformation. The total dimension $\sum_{i=1}^n d_i(\mathbf{k}_s)N_i(\mathbf{k}_s)$ is constant throughout the BZ because it counts the number of orbitals in the unit cell. Antiunitary symmetries such as TR also interact with the unitary space group representations (e.g., by mapping one irrep to another because they involve complex conjugation), but we encounter only PH symmetry in Chapter 2. For superconductors, one combines separate irreps for the particle and hole sectors to form a larger representation for the BdG Hamiltonian, but we stick to normal Bloch Hamiltonians for now.

The foundation of symmetry indicators is the classification of every $\mathcal{H}(\mathbf{k}_s)$, which are zero-dimensional Hamiltonians possessing unitary symmetries specified by $G_{\mathbf{k}_s}$ on top of fundamental (TR, PH or chiral) symmetries. The multiplicity of the irreps immediately present themselves as candidates for being topological invariants, which we illustrate by example in Figure 1.5. Here we consider two HSP Hamiltonians $\mathcal{H}_0(\mathbf{\Pi})$, $\mathcal{H}_1(\mathbf{\Pi})$ and a symmetric adiabatic interpolation between them $\mathcal{H}_t(\mathbf{\Pi})$. We count the multiplicities of the irreps of *occupied* states (those below the Fermi energy), labelled by $\#\Pi_i \leq N_i(\mathbf{\Pi})$, to form a "vector"[19] $\mathbf{n}_t = [\#\Pi_1, \ldots, \#\Pi_n]^T$. Crucially, if the vectors $\mathbf{n}_0$ and $\mathbf{n}_1$ are different, then there

[19]Being integer-valued, $\mathbf{n}$ isn't technically a vector, but our intuition for vector spaces will still hold up well.

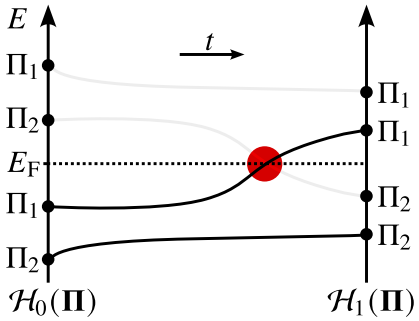

Fig. 1.5 A diagram showing the symmetric deformation $\mathcal{H}_t(\mathbf{\Pi})$ between two HSP Hamiltonians with different irreps. Because the multiplicities of the occupied irreps $\#\Pi_1$, $\#\Pi_2$ do not match on either side, energies must cross the Fermi energy E_F at some point and the underlying band structures for $t = 0$ and $t = 1$ cannot be in the same topological phase.

must be no way to adiabatically connect $\mathcal{H}_0(\mathbf{\Pi})$ and $\mathcal{H}_1(\mathbf{\Pi})$ without closing the gap. This follows because $G_{\mathbf{\Pi}}$ is preserved throughout and $U_{g,t}(\mathbf{\Pi})$ must change adiabatically. The first step for classification through symmetry indicators, therefore, is to construct a large vector of band labels for multiplicities of occupied irreps at all representative[20] HSPs in the BZ. One may add and subtract whole multiples of these vectors to move around in a $\mathbb{Z}^{d_\mathrm{BL}}$ "vector space" corresponding to a group of band labels {BL}. In superconductors, there may also be Pfaffian invariants definable at PH-invariant momenta, but in Chapter 2 these are expressible in terms of the irrep band labels.

As it stands, the dimension d_BL of this space of band labels is much too large because HSPs do not exist in isolation, and the symmetry representations at different points have to satisfy certain *compatibility relations* depending on the symmetry group. As one moves infinitesimally away from a HSP $\mathbf{k}_\mathrm{s}$ in a certain direction to $\mathbf{k}_\mathrm{s} + \delta\mathbf{k}$, some symmetries may be broken $G_{\mathbf{k}_\mathrm{s}} \to G_{\mathbf{k}_\mathrm{s}+\delta\mathbf{k}} \subseteq G_{\mathbf{k}_\mathrm{s}}$, which lifts degeneracies. For the symmetries $\tilde{g} \in G_{\mathbf{k}_\mathrm{s}+\delta\mathbf{k}}$ that remain, however, the representations $U_{\tilde{g}}(\mathbf{k}_\mathrm{s} + \delta\mathbf{k})$ must be compatible with the irreps $u_{\tilde{g}}(\mathbf{k}_\mathrm{s})$. We say that $U_{\tilde{g}}(\mathbf{k}_\mathrm{s} + \delta\mathbf{k})$ is 'subduced' from $u_{\tilde{g}}(\mathbf{k}_\mathrm{s})$, written $u_{\tilde{g}}(\mathbf{k}_\mathrm{s}) \mapsto U_{\tilde{g}}(\mathbf{k}_\mathrm{s} + \delta\mathbf{k})$. Consequently, for the Hamiltonian to remain gapped along a line Σ from one HSP $\mathbf{k}_1$ to another inequivalent HSP $\mathbf{k}_2$, any band labels definable on Σ (due to a nontrivial little-group G_Σ) have to remain continuous as one approaches both $\mathbf{k}_1$ and $\mathbf{k}_2$. This defines a compatibility relation between the band labels at HSPs $\mathbf{k}_1$ and $\mathbf{k}_2$. We show this in action for an example wallpaper group (i.e., two-dimensional space group) in Fig. 1.6. Hence, not all elements of {BL} are self-consistent, and we must reduce the space to valid gapped band structures, denoted by $\{\mathrm{BS}\} \simeq \mathbb{Z}^{d_\mathrm{BS}}$. In practice this is done by expressing compatibility relations as a

[20] We say 'representative' because if there exists an element $g \in G$ for which $\mathbf{k}_1 = g\mathbf{k}_2$, then $\mathbf{k}_1$ and $\mathbf{k}_2$ have conjugate little groups, and any information at $\mathbf{k}_2$ is already contained in the irrep content of $\mathbf{k}_1$. Some schemes also lump this restriction in with the 'compatibility relations' (defined below), but we consider them separately.

Π_i	I	M_x	M_y	R_π
Γ_1, X_1	1	1	1	1
Γ_2, X_2	1	−1	−1	1
Γ_3, X_3	1	1	−1	−1
Γ_4, X_4	1	−1	1	−1

(a)

Σ_i	I	M_y
Σ_1	1	1
Σ_2	1	-1

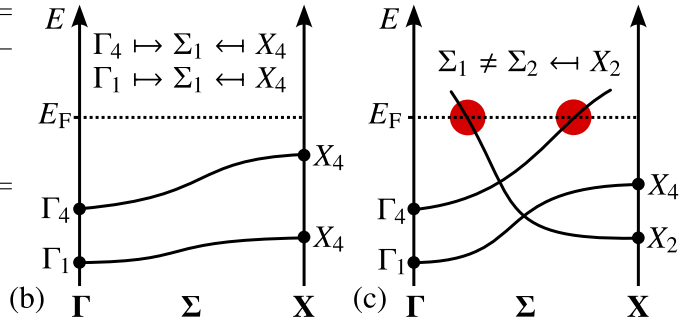

Fig. 1.6 An example of how compatibility relations dictate which band labels are valid gapped band structures for the wallpaper group p2mm. (a) The spinless one-dimensional irreps for the dihedral group D_2 and the cyclic group C_2. In moving from $\mathbf{\Gamma}$ or $\mathbf{X}$ along the mirror-symmetric line $\mathbf{\Sigma}$ (see Fig. 1.4), the little group D_2 is reduced to a subgroup C_2. The representations must agree for the symmetry element M_y left unbroken. In (b) and (c) we test whether the band labels at $\mathbf{\Gamma}$ and $\mathbf{X}$ are consistent with two isolated bands below the Fermi level. The band labels in (b) pass this test, but in (c) the irreps X_2 and Γ_4 subduce to different representations along $\mathbf{\Sigma}$ so they cannot belong to the same band.

linear constraint $C\mathbf{n} = \mathbf{0}$ for some matrix C, and considering only the null space of C. (Here is where 'topological quantum chemistry' [47] departs from the symmetry indicator approach by using a graph-theoretic approach to solve the compatibility relations instead.) Despite their general importance, we won't have any high-symmetry lines or compatibility relations in Chapter 2 because we deal only with rotation symmetry in 2D, and hence {BS} = {BL} there.

Naturally, the symmetry representations $U_g(\mathbf{k})$ above arise from Fourier-transforming real space symmetry operations of G, which we show in detail in Sec. 2.2.1. Since one seeks a stable classification, a special role is played by the band label vectors $\mathbf{a}$ of atomic insulators, which follow from placing filled orbitals at symmetry-allowed Wyckoff positions [51] as shown in Fig. 1.4 (β).[21] This role is to define a subspace spanned by the vectors $\{\mathbf{a}_j\}$ (which may not be linearly independent) corresponding to a subgroup $\{\text{AI}\} \simeq \mathbb{Z}^{d_{\text{AI}}}$ of {BS} that we consider topologically trivial. Note that because {AI} allows for the addition or subtraction of vectors $\mathbf{a}_j$, an element $\mathbf{a} \in \{\text{AI}\}$ may have negative band label integers $\#\Pi_i$ which would immediately prevent us from interpreting its components as occupied irrep multiplicities of a physical atomic insulator. This arises because adding vectors is implemented through stacking, but subtraction has no such direct physical procedure. In fact, even all the components being

[21] Like we saw in momentum space, some positions $\mathbf{x}$ in the real space unit cell are invariant under the action of a non-trivial group $G_\mathbf{x} \subset G$ called its *site-symmetry group* (or *stabiliser group*). Such a point $\mathbf{x}$ is in the *orbit* of another, $\mathbf{x}'$, if they are related by $g\mathbf{x} = \mathbf{x}'$ for some $g \in G$, from which it follows that their site-symmetry groups $G_\mathbf{x}$ and $G_{\mathbf{x}'}$ are conjugate. Points with conjugate site-symmetry groups are said to be in the same *Wyckoff position*.

positive is not enough to guarantee that **a** can be realised by stacking atomic insulators, because it may be the 'difference' of two atomic insulators, as in a fragile topological phase. Nevertheless, we get the stable 'symmetry indicator' classification group by constructing the quotient

$$\{\mathrm{SI}\} = \frac{\{\mathrm{BS}\}}{\{\mathrm{AI}\}}, \tag{1.33}$$

which guarantees that systems mapping to distinct elements of {SI} are not deformable into each other even when allowing stacking with atomic insulators. It can be shown [48] that the resulting group structure is always finite (even for superconductors [49, 52]):

$$\{\mathrm{SI}\} \simeq \mathbb{Z}_{s_1} \times \mathbb{Z}_{s_2} \times \ldots \times \mathbb{Z}_{s_{d_{\mathrm{BS}}}} \tag{1.34}$$

with positive integers s_i and $d_{\mathrm{BS}} = d_{\mathrm{AI}}$. The group is nontrivial if any $s_i > 1$. Assigning a vector **n** to an element in {SI} can be done very efficiently as a linear algebra problem once the basis vectors $\{\mathbf{a}_j\}$ for atomic insulators in the appropriate symmetry class are known.

Evidently the finite group {SI} cannot always coincide with the true stable topological classification group because we have already encountered phases labelled by an unbounded $\mathbb{Z}$-valued Chern invariant. What symmetry indicators can do, therefore, is quickly diagnose if a system is gapped at HSPs and incompatible with an atomic description, which is valuable to high-throughput searches for topological materials [53–55]. This requires further validation to rule out accidental crossings at nonsymmetric points in the BZ. For this reason, in Chapter 2 we do not take the final step of constructing the quotient group as in Eq. (1.33) because a provably complete set of stable invariants are available for our particular symmetry class. This combines a set of linear combinations of band labels $\{\#\Pi_i\}$ with the Chern number (1.3), which were shown to classify the band structure over the whole BZ for Class D superconductors with rotational symmetry [56]. We then use these invariants to derive a bulk-boundary correspondence.

Above, we alluded to differences when extending symmetry indicators to superconductors, which was achieved iteratively over many studies owing to its increased difficulty [57, 58, 52, 59, 49]. The biggest conceptual difficulty is properly defining an 'atomic limit' superconductor, which is necessary for a classification that works beyond the weak-pairing limit. (In the weak-pairing limit the insulator invariants work just as well for a superconductor because the eigenstates of the BdG Hamiltonian are directly related to the eigenstates of the normal diagonal part.) The proper 'atomic limit superconductor' is one whose pairing can be switched off $\hat{\Delta} \to 0$ without closing a gap such that the resulting insulator is in its

atomic limit [59].[22] Trivial superconductors are adiabatically connected to the 'atomic limit' superconductor as usual. The trivial group may be equally viewed as being generated by arrays of 0D BdG Hamiltonian symmetrically placed at Wyckoff positions [49]. Deriving the symmetry-indicated classification group then follows the principles above, with additional enrichment due to the nontrivial symmetry representations possible for the pairing term $\hat{\Delta}$.

1.1.5 Higher-Order Topology

Topological crystalline insulators and superconductors are particularly interesting because they can display an entirely new kind of bulk-boundary correspondence due to *higher-order topology*. The gapless states we have introduced thus far have been on codimension-one submanifolds of conventional topological systems. Systems with n-th order topology, on the other hand, have gapless states on manifolds of codimension n allowed to be greater than one, as shown in Figure 1.7. These may be thought of as globally irremovable surface topological defects of dimension $d-n$ [61]. Typically, the stability of a $d-n$ dimensional defect is given by its tenfold way classification [62], depending only on $\delta = d-n+1$ and its AZ symmetry class. However, a nontrivial defect classification on its own is not enough to generically protect anomalous gapless surface states because, on a sphere, topological defects can always be removed. For example, on the surface of a (smoothed out) 3D slab, like in Figure 1.7, a line defect can be shrunk down to a point, while point defects—which always come in pairs—can be brought together and annihilated [61]. Such processes could be obstructed by the right spatial symmetry (e.g. inversion symmetry forcing point defects to be antipodal), hinting that crystalline symmetries are crucial for the protection of higher-order topology.

This raises an important point: the presence of gapless states with codimension $n > 1$ is insufficient to conclude that the bulk has higher-order topology. Indeed, there are systems without crystalline symmetries that ostensibly fit the definition for higher-order topology, such as 3D TIs penetrated by an arbitrarily orientated magnetic field [63, 64], which have hinge modes like those in Figure 1.7. Although stable up to continuous deformations preserving the bulk and surface gaps, their gapless hinges disappear upon being exchange coupled to a ferromagnetic insulating film. In such examples, the system has "extrinsic" higher-order topology attributed to the boundary being nontrivial, whereas the bulk is trivial [46]. By contrast, the "intrinsic" classification puts crystals that differ only by their lattice termination in the same topological class. A nontrivial intrinsic classification requires spatial (or spatiotemporal [65]) symmetries, and it is this termination-independent classification we

[22] The link to a physical state is inevitably less direct for superconductors, but topology is encoded in the long-distance behaviour of the Cooper pair wavefunction [30, 60]: decay is exponential if trivial and algebraic if topological.

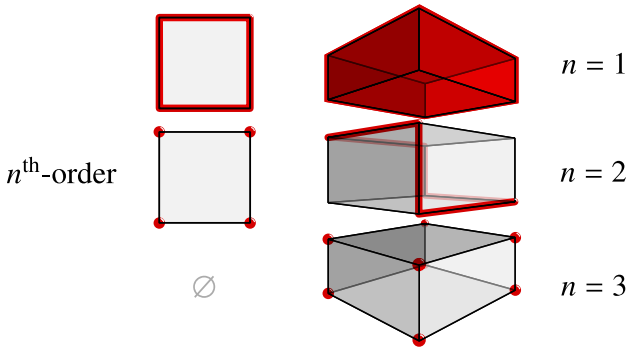

Fig. 1.7 A cartoon showing the codimensionality of gapless surface states. In 2D there can be gapless edges ($n = 1$) or corner modes protected by rotational symmetry ($n = 2$). In the 3D example there can be gapless surfaces ($n = 1$), hinges protected by inversion symmetry ($n = 2$) or corners protected by mirror symmetries ($n = 3$).

are interested in. Even for intrinsic higher-order topological phases, the precise form of the anomalous boundary states may depend on how the lattice is terminated (such as in Chapter 2, where "corner modes" can be moved away from corners), but their existence is ensured by the bulk topology so long as the boundary respects the appropriate point group symmetry.

Since its initial discovery [65–69], higher-order topology has been found in many different settings, sometimes manifesting in other ways beyond mid-gap states. In each setting, establishing the higher-order bulk-boundary correspondence requires invariants beyond the tenfold way that are yet to be unified. For example, topological insulators with non-commuting mirror symmetries can have quantised multipole moments due to fractional $\pm\frac{e}{2}$ corner charges [67, 68]. Here, just as the dipole can be formulated in terms of the Berry phase [70], the quadrupole and octupole moments are calculated through so-called 'nested' Wilson loops [67] over subspaces in the BZ, which become quantised bulk invariants in the presence of spatial symmetries. One may also find fractional $\frac{e}{n}$ corner charges in 2D C_n-symmetric insulators without multipole moments or in-gap states [71], again linked to a topological index (that is 'secondary' because it requires the primary index—the polarisation—to vanish).[23] This index is expressed in terms of symmetry indicators, which find wider use in diagnosing higher-order gapless states [37] and are used for our second-order bulk boundary correspondence for 2D superconductors in Chapter 2. In our setting the second-order gapless states will be 0D MZMs.

[23]The fractional charge here is the result of a *filling anomaly*, a mismatch between the number of ionic sites and the number of electrons needed to maintain rotational symmetry. For Wannier-representable phases this happens when Wannier orbitals lie on the corner of a unit cell [71]. This is a scenario we exclude in Chapter 2 because the classification scheme we use does not apply, as outlined in Appendix A.1.

1.2 Practical Aspects of Topological Superconductors

Realising MZMs is especially difficult because no superconducting materials have been found to be innately topological. The vast majority of superconductors pair electrons with opposite spin through s-wave pairing, leading to quasiparticles of the form $\hat{\alpha} \approx u\hat{c}_{\downarrow}^{\dagger} + v\hat{c}_{\uparrow}$ that are hopelessly distinct from $\hat{\alpha}^{\dagger}$. (Even strontium ruthenate Sr_2RuO_4, once the leading candidate for p-wave superconductivity [23], now seems to host a different type of unconventional superconductivity [72–74].) Experiments therefore turn to more artificial routes of inducing topological superconductivity using conventional superconductors. One promising experimental avenue for MZMs in 1D systems was the nanowire construction [75, 76] that was the subject of hundreds of subsequent papers. Despite some experimental groups implementing this construction and claiming observations consistent with MZMs [77, 78], the landmark result [79] was later spectacularly retracted [80], and concerns about related experiments persist. The approach is to induce p-wave superconductivity in a semiconducting nanowire through the proximity effect of an adjacent s-wave superconductor, which also requires strong spin-orbit coupling and a modest magnetic field. The motivation for these ingredients remains the same for other experimental proposals, which is to break all the symmetries (i.e. spin-rotation and time-reversal) that otherwise lead to MZMs having local degenerate partners.

Even after creating a topological superconductor, experimentally demonstrating its nontriviality is another challenge. Some difficulties are due to unwanted physical processes; for example, we saw in Sec. 1.1.3 that parity conservation is key to the phenomenology of topological superconductors, so it is crucial to mitigate 'quasiparticle poisoning', whereby fermions tunnel into or out of the system and cause transitions between (degenerate) states with different parity [81, 24].[24] The small proximity-induced topological gap also makes the system generally susceptible to stray terms in the Hamiltonian. The other difficulty is passing the most stringent tests for 'smoking gun' signatures of topological superconductivity. In early MZM experiments, the aim was to a find quantised zero-bias conductance peak in the tunnelling spectroscopy [83, 84], which is a local probe for MZMs that is easier than demonstrating non-Abelian exchange statistics through braiding. It has since been shown that these local probes can be mimicked [85] by topologically trivial 'quasi-Majorana' states that are instead pairs of near-zero energy Andreev bound states [86].[25] Modern focus

[24] Some hence prefer to prefix "topological phase" with "fermion-parity-protected" in these systems [82].

[25] These states occur when the confining potential is sufficiently smooth (similar to the nontopological boundary states that motivate our sharp mass inversion limit in a different setting in Sec. 3.4.1). The tunnelling amplitudes for the two quasi-Majoranas differ drastically because the effective tunneling barriers they experience are different (either from being oppositely spin-polarised [85] or partially separated [87]), which mimics the signal that would result from probing one side of a topological wire hosting two spatially separated MZMs.

has therefore shifted to more robust probes of topological superconductivity going beyond measuring individual MZMs. One strategy is to look for signs of a *bulk* topological phase transition [88–90] (rather than boundary states), while another is having the non-locality and statistics of multiple MZMs manifest in a way that does not require physical braiding. Some approaches adopting the latter strategy include the topological Kondo effect [91], where MZMs play the role of a spin impurity that couples to conduction electrons in the leads, and a recent weak measurement protocol [92] that encodes topological nontriviality in the shot noise of current cross-correlations. The cornerstone of both approaches is the exploitation of charging energy in mesoscopic superconductors, which forms a "Majorana-Cooper box" that is finding increasing utility in the field [93]. We next outline the basic physics of charging energy in superconductors since it forms the basis of our investigations in Chapter 3.

1.2.1 Charging Energy in Mesoscopic Superconductors

Utilising charging energy in platforms for topological superconductivity is proving fruitful for both theory and experiment [93]. The relevance of this term stems from the small dimensions of constituent superconductors, which leads to small capacitances and hence a large energy associated with adding or subtracting electrons. Consequently, it can lift the degeneracy of the even and odd parity ground states that we encountered in Sec. 1.1.3 in potentially advantageous ways. For example, Coulomb effects can be baked in to topological quantum computation schemes to guard against quasiparticle poisoning [94], or directly braid MZMs [95, 96]. By adding onsite charging energy to higher-order topological superconductors, one may even generate topologically ordered stabiliser codes [97]. The tools for treating charging energy are borrowed from circuit quantum electrodynamics (QED), which is the study of quantised electrical circuits that incorporate phenomenology associated only with superconductors, namely the Josephson effect [98].[26] In Chapter 3, we consider how charging energy affects a system where the superconducting phase controls the topology. This ingredient is present in modern planar Josephson junction platforms for MZMs [100, 101] which have been constructed experimentally and reported to pass local tunnelling probe tests for topological superconductivity [102, 103]. When adding charging energy to such systems, the low-energy spectrum shares common features with the simpler system of a Josephson junction sitting in parallel with a capacitor, known as the *Cooper pair box* (CPB).

[26] Circuit QED is itself of immense current interest because it is the basis of superconducting qubits famously used by *Google* [99] and *IBM*. The term was chosen for its similarity to 'cavity QED', since one may engineer discrete energy levels to form an artificial atom—as we soon see—which may be strongly coupled to the electromagnetic field through a microwave resonator [98].

The Cooper Pair Box

The features of the CPB are best contrasted with the quantum version of the familiar LC oscillator [104]. Consider an inductor in parallel with a capacitor, and recall that (linear) inductance and capacitance are defined through $L = \Phi/I$ and $C = Q/V$, respectively. The energy stored in a given component is given by $E(t) = \int_{-\infty}^{t} dt' V(t') I(t')$, where the branch current I and voltage V are assumed to be zero in the distant past [105]. It is convenient to rephrase these in terms the flux Φ threading the inductor and the capacitor's charge Q through Faraday's law $\Phi(t) = \int_{-\infty}^{t} dt' V(t')$ and charge conservation $Q(t) = \int_{-\infty}^{t} dt' I(t')$. Performing the energy integral for both components then neatly gives the total system energy

$$\mathcal{H}_{LC} = \frac{Q^2}{2C} + \frac{\Phi^2}{2L}. \tag{1.35}$$

Combining the above relations shows that Φ and Q are canonically conjugate variables. Following Dirac's principle, we quantise these by associating the Poisson bracket with a commutation relation between operators:

$$\{\Phi, Q\} = 1 \quad \rightarrow \quad [\hat{\Phi}, \hat{Q}] = i\hbar. \tag{1.36}$$

The Hamiltonian (1.35) is then of course the quantum Harmonic oscillator with equally spaced eigenvalues $\epsilon_n = \hbar\omega(n + \frac{1}{2})$ and $\omega = 1/\sqrt{LC}$.

In a CPB, the inductor is replaced by a Josephson junction which acts as a *nonlinear* inductor. The major difference comes from the Josephson relations [106] which govern the dissipationless current flowing between two superconducting electrodes separated by a thin insulating barrier. Firstly, the supercurrent is given by

$$I = I_c \sin\phi, \tag{1.37}$$

where ϕ is the difference between superconducting phases $\Delta e^{\pm i\phi/2}$ on both sides of the junction, and I_c—a property of the junction—is the critical current. (In the regime beyond I_c, which we do not enter, Cooper pairs break down and the current becomes resistive [107].) Secondly, a voltage V across the junction gives time dependence to the phase difference: $\dot{\phi} = \frac{2\pi}{\Phi_0} V$, where $\Phi_0 = h/2e$ is the flux quantum, or equivalently

$$\phi = \frac{2\pi}{\Phi_0}\Phi \tag{1.38}$$

in terms of the flux. [By combining Eqs. (1.37) and (1.38), one can define a nonlinear inductance as $L_J(\Phi) = (\partial I/\partial\Phi)^{-1}$ when below the critical current.] The energy stored in the Josephson junction due to coherent tunnelling of Cooper pairs is hence

$$E(t) = \int_{-\infty}^{t} dt' V(t')I(t') = I_c \int_{-\infty}^{t} dt' \left(\frac{d\Phi}{dt'}\right) \sin\left(\frac{2\pi}{\Phi_0}\Phi\right) = -E_J \cos\left(\frac{2\pi}{\Phi_0}\Phi\right), \tag{1.39}$$

defining $E_J \equiv \Phi_0 I_c/2\pi$ to be the *Josephson energy*. Again, charge Q is conjugate[27] to the flux Φ, which provides a route to quantisation, but we instead express it in terms of the phase difference ϕ and the number of paired electrons on the island $N = Q/e$.[28] We therefore arrive at the fundamental charge-phase uncertainty relation

$$[\hat{\phi}, \hat{N}] = 2i. \tag{1.40}$$

The operator $e^{i\hat{\phi}}$ hence adds a Cooper pair to the island. We also attach a voltage source and capacitance as shown in Figure 1.8 (a) to act as a non-integer offset charge for the superconducting island; in real systems this may be due to a deliberate voltage bias or spurious "charge noise". After accounting for this offset, the quantised CPB Hamiltonian is

$$\hat{H} = E_C(\hat{N} - N_g)^2 - E_J \cos\hat{\phi}, \tag{1.41}$$

where $N_g = C_g V_g/e \in \mathbb{R}$ and $E_C = e^2/2(C_\Sigma + C_g)$ is the *charging energy* [104]. We intuitively view this as the combination of a potential term $-E_J\cos(\hat{\phi})$ at odds with a kinetic energy term $(\hat{N} - N_g)^2$, which endows a particle's periodic "position" $\phi \in (-\pi, \pi]$ with dynamics. In this analogy E_C is an "inverse mass" for the particle. The Hamiltonian is anharmonic, with decreasing energy gaps between higher levels [108] visible in Fig. 1.8 (b).

With this anharmonicity comes the hope of individually addressing the two lowest states of the CPB—an impracticable task for an LC oscillator—which has been developed further into the successful *transmon qubit* [108]. The transmon takes the $E_J/E_C \gg 1$ limit of the CPB, which is motivated by the typical lack of control over N_g. As seen in Figure 1.9, for modest E_J/E_C the low energy spectrum is strongly influenced by N_g, whereas the influence weakens for larger E_J/E_C. Fluctuations in N_g therefore lead to fluctuations in the qubit transition frequency and dephasing. This decoherence mechanism is exponentially suppressed in E_J/E_C, which overcomes the algebraic suppression of the anharmonicity, as is desirable for quantum information. It is the precise dependence of the low-energy spectrum on N_g (rather than its qubit potential) in the transmon regime that is relevant to our later problem

[27] The Lagrangian (kinetic energy minus potential energy) is $\mathcal{L} = C\dot{\Phi}^2/2 + E_J\cos(\frac{2\pi}{\Phi_0}\Phi)$ so $\partial\mathcal{L}/\partial\dot{\Phi} = C\dot{\Phi} = Q$.

[28] Our convention differs from most circuit QED literature which counts the number of Cooper *pairs*.

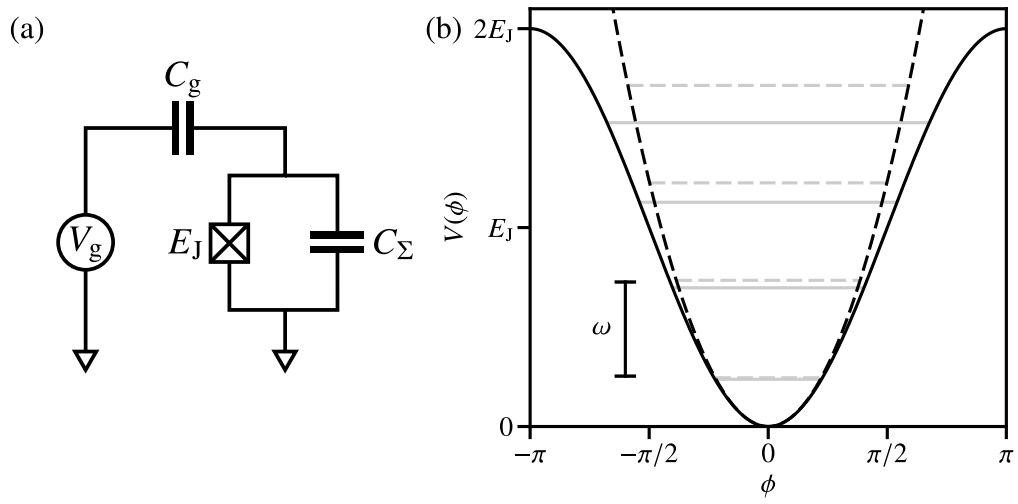

Fig. 1.8 (a) Lumped circuit diagram for a voltage-biased transmon qubit. The transmon qubit is a Josephson junction (denoted by a cross) with Josephson energy E_J and intrinsic capacitance C_J shunted by a capacitor C_S so that $C_\Sigma = C_J + C_S$, grounded on one side. The C_g and V_g elements provide voltage-biasing. (b) The effective potential ϕ for a Cooper pair box (CPB) compared to an LC oscillator (dotted), along with the lowest energy levels. Anharmonicity makes the CPB energy gaps progressively smaller than the evenly spaced $\omega = 1/\sqrt{LC}$ oscillator energies.

in Chapter 3, however. There, we couple the Josephson phase to topological fermions and explore probability of ϕ phase slips encoded in the spectrum.

The low-energy behaviour is qualitatively understood by realising that N_g acts as a quasi-momentum that alters the boundary condition of the problem [98]. To see this, perform a gauge transformation with $\hat{U} = e^{-i\hat{\phi}N_g/2}$ such that

$$\hat{U}(\hat{N} - N_g)\hat{U}^\dagger = \hat{N} \quad \Longrightarrow \quad \hat{U}\hat{H}\hat{U}^\dagger = E_C\hat{N}^2 - E_J\cos\hat{\phi}. \tag{1.42}$$

This transfers the Hamiltonian's explicit dependence on N_g to the wavefunction $|\psi\rangle \to |\psi'\rangle = \hat{U}|\psi\rangle$ instead, which no longer obeys periodic boundary conditions:

$$\langle\phi + 2\pi|\psi'\rangle = e^{-i\pi N_g}\langle\phi|\psi'\rangle. \tag{1.43}$$

In this gauge the "position" ϕ is better viewed as a non-compact coordinate describing a periodic extended cosine potential $-E_J\cos\phi$, while $|\psi'\rangle$ is a Bloch wavefunction with momentum $k = \pi N_g$.[29] Conclusions about the N_g spectrum follow immediately by comparison to the corresponding tight-binding problem. Namely, for $E_J/E_C \gg 1$ there is minimal

[29]The fixing of momentum to N_g distinguishes this setup from a truly extended lattice which has infinitely many degrees of freedom and hence a continuum of momenta and energies.

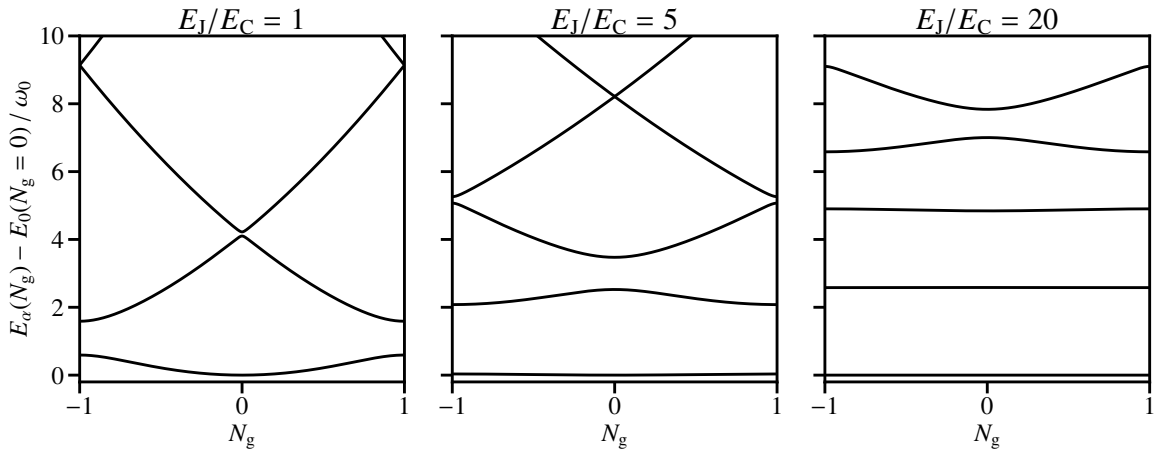

Fig. 1.9 The spectrum of the Cooper pair box as a function of the gate bias charge N_g. The spectrum is periodic under $N_g \to N_g + 2$ since it can be offset by adding a Cooper pair. The bandwidth of the lowest energy state decreases exponentially with E_J/E_C. The analogous oscillator frequency $\omega_0 \propto \sqrt{E_J E_C}$ is kept constant in each plot.

dispersion because the particle is well-localised at the bottom of the potential wells, which makes the modified boundary condition almost irrelevant. The processes that do involve $\phi \to \phi + 2\pi$ are rare *tunnelling* events, which we quantify in the next section.

1.3 Tunnelling and Instantons

Having appreciated the importance of tunnelling in the low-energy spectrum of Josephson junctions with charging effects, we now review the powerful method of *instantons* for accurately calculating tunnelling amplitudes [109].[30] Despite seeming excessive when applied to the CPB Hamiltonian (1.41), the method will be necessary when we later add fermions and couple them to the Josephson phase difference. It is this power to include other quantum fields or work in higher dimensions that means the method of instantons pervades theoretical high-energy physics [110, 111].

1.3.1 Euclidean Solutions

Although the appearance of imaginary time is taken for granted in the many-body path integral (our starting point in Chapter 3), we motivate the need for imaginary time in tunnelling problems by considering the simple problem of a particle encountering a potential barrier.

[30] Hereon, 'tunnelling' refers to phase slips of the superconducting phase difference ϕ, *not* the coherent tunnelling of Cooper pairs through the Josephson junction.

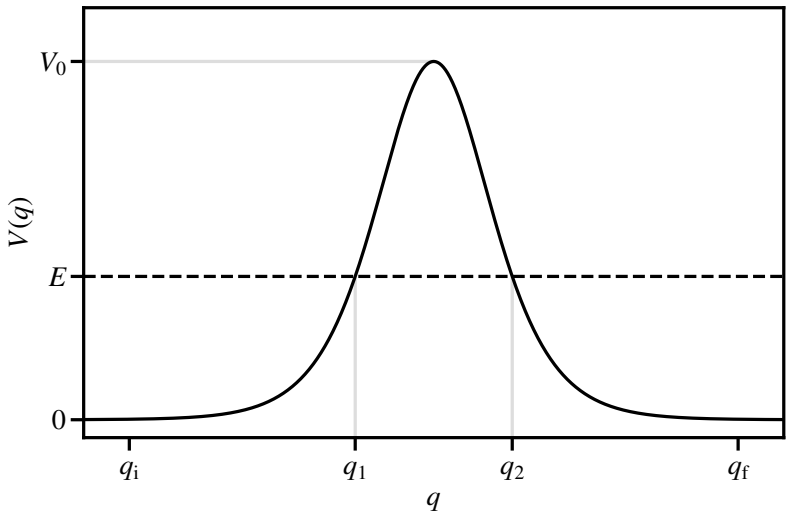

Fig. 1.10 A barrier potential with an incident particle from the left at energy E, which is below the barrier height V_0. The particle is able to penetrate the barrier due to quantum tunnelling. Classical turning points are labelled by q_1 and q_2.

This setting will be where we build our intuition for the Euclidean solutions of the more elaborate tunnelling problem we encounter later.

Consider a quantum mechanical particle in 1D with position $\hat{q}$ and momentum $\hat{p}$ encountering a potential barrier such as that in Figure 1.10, whose Hamiltonian is

$$\hat{H} = \frac{\hat{p}^2}{2m} + V(\hat{q})\,. \tag{1.44}$$

When the particle has energy E, which less than the height of the barrier V_0, most of the particle is reflected but a small part is transmitted. This part has an amplitude proportional to $e^{-B}[1+O(\hbar)]$, where from the Jeffreys-Wentzel-Kramers-Brillouin (JWKB) approximation we have $B = \frac{1}{\hbar}\int_{q_1}^{q_2} dq\sqrt{2m\,[V(q)-E]}$, with integration happening over the classically forbidden region $q \in (q_1, q_2)$. [This is not seen in any order of perturbation theory, since it vanishes more rapidly than any power of $\hbar$.] In this region, the total energy is less than the potential energy. If interpreting the difference as a negative kinetic energy, we would conclude that the velocity was imaginary, just as if it were the derivative of q with respect to an imaginary time. This gives a physical motivation for applying Euclidean analysis, even though it is somewhat trivial with one degree of freedom.

If we were to try and write this process as a path integral, we would write the propagator between positions q_i and q_f as

$$\langle q_\mathrm{f}|\, e^{-i\hat{H}T/\hbar}\, |q_\mathrm{i}\rangle = \int_{q(0)=q_\mathrm{i}}^{q(T)=q_\mathrm{f}} \mathcal{D}q\, e^{iS/\hbar}, \tag{1.45}$$

where the exponent is the familiar integral of the Lagrangian $S = \int dt \left[\frac{m}{2}\dot{q}^2 - V(q)\right]$. Clearly, the stationary-phase approximation fails to describe tunnelling processes: there is no classical solution of the real time action with tunnelling boundary conditions if $E < V_0$. This may tempt us to conclude that we cannot perform a semiclassical approximation to the tunnelling process, but the success of the standard JWKB approximation demonstrates that this conclusion must be untrue. The problem lies with the stationary-phase approximation in the path integral framework.

Now consider an analytic continuation $t \to -i\tau$ of the matrix element

$$\langle q_\mathrm{f}|\, e^{-i\hat{H}T/\hbar}\, |q_\mathrm{i}\rangle \to \langle q_\mathrm{f}|\, e^{-\hat{H}\beta/\hbar}\, |q_\mathrm{i}\rangle\,, \tag{1.46}$$

where $t \in [0,T) \to \tau \in [0,\beta)$. This new propagator also has a path integral representation with action

$$iS = i\int_0^T dt \left[\frac{m}{2}\dot{q}^2 - V(q)\right] \to \int_0^\beta d\tau \left[-\frac{m}{2}\dot{q}^2 - V(q)\right] = -\int_0^\beta d\tau \left[\frac{m}{2}\dot{q}^2 + V(q)\right] = -S_\mathrm{E}. \tag{1.47}$$

Thus, in addition to changing the factor of i in the exponential into a minus sign, the potential has been flipped upside down. Now there *do* exist solutions to the imaginary-time equations of motion with tunnelling boundary conditions, corresponding to saddle points of the Euclidean action S_E. Information about the low-energy spectrum follows by comparison to the spectral (or 'Lehmann') representation

$$\langle q_\mathrm{f}|\, e^{-\hat{H}\beta}\, |q_\mathrm{i}\rangle = \sum_n e^{-\beta E_n} \langle q_\mathrm{f}|n\rangle \langle n|q_\mathrm{i}\rangle \tag{1.48}$$

and its functional dependence on β as $\beta \to \infty$. (From now on we set $\hbar = 1$ so that $\beta \to \infty$ effects the $\beta/\hbar \to \infty$ limit.)

The analytical continuation feels artificial thus far—what has it achieved? It has identified the paths whose vicinities give the dominant contributions to the path integral in the semiclassical limit, which we can soon use to evaluate the path integral in the saddle-point approximation. With start and end points on different sides of the potential barrier, there were no stationary-action (i.e., classical) trajectories in real time: all trajectories with those

boundary conditions interfered very destructively. Yet, their cumulative effect can be extracted from a finite number of regions in the space of possible trajectories, namely those proximate to saddle points in imaginary time. So, while the tunnelling amplitude would have to be painfully calculated from the real-time path integral as a sum of interfering non-stationary paths, the dominant contributions are concentrated around classical paths in imaginary-time and are thus amenable to a saddle-point approximation. The destructive interference in the real-time path integral leaves its mark, however, which gives rise to the exponential suppression of the tunnelling amplitude in the size of the barrier [112].

1.3.2 The Dilute Instanton Gas for Periodic Potentials

We now return to the concrete problem of quantum tunnelling in Josephson junctions and expose the instanton calculation in detail.

Recall that the Hamiltonian in Eq (1.41) has a symmetry under $\phi \to \phi + 2\pi$, which will also be true of the microscopic Hamiltonian that generates the Josephson potential in Chapter 3.[31] Hence, physically, ϕ is compact on a $[0, 2\pi)$ interval. To spare ourselves a later translation of this section's results to the setup of Chapter 3, we will consider a Josephson potential with two minima at $\phi = 0$ and $\phi = \pi$ from the outset, with Hamiltonian

$$\hat{H} = E_{\mathrm{C}}(\hat{N} - N_{\mathrm{g}})^2 - E_{\mathrm{J}} \cos(2\hat{\phi}) \tag{1.49}$$

chosen for simplicity. We opt not to think of $\phi \to \phi + \pi$ as a general symmetry since we shall maintain that $\phi = 0$ and $\phi = \pi$ are inequivalent points. [Of course, the N_{g} spectra of the particular Hamiltonians (1.41) and (1.49) are related through 'BZ' folding, but we choose the folded picture.]

We express the imaginary-time propagator as a path integral, treating the periodicity of ϕ carefully:

$$\langle \phi_f | e^{-\hat{H}\beta} | \phi_i \rangle = \sum_w \int_{\phi_0 = \phi_i}^{\phi_\beta = \phi_f + 2\pi w} \mathcal{D}\phi \exp\left\{ - \int_0^\beta d\tau \left[\frac{1}{2} \frac{1}{8E_{\mathrm{C}}} (\partial_\tau \phi_\tau)^2 + i \frac{N_{\mathrm{g}}}{2} (\partial_\tau \phi_\tau) - E_{\mathrm{J}} \cos(2\phi_\tau) \right] \right\}. \tag{1.50}$$

[31] As made clear in Chapter 3, our situation will be entirely distinct from the so-called 4π Josephson effect [113] which occurs when a parity-preserving Josephson junction is formed between the ends of two topological superconducting wires A and B hosting MZMs $\hat{\gamma}'_A$ and $\hat{\gamma}''_B$ through a term $\propto i\hat{\gamma}'_A \hat{\gamma}''_B \cos(\phi/2)$.

Notice that ϕ_τ has become a non-compact variable lying anywhere on the real line,[32] allowed to have nontrivial winding $w \in \mathbb{Z}$. Correspondingly, the Josephson potential in the action is an infinite periodic potential, just as we argued from a wavefunction perspective in the previous section when we introduced N_g as an effective momentum.

We now look for the classical solutions of this action satisfying the saddle-point condition $\delta S = 0$. The exact differential term simply contributes $\frac{iN_g}{2}(\phi_f - \phi_i + 2\pi w)$ to the action. The Euler-Lagrange equations from the remaining terms give the motion of a particle with coordinate ϕ_τ in an inverted cosine potential, sketched in Figure 1.11. It is also sufficient to consider only paths with $\phi_f = \phi_i$, since these are the ones that appear in the partition function $Z = \int_0^{2\pi} d\phi \, \langle\phi| e^{-\hat{H}\beta} |\phi\rangle$, where β is the inverse temperature. The most important trajectories are those that start and end at the maxima $\phi = 0, \pi$ of the inverted potential, since these are the points that accumulate the least action. One obvious trajectory is for the particle to remain at rest at a maximum. Yet, from our intuition about classical mechanics, we additionally see that the particle may leave a maximum at $\phi = 0$ and accelerate through a minimum to reach another maximum at $\phi = \pi$, which is known as the *instanton* solution, depicted in Figure 1.11. (When ϕ advances by $-\pi$, we label it an *anti-instanton*.) After reaching the other maximum, the particle may stay there for an arbitrary amount of time before returning. We henceforth denote the potential by $V_\phi \equiv -E_J \cos(2\phi)$ for brevity. The instanton profile follows from the conservation of Euclidean energy,

$$\partial_\tau \phi_\tau^\star = 4\sqrt{E_C[V_{\phi_\tau^\star} - V_0]}. \tag{1.51}$$

[32] In deriving the path integral [114], one inserts resolutions of the identity $\mathbb{1} = \sum_{N_j \in \mathbb{Z}} \int_0^{2\pi} d\phi_j |\phi_j\rangle\langle\phi_j|N_j\rangle\langle N_j|$ at each time step, giving contributions $\cdots\langle\phi_j|N_j\rangle\langle N_j|\phi_{j-1}\rangle\cdots \propto e^{\sum_j N_j(\phi_j - \phi_{j-1})}$. The sums over N_j are traded for integrals with the Poisson summation formula $\sum_{N\in\mathbb{Z}} f(N) = \sum_\ell \int_{-\infty}^{\infty} dN\, f(N) e^{2\pi i \ell N}$, so that each $(\phi_j - \phi_{j-1}) \to (\phi_j + 2\pi\ell_j - \phi_{j-1})$. The key step is supplanting each ϕ_j with a non-compact variable $\phi'_j = \phi_j + 2\pi \sum_{k=1}^{j} \ell_k$ defined on $(-\infty, \infty)$, which removes the $\sum_{\ell_j}$ summations:

$$\prod_j \sum_{\ell_j} \int_0^{2\pi} d\phi_j e^{N_j(\phi_j + 2\pi\ell_j - \phi_{j-1})} = \prod_j \int_{-\infty}^{\infty} d\phi'_j e^{N_j(\phi'_j - \phi'_{j-1})}.$$

Implicit in this redefinition is that ϕ' satisfies the original boundary conditions *modulo* 2π. The standard form of the path integral then follows by performing the resulting Gaussian integrals over all N_j.

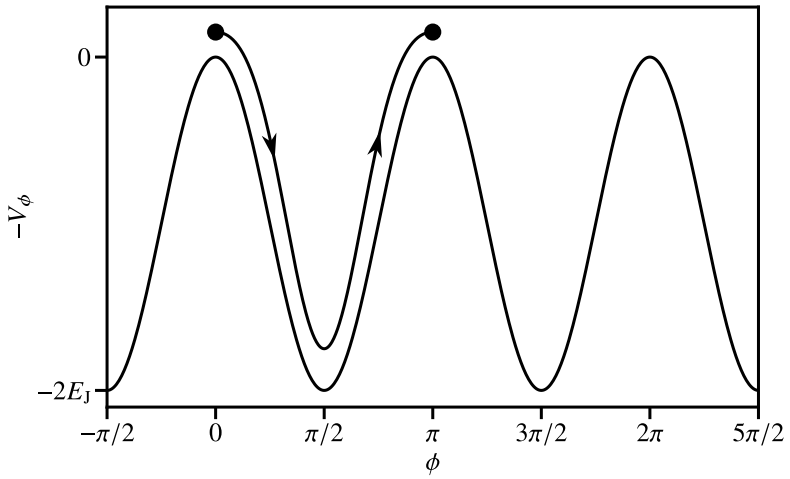

Fig. 1.11 A diagram showing the inverted cosine potential $-V_\phi = E_J \cos\phi$ and a classical instanton solution linking the maxima at $\phi = 0$ and $\phi = \pi$.

Its action (relative to the trivial action that would accumulate if the particle were to never leave) is found to depend only on the shape of the potential:

$$S^\star - V_0\tau = \int_0^\tau d\tau \left[\frac{1}{2}\frac{1}{8E_C}\left(\partial_\tau \phi_\tau^\star\right)^2 + V_{\phi_\tau^\star} - V_0\right] \tag{1.52}$$

$$= \int_0^\tau d\tau \left[\frac{1}{2\sqrt{E_C}}(\partial_\tau \phi_\tau^\star)\sqrt{V_{\phi_\tau^\star} - V_0}\right] = \frac{1}{2\sqrt{E_C}}\int_0^\pi d\phi \sqrt{V_{\phi_\tau^\star} - V_0}. \tag{1.53}$$

Each instanton has a timescale that we may estimate from Eq. (1.51) by approximating the potential minimum at $\phi = \pi$, say, as $V_\phi \approx \frac{V''}{2}(\phi - \pi)^2$, giving $\partial_\tau \phi_\tau^\star \approx -\sqrt{8E_C V''}(\phi_\tau^\star - \pi) \equiv -\omega(\phi_\tau^\star - \pi)$. At long times, $\tau \to \infty$, this integrates to $\phi_\tau^\star \to \pi - e^{-\omega\tau}$, showing that the temporal extent of an instanton is roughly reciprocal to the oscillator frequency of the wells.[33] Since each instanton is localised in time, there are approximate solutions to the equations of motion where many instantons appear in sequence, separated by times much greater than their widths, demonstrated in Fig. 1.12. As the path integral prescribes, we must sum over all these configurations of ϕ_τ to calculate the propagator. The resulting summation is called the *dilute instanton gas* [109]. Its validity hinges on the timescale for instantons being much shorter than typical instanton separations, which means that configurations of overlapping instantons constitute only a minuscule fraction of the space of summed trajectories. Also assumed is that the instantons barely interact at these long distances.

In summing all configurations, we group trajectories according to how many instantons and anti-instantons appear, counted by q and $\bar{q}$, respectively. It is heuristically clear that

[33] That this timescale is typically short is what inspired 't Hooft to coin the term "instant-on" [109].

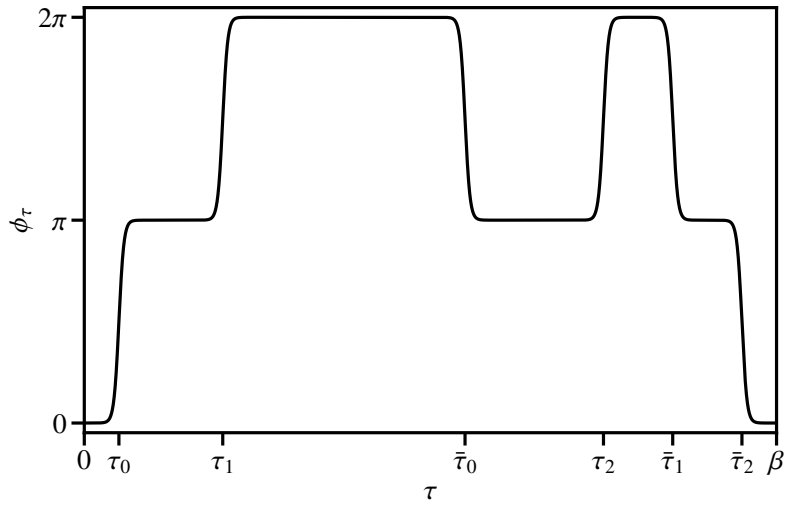

Fig. 1.12 Schematic representation of a phase profile ϕ_τ with zero winding $w = 0$ that contributes to the dilute instanton gas summation, composed of independent (anti-)instantons at times τ_j ($\bar{\tau}_j$). The timescale of instantons relative to inverse temperature β is exaggerated compared to the assumptions of the dilute instanton gas approximation.

trajectories with different q or $\bar{q}$ are not perturbatively related to each other, so these are stable quantities.[34] Instantons and anti-instantons may appear at any time and in any order, but each comes with an $e^{-S^\star}$ penalty, so the summation takes the form

$$Z \propto e^{-\beta(V_0+\omega/2)} \sum_w \sum_{q,\bar{q}=0}^{\infty} \delta_{w,\frac{q-\bar{q}}{2}} \int_0^\beta d\bar{\tau}_1 \int_{\bar{\tau}_1}^\beta d\bar{\tau}_2 \cdots \int_{\bar{\tau}_{\bar{q}-1}}^\beta d\bar{\tau}_{\bar{q}} \tag{1.54}$$

$$\int_0^\beta d\tau_1 \int_{\tau_1}^\beta d\tau_2 \cdots \int_{\tau_{q-1}}^\beta d\tau_q \, (Ke^{-S^\star})^{q+\bar{q}} e^{i\pi w N_\mathrm{g}}. \tag{1.55}$$

Here we included quantum fluctuation contributions ω and K that we choose not to evaluate, only to note that they come from perturbed classical trajectories [115]. We see above a competition between entropy and energetics that decides the typical density of instantons [114]. The configurational entropy simplifies to $\int_0^\beta d\tau_1 \int_{\tau_1}^\beta d\tau_2 \cdots \int_{\tau_{q-1}}^\beta d\tau_q = \frac{\beta^q}{q!}$ for both instanton species. The $\delta_{w,\frac{q-\bar{q}}{2}}$ factor ensures consistency between the number of instantons and the winding number, enforcing that q and $\bar{q}$ are simultaneously odd or even for ϕ_τ to start and end in a minimum of the same 0- or π-like type. It is therefore easiest to split up the summation

[34] In fact they label topologically distinct instanton sectors (in the mathematical sense).

into even and odd contributions:

$$Z \propto e^{-\beta(V_0+\omega/2)}\Bigg[\sum_{q=\text{odd}}^{\infty}\frac{\left(K\beta e^{-S^\star}e^{i\frac{\pi N_\text{g}}{2}}\right)^q}{q!}\sum_{\bar{q}=\text{odd}}^{\infty}\frac{\left(K\beta e^{-S^\star}e^{-i\frac{\pi N_\text{g}}{2}}\right)^{\bar{q}}}{\bar{q}!}+ \tag{1.56}$$

$$\sum_{q=\text{even}}^{\infty}\frac{\left(K\beta e^{-S^\star}e^{i\frac{\pi N_\text{g}}{2}}\right)^q}{q!}\sum_{\bar{q}=\text{even}}^{\infty}\frac{\left(K\beta e^{-S^\star}e^{-i\frac{\pi N_\text{g}}{2}}\right)^{\bar{q}}}{\bar{q}!}\Bigg]. \tag{1.57}$$

Recognising these as the hyperbolic functions, we apply the angle addition formula to conclude that

$$Z \propto e^{-\beta(V_0+\omega/2)}\cosh\left[2\beta K e^{-S^\star}\cos\left(\frac{\pi}{2}N_\text{g}\right)\right]. \tag{1.58}$$

This is the partition function of a two-level system with energies that disperse with N_g as

$$E_\pm(N_\text{g}) = V_0 + \frac{\omega}{2} \pm 2Ke^{-S^\star}\cos\left(\frac{\pi}{2}N_\text{g}\right), \tag{1.59}$$

as is expected for a tight-binding problem with nearest-neighbour hopping strength $t_{0\to\pi} = Ke^{-S^\star}$. (The quantity $Ke^{-S^\star}$ also sets the average instanton density $\langle q\rangle/\beta$ in the above summation, so its smallness justifies the diluteness approximation *a posteriori*.) Looking back at Figure 1.9 confirms that the same dispersion shape results from folding the spectrum of the $-E_\text{J}\cos\phi$ potential. We have thus found the $0 \to \pi$ tunnelling amplitude for the Josephson Hamiltonian (1.49), which will serve us well in Chapter 3 when we adapt this method to include topology-changing fermions.

Even in this simple 1D example that could equally have been treated with the JWKB approximation, the instanton approach has its advantages. Importantly, it gave us a controlled approximation [114] unlike JWKB.[35] The first-order result gave us the exponent for the tunnelling amplitude, while the prefactor K could in principle be calculated by performing the fluctuation integrals around classical instanton configurations.[36] The density of the instanton gas is also a parameter that can be pushed beyond the dilute limit.

[35] In JWKB, one expands the exponent of $\psi(q) = e^{i\Phi(q)/\hbar}$ to a certain order in $\hbar^n$, solves differential equations and matching conditions (that are increasingly unwieldy in n), then hopes that the result is accurate.

[36] The second-order Gaussian fluctuation integrals require calculating a functional determinant $K \propto \det\left(-\frac{1}{8E_\text{C}}\partial_\tau^2 + V''_\phi\right)$, whose detailed calculation is found in Refs. [115, 116].

1.4 Thesis Outline

With this conceptual understanding of modern topological superconductors and the method of instantons, we are ready to present novel results. The content of the rest of the thesis has been adapted from the following articles published during my PhD:

- **Elis Roberts**, Jan Behrends and Benjamin Béri. Physical Review **B** 101, 155133 (2020)
  Second-Order Bulk-Boundary Correspondence in Rotationally Symmetric Topological Superconductors from Stacked Dirac Hamiltonians

- **Elis Roberts**, Jan Behrends and Benjamin Béri. arXiv:2112.14280
  Quantum Tunneling in the Presence of a Topology-Changing Fermionic Bath

These form the basis of Chapters 2 and 3, respectively. In Chapter 2 we see how the rotation representations associated with a symmetry-indicated topological phase can be used to diagnose second-order topology in 2D superconductors, manifesting as 0D corner-MZMs. This is done systematically by mapping changes in bulk symmetry representations to constraints on how chiral edge modes may gap out. In Chapter 3 we consider the general scenario of topological fermions coupled to a boson whose dynamics are described by tunnelling events. We find that the topology change of the fermions suppresses tunnelling using an example rooted in Josephson junction MZM platforms that include charging effects. We summarise these findings in Chapter 4 and present possible directions for future research.

Chapter 2

Second-order bulk-boundary correspondence in rotationally symmetric topological superconductors

2.1 Motivation

The classification of topological phases of matter, as we argued in Chapter 1, is one of the cornerstones of modern condensed-matter physics. Depending on their dimensionality and the presence of antiunitary symmetries, gapped noninteracting Hamiltonians may fall into topologically distinct sectors characterised by sets of topological invariants [16, 17, 117]. We further saw that crystalline symmetries enrich the classification of topological insulators and superconductors, giving rise to a wider class of materials called crystalline topological insulators [36, 118, 119, 33, 120, 10, 38, 47, 48]. The interplay of crystalline and antiunitary symmetries makes the topological classification a challenging task, as there are for example 230 space groups in three dimensions, allowing for a plethora of symmetry-protected topological phases partially characterised by various symmetry indicators [36, 121, 56, 38, 47, 48, 122–124, 50] that we reviewed in Sec. 1.1.4.

One main goal of the symmetry classification of topological insulators and superconductors is to establish a correspondence between the invariants defined in the bulk and in-gap states that arise at the surfaces [125–127]. In crystalline topological insulators, this bulk-boundary correspondence links the bulk invariants to gapless modes at surfaces that respect the underlying spatial symmetries [36, 118, 119].

Spatial symmetries may also give rise to higher-order topological insulators and superconductors. As we introduced in Sec. 1.1.5, these phases have gapped boundaries, but host

"higher-order boundary modes": gapless boundary-excitations of codimension greater than one, e.g., bound to their hinges or corners [68, 67, 69, 65]. Higher-order topological phases have been studied in systems protected by order-two symmetries (e.g., reflection and inversion symmetry [68, 67, 69, 128, 46, 129]), rotational invariance [66, 65, 71], and combinations of the above [130–132]. Gapless hinge and corner excitations may also appear in interacting models [133, 97], Floquet phases [134, 135] and can coexist with gapless surface states [136]. Higher-order topology does not necessarily rely on an underlying regular lattice [137], but can be also found in quasicrystals respecting certain spatial symmetries [138, 139]. Corner modes have been found experimentally in various metamaterials, including phononic lattices [140], engineered electronic lattices [141], topolectrical [142] and microwave circuits [143]. Strong experimental evidence further suggests the existence of hinge modes in bismuth [132].

In higher-order topological phases, the presence and robustness of boundary modes depends on how the underlying spatial symmetries transform the degrees of freedom of neighbouring surfaces into another. This raises the question of how to relate this transformation of neighbouring surfaces to topological invariants defined in the bulk. Establishing this relationship amounts to deriving a bulk-boundary correspondence in a manner that keeps the role of the defining symmetries transparent. This has been the guiding principle behind recent work relating symmetry indicators to higher-order boundary modes in insulators [37, 144], and it has also been a key element in the work of Trifunovic and Brouwer establishing the bulk-boundary correspondence for higher-order topological phases with order-two symmetries in the absence of weak (i.e., lower dimensional) invariants [46, 129]. Here we describe how such a bulk-boundary correspondence program can be carried out beyond these cases, focussing on two-dimensional (2D) crystalline superconductors with n-fold rotational symmetry (i.e., C_n symmetry), and allowing for nonvanishing weak invariants. Establishing a link between edge transformation properties and bulk invariants provides an illuminating perspective complementary to counting arguments based on bulk defect classifications [121, 56], and gives results consistent with examples based on very recent extensions of symmetry indicators to the superconducting classes [145, 49].

Our approach is based on an effective description in terms of stacked Dirac models [122, 37] like those introduced in Sec. 1.1.3. Using this, we show that rotational invariance dictates a relationship between adjacent surfaces and that this may give rise to protected second-order boundary modes in the form of Majorana bound states. We express this bulk-boundary correspondence in terms of the bulk invariants for rotationally symmetric crystalline superconductors developed in Ref. [56] and an additional contribution signifying the combined effects of weak topological invariants and the physical rotation centre. While our considerations are general, for the purposes of a detailed exposition we will be focusing

on C_4-symmetric systems: of the C_2, C_3, C_4, and C_6 symmetries possible in 2D crystals, the C_4-symmetric case is the one displaying the richest combination of stacked Dirac and second-order topological superconducting features. (We shall comment on applying our methods to the other cases in a Sec. 2.5.) To demonstrate the validity of our stacked Dirac approach, we also illustrate our results on several concrete lattice models.

In what follows, for brevity we shall refer to the second order Majorana bound states we find as corner modes, even though rotational symmetry does not, strictly speaking, require them to be at the geometrical corners of the system: Their position can be moved in a rotation-symmetric manner e.g., by adding suitable Kitaev chains to the boundary [65, 121]. However, such a deformation merely shifts the Majorana bound states around the boundary without altering their position relative to each other and, as such, it cannot gap out the Majoranas. In what follows, the term *corner mode* should thus be understood up to such Kitaev chain deformations.

This Chapter is organised as follows: After briefly summarizing the symmetry classification of rotationally invariant superconductors [56] in Sec. 2.2, we introduce our stacked Dirac model based approach in Sec. 2.3. We present an effective edge theory and consider the most general mass terms that gap out the edge modes. To relate the bulk description to the boundaries, we relate the topologically distinct rotation properties of the boundary mass term to the bulk invariants in Sec. 2.4. We show some explicit examples in Sec. 2.6 and conclude in Sec. 2.7. In Appendix A, we clarify the role of the unit cell and explicitly derive the edge Hamiltonian.

2.2 Bulk Topological Classification

We work with 2D topological crystalline superconductors in class D. These are particle-hole (PH) symmetric systems which admit an effectively single-particle Bogoliubov-de-Gennes (BdG) Hamiltonian. Working in momentum space and denoting this BdG Hamiltonian by $\mathcal{H}(\mathbf{k})$ at momentum $\mathbf{k}$ in the Brillouin zone (BZ), PH symmetry is given by

$$\Xi\mathcal{H}(\mathbf{k})\Xi^{-1} = -\mathcal{H}(-\mathbf{k}), \tag{2.1}$$

where Ξ is an antiunitary operator satisfying $\Xi^2 = +1$.

The presence of an additional n-fold rotational symmetry C_n allows for a richer topological classification [56, 50, 66] than if the only symmetry was PH symmetry. We now review the classification scheme devised by Benalcazar *et al.* for classifying crystalline superconductors with rotational symmetry [56]. This is a concrete implementation of the symmetry indicator

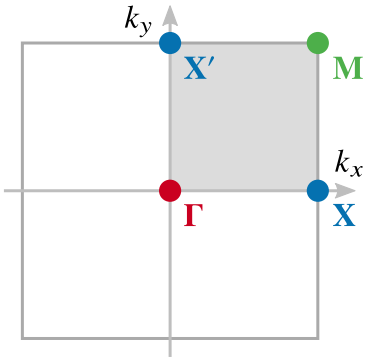

Fig. 2.1 The Brillouin zone for C_4-symmetric models. There are two fourfold fixed points labelled $\mathbf{\Gamma}$ and $\mathbf{M}$, and two twofold fixed points $\mathbf{X}$ and $\mathbf{X}'$ that transform into each other upon a fourfold rotation. The shaded region indicates the fundamental domain that generates the entire BZ.

approach to classifying crystalline topological phases, whose principles we laid out in Sec. 1.1.4, which is to use the symmetry representations of occupied bands at high symmetry points in the BZ [36, 123, 124, 121].

What follows is an abridged version of Sec. 1.1.4 specific to rotational symmetry in 2D. The rotational symmetry of the model is expressed through the relation

$$r_n \mathcal{H}(\mathbf{k}) r_n^\dagger = \mathcal{H}(R_n \mathbf{k}), \tag{2.2}$$

where r_n is an n-fold rotation operator obeying $r_n^n = -\mathbb{1}$ and R_n is the SO(2) matrix for n-fold rotations in the 2D plane. Since r_n conserves charge, it commutes with the PH symmetry operator $[\Xi, r_n] = 0$ [56]. (There are some subtleties to this statement if Cooper pairs have nonzero angular momentum, which we defer until Sec. 2.5.3 because it doesn't impact the analysis.) The $r_n^n = -\mathbb{1}$ requirement comes from the fact that r_n is a single particle operator acting on a particle with half-odd-integer spin (a fermion), for which a Berry phase of -1 is acquired under a full 2π rotation. Since these are *crystalline* superconductors, the BZ contains certain high-symmetry points (HSPs) $\mathbf{\Pi}^{(n)}$, which are invariant under rotation $R_n \mathbf{\Pi}^{(n)} = \mathbf{\Pi}^{(n)}$ up to a reciprocal lattice vector. At these points, the rotational symmetry is simply $[r_n, H(\mathbf{\Pi}^{(n)})] = 0$, and as such the momentum eigenstates can be chosen as eigenstates of the rotation operator. This allows us to label each state at $\mathbf{\Pi}^{(n)}$ with its rotation eigenvalue

$$\Pi_p^{(n)} = e^{i\pi(2p-1)/n}, \qquad \text{for } p = 1, 2, \ldots n. \tag{2.3}$$

For example, in a C_4-symmetric BZ (shown in Figure 2.1), there are both fourfold and twofold fixed points, whose rotation eigenvalues are shown in Figure 2.2.

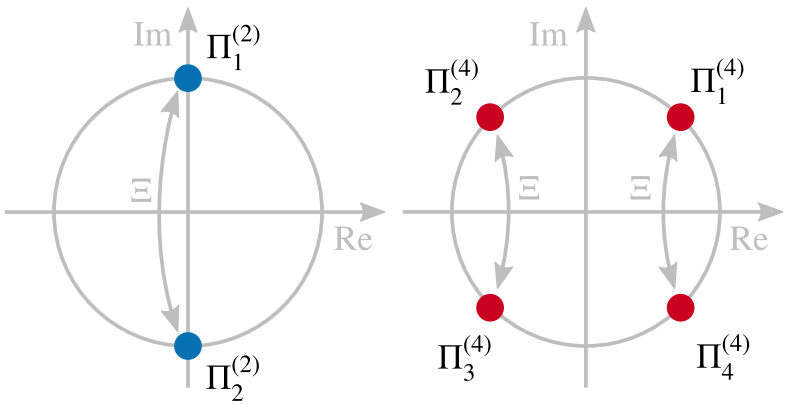

Fig. 2.2 The rotation eigenvalues for C_2 and C_4 symmetry, respectively. The PH operator relates complex conjugate pairs of rotation eigenvalues (while also switching between positive and negative energy bands).

We now outline how these rotation eigenvalues are used to topologically classify gapped superconductors in two dimensions. We start by defining a trivial superconductor as one that can be connected to a superconductor in the atomic limit without closing the gap and while respecting the same crystalline and PH symmetries throughout. Here the 'atomic limit' is understood as a symmetry-respecting array of zero-dimensional superconductors [49]. For crystal structures compatible with a symmetric boundary, as we note is required for a generic bulk-boundary correspondence (see Appendix A.1), a unit cell can be chosen such that an atomic limit superconductor's ground state wave function has no momentum-dependent features. With this more restricted definition of topological equivalence (because it involves obeying an additional unitary symmetry), the boundary between two inequivalent phases does not necessarily possess edge states, as we explore in this Chapter. For the ground state wave function to have no momentum-dependent features, the rotation eigenvalues of the negative energy states (which, within the BdG description, are all occupied in the ground state) must be the same at all HSPs in the BZ. This motivates the definition of the topological invariants as

$$[\Pi_p^{(n)}] \equiv \#\Pi_p^{(n)} - \#\Gamma_p^{(n)}, \tag{2.4}$$

where $\#\Pi_p^{(n)}$ is the number of negative energy BdG bands with eigenvalue $\Pi_p^{(n)}$. Intuitively, these are chosen because occupancies of rotation eigenvalues will not change unless there is a gap closing, and taking the difference relative to a reference momentum [chosen as $\mathbf{\Gamma}$ in Eq. (2.4)] is required for the invariants to be stable under the addition of trivial bands. Under this definition, a C_n-symmetric superconductor is topological if $[\Pi_p^{(n)}]$ is nonzero for any p.

A complete topological characterisation requires establishing the set of independent $[\Pi_p^{(n)}]$. They are not all independent because rotational symmetry constrains the rotation

eigenvalues at C_n-related points in the BZ to be the same (e.g., the C_2 eigenvalues of the C_4-related $\mathbf{X}$ and $\mathbf{X}'$ in the fourfold case, shown in Fig. 2.1). PH symmetry places further restrictions on these invariants, since if the rotation eigenvalue of a state is $\Pi_p^{(n)}$, its PH-conjugate state has eigenvalue $\Pi_p^{(n)*} = \Pi_{n-p+1}^{(n)}$. That is to say, the number of occupied eigenvalues $\Pi_p^{(n)}$ is equal to the number of *unoccupied* eigenvalues $\Pi_{n-p+1}^{(n)}$, which implies

$$[\Pi_p^{(n)}] = -[\Pi_{n-p+1}^{(n)}]. \tag{2.5}$$

For C_4-symmetric systems there are three independent rotation invariants [56],

$$[X] \equiv \#X_1 - (\#\Gamma_1 + \#\Gamma_3), \tag{2.6a}$$
$$[M_1] \equiv \#M_1 - \#\Gamma_1, \tag{2.6b}$$
$$[M_2] \equiv \#M_2 - \#\Gamma_2, \tag{2.6c}$$

which, in conjunction with the Chern number Ch, fully classify the bulk topology in this symmetry class.

2.2.1 Importance of Rotation Centre

In the previous section, we started with the rotational symmetry relation Eq. (2.2), but a system with periodic boundary conditions can have many centres of rotation [124, 146], as exemplified in Fig. 2.3. Although operators implementing rotation about different centres are easily related through composition with translation operators, the classification of periodic Hamiltonians summarised above relies on a momentum-independent rotation operator [56], which can only be true for one of the rotation centres. Since a finite system with boundaries may only satisfy rotational symmetry about one of the rotation centres, the physical symmetry operator relating different edges of a finite system may be *different* (but closely related) to the symmetry operator used to classify periodic Hamiltonians in Ref. [56]. In this section we explicitly relate these distinct rotation operators in the case of C_4 symmetry, which allows for two rotation centres that we refer to as A and B.

Rotation Centre A

We now explicitly derive the rotation operator in momentum-space for case A depicted in Fig. 2.3, in a similar spirit to Ref. [124]. Let lattice sites be situated at $\mathbf{R} = n_1\mathbf{a}_1 + n_2\mathbf{a}_2$, where $n_i \in \mathbb{Z}$ are integer coefficients of primitive lattice vectors $\mathbf{a}_i$. Associated with each lattice site are orbitals α located at atomic positions $\mathbf{d}_\alpha$ within a unit cell, such that many orbitals

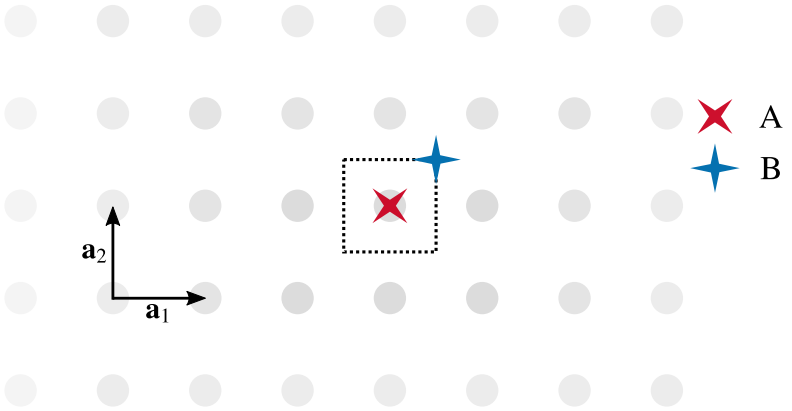

Fig. 2.3 Two options (A and B) for the rotation centre in an infinite C_4-symmetric lattice. The dotted box shows a primitive unit cell with its associated lattice site in the middle. Case B has its rotation operator shifted by $\mathbf{c} = \frac{1}{2}(\mathbf{a}_1 + \mathbf{a}_2)$

may share the same atomic position. Consider the position of a particular orbital, given by $\mathbf{r} \equiv \mathbf{R} + \mathbf{d}_\alpha$. Let R_A be defined as a pure rotation R_n about the origin which coincides with a lattice site. If this operation is to be a symmetry, then an atom located at $\mathbf{r}$ must be mapped to another atomic site so that

$$R_A : \mathbf{r} \to R_n \mathbf{r} = R_n(\mathbf{R} + \mathbf{d}_\alpha) = \mathbf{R}' + \mathbf{d}_\beta, \tag{2.7}$$

for some other lattice point $\mathbf{R}'$ and atomic site $\mathbf{d}_\beta$. A key point to note is that for certain lattices one *cannot* choose a basis in the unit cell such that $\mathbf{R}' = R_n \mathbf{R}$ for all $\mathbf{d}_\alpha$, as we soon explain in more detail. In second-quantised notation the operator $\hat{R}_A$ changes the position of each atomic orbital as

$$\hat{R}_A \hat{c}^\dagger_\alpha(\mathbf{R} + \mathbf{d}_\alpha)\hat{R}_A^{-1} = \hat{c}^\dagger_\beta(\mathbf{R}' + \mathbf{d}_\beta)\mathcal{R}_{\beta\alpha}, \tag{2.8}$$

which includes a unitary matrix $\mathcal{R}_{\beta\alpha}$ (with implicit summation over orbitals β) to account for rotation amongst atomic orbitals, whose elements $\mathcal{R}_{\beta\alpha}$ are only nonzero when $\mathbf{d}_\alpha \to \mathbf{d}_\beta$. Our Fourier transform convention has the periodic phase taken with respect to lattice sites, such that momentum space operators are given by[1]

$$\hat{c}^\dagger_\alpha(\mathbf{k}) = \frac{1}{\sqrt{N}} \sum_{\mathbf{R}} \hat{c}^\dagger_\alpha(\mathbf{R} + \mathbf{d}_\alpha) \exp(i\mathbf{k} \cdot \mathbf{R}), \tag{2.9}$$

[1]This Fourier transform convention implies a certain choice of basis functions [147, 148]. For details on the basis choice cf. Appendix A.1.

which transform as [124]

$$\begin{aligned}\hat{R}_A\hat{c}^\dagger_\alpha(\mathbf{k})\hat{R}_A^{-1} &= \frac{1}{\sqrt{N}}\sum_{\mathbf{R}}\hat{R}_A\hat{c}^\dagger_\alpha(\mathbf{R}+\mathbf{d}_\alpha)\hat{R}_A^{-1}\exp(i\mathbf{k}\cdot\mathbf{R})\\ &= \frac{1}{\sqrt{N}}\sum_{\mathbf{R}}\hat{c}^\dagger_\beta(\mathbf{R}'+\mathbf{d}_\beta)\mathcal{R}_{\beta\alpha}\exp(i\mathbf{k}\cdot\mathbf{R})\\ &= \frac{1}{\sqrt{N}}\sum_{\mathbf{R}'}\hat{c}^\dagger_\beta(\mathbf{R}'+\mathbf{d}_\beta)\mathcal{R}_{\beta\alpha}e^{i\mathbf{k}\cdot(R_n^T\mathbf{R}'+R_n^T\mathbf{d}_\beta-\mathbf{d}_\alpha)}\\ &= \hat{c}^\dagger_\beta(R_n\mathbf{k})\mathcal{R}_{\beta\alpha}e^{i(R_n\mathbf{k})\cdot(\mathbf{d}_\beta-R_n\mathbf{d}_\alpha)}.\end{aligned} \tag{2.10}$$

This shows that the basis spinors $\hat{\xi}^\dagger_{\mathbf{k}} = \bigoplus_\alpha\left(\hat{c}^\dagger_\alpha(\mathbf{k}),\hat{c}_\alpha(-\mathbf{k})\right)$ of the second-quantised Hamiltonian

$$\hat{H} = \frac{1}{2}\int\frac{d^2\mathbf{k}}{(2\pi)^2}\hat{\xi}^\dagger_{\mathbf{k}}\mathcal{H}(\mathbf{k})\hat{\xi}_{\mathbf{k}}, \tag{2.11}$$

transform as

$$\begin{aligned}\hat{R}_A\hat{\xi}^\dagger_{\mathbf{k}}\hat{R}_A^{-1} &= \bigoplus_\alpha\left(\hat{R}_A\hat{c}^\dagger_\alpha(\mathbf{k})\hat{R}_A^{-1},\,\hat{R}_A\hat{c}_\alpha(-\mathbf{k})\hat{R}_A^{-1}\right)\\ &= \bigoplus_\alpha\left(\hat{c}^\dagger_\beta(R_n\mathbf{k})\mathcal{R}_{\beta\alpha},\hat{c}_\beta(-R_n\mathbf{k})\mathcal{R}^*_{\beta\alpha}\right)e^{i(R_n\mathbf{k})\cdot(\mathbf{d}_\beta-R_n\mathbf{d}_\alpha)}\\ &\equiv \hat{\xi}^\dagger_{R_n\mathbf{k}}r_n(\mathbf{k}).\end{aligned} \tag{2.12}$$

(Note that Refs. [52, 49] consider more general phase choices for the matrix $\mathcal{R}^*$ in the hole sector depending on the symmetry of the superconducting pairing term, which we discuss in Section 2.5.3.) Rotational invariance of the second-quantised Hamiltonian $\hat{R}_A\hat{H}\hat{R}_A^{-1} = \hat{H}$ implies that the Bloch Hamiltonian needs to satisfy

$$r_n(\mathbf{k})\mathcal{H}(\mathbf{k})r_n^\dagger(\mathbf{k}) = \mathcal{H}(R_n\mathbf{k}). \tag{2.13}$$

In general, the momentum-dependent part $e^{i(R_n\mathbf{k})\cdot(\mathbf{d}_\beta-R_n^T\mathbf{d}_\alpha)}$ of $r_n(\mathbf{k})$ is not a complex phase universal to all orbitals because $\mathbf{d}_\beta$ may lie in a different unit cell than $R_n\mathbf{d}_\alpha$ for certain α. This occurs, for example, when atoms are situated at the edge of a unit cell. If it is impossible to define a C_n-symmetric unit cell without atoms on the edges of the cell, then the rotation operator is generally not momentum-independent and the classification scheme of Ref. [56] (in its current form) does not hold; cf. Appendix A.1 for details. Lattices of the same type also present an impediment for formulating a bulk-boundary correspondence: When the atomic sites lie at the edge of a unit cell, it is impossible to tile a finite rotationally symmetric system without resorting to an extensive number of partial unit cells at the boundary. Any

classification scheme for such a system would be non-generic, as it needs to take into account the lattice termination. When all atoms lie wholly within the unit cell, which respects rotational invariance individually, we can indeed have $R_n\mathbf{d}_\alpha = \mathbf{d}_\beta$ for all orbitals α such that $e^{i(R_n\mathbf{k})\cdot(\mathbf{d}_\beta - R_n\mathbf{d}_\alpha)} = 1$, recovering Eq. (2.2) with $r_n(\mathbf{k}) \to r_n$. Henceforth, when simply referring to the unit cell, we shall be working with this restricted C_n-symmetric unit cell notion that allows for a well-defined bulk-boundary correspondence.

Rotation Centre B

Now consider a different operation R_B which consists of a pure rotation R_n about a different centre which is shifted by a vector $\mathbf{c}$. Different lattices have different options for $\mathbf{c}$ as long as a rotation about $\mathbf{c}$ maps lattice sites to other lattice sites. In the case of C_4 symmetry there is only the option of $\mathbf{c} = \frac{1}{2}(\mathbf{a}_1 + \mathbf{a}_2)$, shown in Fig. 2.3. Lattice sites are still situated at $\mathbf{R} = n_1\mathbf{a}_1 + n_2\mathbf{a}_2$, and we again consider a particular orbital located at position $\mathbf{r} = \mathbf{R} + \mathbf{d}_\alpha$. The rotation R_B then changes each position

$$R_B : \mathbf{r} \to R_n(\mathbf{r} - \mathbf{c}) + \mathbf{c} = R_n(\mathbf{R} + \mathbf{d}_\alpha) + (1 - R_n)\mathbf{c} \tag{2.14}$$

$$= \mathbf{R}' + \mathbf{d}_\beta + (1 - R_n)\mathbf{c}, \tag{2.15}$$

i.e., it can be considered a combination of the rotation R_A about the origin and an additional translation by $(1 - R_n)\mathbf{c}$. In second-quantised notation, the rotation changes the creation operators as

$$\hat{R}_B \hat{c}^\dagger_\alpha(\mathbf{R} + \mathbf{d}_\alpha)\hat{R}_B^{-1} = \hat{c}^\dagger_\beta(\mathbf{R}' + \mathbf{d}_\beta + [1 - R_n]\mathbf{c})\mathcal{R}_{\beta\alpha}, \tag{2.16}$$

which includes the additional translation by a lattice vector $(1 - R_n)\mathbf{c}$. It is important to note that even with this shift, the transformation of orbitals into each other is the same as before, i.e., $\mathcal{R}_{\alpha\beta}$ is the same as it was for R_A. With the same Fourier transform convention, we see

that the momentum space operators now transform as

$$\begin{aligned}
\hat{R}_B\hat{c}^\dagger_\alpha(\mathbf{k})\hat{R}_B^{-1} &= \frac{1}{\sqrt{N}}\sum_{\mathbf{R}}\hat{R}_B\hat{c}^\dagger_\alpha(\mathbf{R}+\mathbf{d}_\alpha)\hat{R}_B^{-1}\exp(i\mathbf{k}\cdot\mathbf{R}) \\
&= \frac{1}{\sqrt{N}}\sum_{\mathbf{R}}\hat{c}^\dagger_\beta(\mathbf{R}'+\mathbf{d}_\beta+[1-R_n]\mathbf{c})\mathcal{R}_{\beta\alpha}e^{i\mathbf{k}\cdot\mathbf{R}} \\
&= \frac{1}{\sqrt{N}}\sum_{\mathbf{R}'}\hat{c}^\dagger_\beta(\mathbf{R}'+\mathbf{d}_\beta+[1-R_n]\mathbf{c})\mathcal{R}_{\beta\alpha}e^{i\mathbf{k}\cdot(R_n^T[\mathbf{R}'+\mathbf{d}_\beta]-\mathbf{d}_\alpha)} \\
&= \frac{1}{\sqrt{N}}\sum_{\mathbf{R}'}\hat{c}^\dagger_\beta(\mathbf{R}'+\mathbf{d}_\beta)\mathcal{R}_{\beta\alpha}e^{i(R_n\mathbf{k})\cdot\mathbf{R}'}e^{i\mathbf{k}\cdot(R_n^T\mathbf{d}_\beta-\mathbf{d}_\alpha-[R_n^T-1]\mathbf{c})} \\
&= \hat{c}^\dagger_\beta(R_n\mathbf{k})\mathcal{R}_{\beta\alpha}e^{i(R_n\mathbf{k})\cdot(\mathbf{d}_\beta-R_n\mathbf{d}_\alpha)}e^{-i\mathbf{k}\cdot(R_n^T-1)\mathbf{c}}. \qquad (2.17)
\end{aligned}$$

Comparing Eq. (2.17) to Eq. (2.10), we see that the rotation operators are related by a momentum-dependent phase

$$\hat{R}_B\hat{c}^\dagger_\alpha(\mathbf{k})\hat{R}_B^{-1} = \hat{R}_A\hat{c}^\dagger_\alpha(\mathbf{k})\hat{R}_A^{-1}\,e^{-i\mathbf{k}\cdot(R_n^T-1)\mathbf{c}}. \qquad (2.18)$$

This extra phase is α-independent, so that the basis spinors transform as

$$\begin{aligned}
\hat{R}_B\hat{\xi}^\dagger_{\mathbf{k}}\hat{R}_B^{-1} &= \hat{\xi}^\dagger_{R_n\mathbf{k}}r_n e^{-i\mathbf{k}\cdot(R_n^T-1)\mathbf{c}} \qquad (2.19)\\
&\equiv \hat{\xi}^\dagger_{R_n\mathbf{k}}r_{n,\mathbf{c}}(\mathbf{k}), \qquad (2.20)
\end{aligned}$$

where we introduce a new notation for the rotation operator such that $r_n \equiv r_{n,\mathbf{c}=\mathbf{0}}$. Of note is that the momentum-independence of r_n necessarily implies a momentum-dependence for $r_{n,\mathbf{c}\neq\mathbf{0}}(\mathbf{k})$. The symmetry relation of the Bloch Hamiltonian is indifferent to this complex phase and is still given by Eq. (2.13).

Physical Rotation Operator

When a superconducting Hamiltonian is terminated in space, only one of $\hat{R}_A$ or $\hat{R}_B$ can be a symmetry of the whole system $\hat{H}$ since both rotation centres are mutually incompatible. Thus, eigenstates of $\hat{H}$ are simultaneously eigenstates of either $\hat{R}_A$ or $\hat{R}_B$. For the bulk (not terminated) system, at HSPs $\mathbf{\Pi}^{(n)}$ in momentum space, one has $r_{n,\mathbf{c}}(\mathbf{\Pi}^{(n)}) = \pm r_n$ because $e^{i\mathbf{\Pi}^{(n)}\cdot(R_n^T-1)\mathbf{c}} = \pm 1$ for any valid rotation centre $\mathbf{c}$, though $r_{n,\mathbf{c}}(\mathbf{\Gamma}) = r_n$ always. When we construct an effective bulk theory in the next section, references to the rotation operator are always to the operator r_n used to classify bulk Hamiltonians, but when we proceed to deriving the rotational symmetry of the edge theory we need to consider the physical rotation operator $r_{n,\mathbf{c}}(\mathbf{k})$.

2.3 Stacked Dirac Models and Boundary Theory

We seek a mapping from the full classification of Ref. [56] summarised in Sec. 2.2 to the second-order boundary signature. We consider superconductors without conventional gapless edge states, therefore we focus on the Ch = 0 case of vanishing Chern number. As stated in the Introduction, our exposition is focused on C_4 symmetry; the modifications required to treat C_2 and C_6 cases are discussed in Appendix 2.5. Since Majorana modes must always come in pairs, a C_3-symmetric system is not able to sustain unpaired Majoranas on its three corners, so we ignore this case entirely.

Our approach is the construction of a continuum model which allows us to describe interfaces between systems with different topological invariants, reminiscent of a Jackiw-Rebbi approach [31, 149].

2.3.1 Stacked Dirac Models

We determine the boundary signature for each topological phase based on a description near the gap closing transitions that change the topology. The previously defined invariants $[X]$, $[M_1]$ and $[M_2]$ only change for gap closings at HSPs $\mathbf{\Pi}^{(n)}$, though Ch also changes for gap closings at any generic momenta. Due to C_4 symmetry, gap closings at generic momenta $\mathbf{k}_0$ (not HSPs) must come in multiplets of four (at $R_4^j\mathbf{k}_0$ with $j = 0, 1, 2, 3$), which changes the Chern number by ±4. As these gap closings at generic momenta can be smoothly shifted to a high-symmetry point, henceforth we consider that all gap closings occur at the HSPs $\mathbf{\Pi}^{(n)}$.

Near a transition at a HSP $\mathbf{\Pi}_\alpha$, a natural description is provided by a massive 2D Dirac Hamiltonians $\mathcal{H}^\alpha_{\mathbf{\Pi}_\alpha}(\mathbf{k})$, with a sign change of the mass across the interface modelling a boundary between regions with different values of their bulk topological invariants. (The momentum $\mathbf{k}$ here is understood relative to $\mathbf{\Pi}_\alpha$.) We will then link the rotation properties encoded in the rotation invariants of Eq. (2.6) to properties of these Dirac fermions. Working with a Dirac model means that our anticipated bulk-boundary correspondence will be in terms of the *difference* between topological phases, which indeed is the most general scenario to which a bulk- boundary correspondence can apply [126]. For any change in topological phase there are multiple possible stacked Dirac realisations, but we will show that the boundary signature follows from a feature common to all of these realisations.

The effective model $\mathcal{H}_{\text{eff}}(\mathbf{k})$ is the direct addition of all these Dirac Hamiltonians, which we refer to as a "stack" of Dirac models $\mathcal{H}^\alpha_{\mathbf{\Pi}_\alpha}(\mathbf{k})$, written as

$$\mathcal{H}(\mathbf{k}) \to \mathcal{H}_{\text{eff}}(\mathbf{k}) = \bigoplus_\alpha \mathcal{H}^\alpha_{\mathbf{\Pi}_\alpha}(\mathbf{k}). \tag{2.21}$$

Physically, this corresponds to stacking many systems together and leaving them decoupled, but with the overall system remaining 2D. We have introduced a (redundant) label $\mathbf{\Pi}_\alpha$ to emphasize the origin of each Dirac Hamiltonian for clarity. Each Dirac model has the same chirality [2] and is described by a Hamiltonian of the form

$$\mathcal{H}^{\alpha}_{\mathbf{\Pi}_\alpha}(\mathbf{k}) = v_\alpha \mathbf{k}\cdot\boldsymbol{\sigma} + m_\alpha \sigma_3 \tag{2.22}$$

respecting PH symmetry [Eq. (2.1)] with $\Xi = \sigma_1\mathcal{K}$, where $\boldsymbol{\sigma} = (\sigma_1, \sigma_2)$ is a 2D vector of Pauli matrices. Each Hamiltonian has its own (possibly distinct) positive velocity v_α (chosen to be isotropic for simplicity), and the parameters m_α control the band separations of each Dirac model. Other off-diagonal mass terms are in principle allowed by symmetry, but to streamline our discussions we choose to include these later among the allowed terms for the edge theory[3].

In working with this continuum picture, we can always envision having folded the HSPs back to $\mathbf{\Gamma}$: This is always possible through an infinitesimal perturbation that reduces translational symmetry to a symmetry under translations of two lattice vectors [150]. It may happen that such reduction of translation symmetry only occurs near the edge, but to treat the bulk and the boundary on the same footing we consider the 2D effective model as if its translation invariance had been reduced throughout. Nevertheless, the Dirac Hamiltonians inherit their properties from the conventional rotation invariants which *do* distinguish between different HSPs, relying on the underlying crystalline symmetry. (For example, for a pair of Dirac Hamiltonians describing gap closings at $\mathbf{X}$ and $\mathbf{X}'$, we could allow for deformations of v_x velocities relative to v_y such that $\mathcal{H}^{\alpha}_{\mathbf{X}}$ and $\mathcal{H}^{\alpha+1}_{\mathbf{X}'}$ are each only twofold symmetric, but are related to *each other* via a fourfold rotation.) For this reason, one may prefer to think of $\mathbf{k}$ as the (small) momentum relative to the respective HSP, even if $\mathbf{k}$ becomes the (small) absolute momentum about $\mathbf{\Gamma}$ in the folded picture.

2.3.2 Rotation Eigenvalues and Signed Representations

In this subsection we describe how the rotation eigenvalues of bulk bands pick out irreducible representations of the rotation operator r_4^α for each Dirac model in the stack. In a C_n-symmetric BZ, the HSPs may be categorised as either being mapped onto themselves (i.e., fixed) under n-fold rotation (e.g., $\mathbf{\Gamma}$ and $\mathbf{M}$ for C_4) or as being mapped to other HSPs (forming an orbit) under n-fold rotation (e.g., the twofold fixed points $\mathbf{X}$ and $\mathbf{X}'$ that map into each other under

[2] The $\mathbf{k}\cdot\boldsymbol{\sigma}$ term may always be brought to this form because the relative sign of k_1 and k_2 is altered by a basis rotation $\mathcal{H}^\alpha(\mathbf{k}) \to \sigma_1\mathcal{H}^\alpha(\mathbf{k})\sigma_1$ for which we would change the sign assigned to m_α.

[3] Allowing symmetric terms of the form $\sigma_3 \otimes M$, for example, where $M = M^T$ and $OMO^T = \bigoplus_\alpha m_\alpha$ does not change the resulting edge theory but its derivation (Appendix A.2) requires a different ansatz.

Occupied $\Pi_p^{(4)}$		r_4^α	m_α	η_α
$e^{i\pi/4}$	Γ_1, M_1	$+e^{-i\sigma_3\pi/4}$	>0	$+1$
$e^{-i\pi/4}$	Γ_4, M_4	$+e^{-i\sigma_3\pi/4}$	<0	$+1$
$e^{i3\pi/4}$	Γ_2, M_2	$-e^{-i\sigma_3\pi/4}$	<0	-1
$e^{-i3\pi/4}$	Γ_3, M_3	$-e^{-i\sigma_3\pi/4}$	>0	-1

Table 2.1 The correspondence of the rotation eigenvalue of the negative energy band to the bulk mass and rotation representation at the fourfold symmetric points $\mathbf{\Gamma}$ and $\mathbf{M}$.

fourfold rotation). We treat these two cases slightly differently. As before, we exemplify our approach on C_4-symmetric systems. We start with the 4-fold fixed points.

Rotation Invariant Momenta

Fourfold rotational symmetry of a Dirac Hamiltonian in the stack means it must satisfy

$$r_4^\alpha \mathcal{H}^\alpha_{\mathbf{\Pi}_\alpha}(\mathbf{k})\, r_4^{\alpha\dagger} = \mathcal{H}^\alpha_{\mathbf{\Pi}_\alpha}(R_4\mathbf{k}), \tag{2.23}$$

where $\mathbf{\Pi}_\alpha \in \{\mathbf{\Gamma}, \mathbf{M}\}$. Recalling that our effective Hamiltonian is written in terms of Pauli matrices, it satisfies

$$e^{-i\sigma_3\pi/4}\mathcal{H}^\alpha_{\mathbf{\Pi}_\alpha}(\mathbf{k})e^{i\sigma_3\pi/4} = \mathcal{H}^\alpha_{\mathbf{\Pi}_\alpha}(R_4\mathbf{k}). \tag{2.24}$$

This lets us identify $r_4^\alpha \propto e^{-i\sigma_3\pi/4}$ up to a complex phase. Insisting that the rotation operator commutes with the PH operator $\Xi = \sigma_1\mathcal{K}$ leaves only a freedom in the *sign* of the representation, however, so that $r_4^\alpha = \eta_\alpha e^{-i\sigma_3\pi/4}$, where $\eta_\alpha = \pm 1$. This sign, in particular sign differences between representations for different $\mathcal{H}^\alpha$, has physical consequences on the edge of the model, which we show below. (A similar approach has been used by Khalaf *et al.* [37].) These representations are referred to as "signed representations" when their sign is important [37]. Interestingly, for C_4-symmetric points, each rotation eigenvalue directly corresponds to a representation sign *and* a sign for the bulk mass term. Crucially these two parameters are not independent: As seen in Table 2.1, listing the four possibilities shown in Fig. 2.2 for the occupied rotation eigenvalues at a C_4-symmetric point gives the signed representation r_4^α *and* the sign of the mass m_α for each Dirac Hamiltonian in the stack.

Momenta Transforming into Each Other

For Dirac Hamiltonians originating from twofold fixed points such as $\mathbf{\Pi}_\alpha \in \{\mathbf{X}, \mathbf{X}'\}$ in a C_4-symmetric BZ, we instead have twofold rotational symmetry

$$r_2^\alpha \mathcal{H}^\alpha_{\mathbf{\Pi}_\alpha}(\mathbf{k}) r_2^{\alpha\dagger} = \mathcal{H}^\alpha_{\mathbf{\Pi}_\alpha}(R_2\mathbf{k}). \tag{2.25}$$

In a similar fashion to how we deduced r_4^α, we could deduce that $r_2^\alpha \propto e^{-i\sigma_3\pi/2} = -i\sigma_3$, of which two choices $r_2^\alpha = \eta_\alpha e^{-i\sigma_3\pi/2}$ with $\eta_\alpha = \pm 1$ commute with PH symmetry. (We refer to the $\eta_\alpha = -1$ case as the negatively signed representation.) One notices here, however, that specifying the occupied rotation eigenvalue does not uniquely pick out a representation sign *and* a mass sign as it did for the fourfold fixed points. This is because $\mp i\sigma_3 \to \pm i\sigma_3$ exchanges its two diagonal elements, while changing the sign of the bulk mass would change which band has negative energy; changing both at once thus leaves the occupied rotation eigenvalue unchanged. The sign of the bulk mass has implications for the edge states that appear on the boundary (specifically their direction of propagation), which will be taken into account when ensuring that we construct Dirac models describing differences between topological phases with the same Chern number [4].

As we want to know how the system (particularly the boundary) behaves under a $\pi/2$-rotation, we need to use the underlying fourfold symmetry of the system. In the original lattice model, momentum states at $\mathbf{X}+\mathbf{k}$ are mapped to $\mathbf{X}'+R_4\mathbf{k}$ under a fourfold rotation R_4 and vice versa. In terms of our stacked Dirac picture, such C_4 symmetry dictates that the Dirac Hamiltonians originating from these points be related by unitary transformations $U_{\mathbf{X}'}$, that is, $\mathcal{H}^\alpha_{\mathbf{X}}(R_4\mathbf{k}) = U_{\mathbf{X}'}\mathcal{H}^{\alpha+1}_{\mathbf{X}'}(\mathbf{k})U^\dagger_{\mathbf{X}'}$ and $\mathcal{H}^{\alpha+1}_{\mathbf{X}'}(R_4\mathbf{k}) = U_{\mathbf{X}}\mathcal{H}^\alpha_{\mathbf{X}}(\mathbf{k})U^\dagger_{\mathbf{X}}$. Here, we chose to place the Dirac Hamiltonians for $\mathbf{X}$ and $\mathbf{X}'$ in neighbouring sub-blocks α and $\alpha+1$, respectively. In terms of the resulting 4×4 Hamiltonian,

$$\mathcal{H}^\oplus(\mathbf{k}) \equiv \mathcal{H}^\alpha_{\mathbf{X}}(\mathbf{k}) \oplus \mathcal{H}^{\alpha+1}_{\mathbf{X}'}(\mathbf{k}), \tag{2.26}$$

the only form of this fourfold symmetry compatible with our convention [Eq. (2.22)] of momenta and Pauli matrices appearing in $k_j\sigma_j$ combinations and having positive velocities is

$$\mathcal{H}^\oplus(R_4\mathbf{k}) = \left[e^{-i\sigma_3\pi/4}\mathcal{H}^{\alpha+1}_{\mathbf{X}'}(\mathbf{k})e^{i\sigma_3\pi/4}\right] \oplus \left[e^{-i\sigma_3\pi/4}\mathcal{H}^\alpha_{\mathbf{X}}(\mathbf{k})e^{i\sigma_3\pi/4}\right], \tag{2.27}$$

[4] That the sign of the mass at $\mathbf{X}^{(\prime)}$ is not set by the occupied rotation eigenvalues is also one source of the "surface-state ambiguity" tabulated in Ref. [37], which is where the surface signature of a nontrivial bulk is not uniquely determined from the symmetry indicators. Once we specify that $\Delta\mathrm{Ch} = 0$ (using information beyond symmetry indicators alone), there will be no ambiguity in the surface-state of this system.

Occupied $\Pi_p^{(2)}$		m_α	$r_4^\oplus$	η_α
$e^{i\pi/2}$	X_1	>0	$e^{-i\sigma_3\pi/4}\otimes\tau_1$	$+1$
$e^{-i\pi/2}$	X_2	<0	$e^{-i\sigma_3\pi/4}\otimes\tau_1$	$+1$
$e^{i\pi/2}$	X_1	<0	$e^{-i\sigma_3\pi/4}\otimes i\tau_2$	-1
$e^{-i\pi/2}$	X_2	>0	$e^{-i\sigma_3\pi/4}\otimes i\tau_2$	-1

Table 2.2 The correspondence of the rotation eigenvalue of the negative energy band and bulk mass to the rotation representation for the $\mathbf{X}/\mathbf{X}'$ points. Also shown is the sign of the twofold rotation representation defined as $r_2^\alpha = \eta_\alpha e^{-i\sigma_3\pi/2}$.

which also holds if velocities are anisotropic at $\mathbf{X}$ and $\mathbf{X}'$ in a C_4 related manner. The unitary relation between $\mathcal{H}_{\mathbf{X}}^{\alpha}(R_4\mathbf{k})$ and $\mathcal{H}_{\mathbf{X}'}^{\alpha+1}(\mathbf{k})$ together with our convention of identical Dirac Hamiltonian chiralities also implies $m_\alpha = m_{\alpha+1}$. The symmetry relation (2.27) can be compactly expressed as

$$\mathcal{H}^\oplus(R_4\mathbf{k}) = r_4^\oplus \mathcal{H}^\oplus(\mathbf{k})\, r_4^{\oplus\dagger}, \tag{2.28}$$

where the requirement of PH symmetry $[r_4^\oplus, \Xi\oplus\Xi] = 0$ leaves two choices

$$r_4^\oplus = e^{-i\sigma_3\pi/4}\otimes\tau_1 \quad \text{or} \quad r_4^\oplus = e^{-i\sigma_3\pi/4}\otimes i\tau_2, \tag{2.29}$$

apart from an overall sign that will later be seen to be inconsequential. Here, we denote the space of stacked Dirac Hamiltonians $\alpha, \alpha+1$ by τ_μ.

Squaring these two representations gives $(r_4^\oplus)^2 = +e^{-i\sigma_3\pi/2}\otimes\mathbb{I}_2$ or $(r_4^\oplus)^2 = -e^{-i\sigma_3\pi/2}\otimes\mathbb{I}_2$, respectively, which is consistent with the two signed options for r_2 above and implies $\eta_\alpha = \eta_{\alpha+1}$. Unlike for the truly fourfold fixed points, the representation and sign of $m_\alpha = m_{\alpha+1}$ is not uniquely determined from occupied rotation eigenvalue—instead the correspondence is between the combination of occupied rotation eigenvalue and mass to rotation representation, shown in Table 2.2.

2.3.3 Dirac Stacks for Topological Interfaces

We now outline how a stacked Dirac model can be constructed to describe a transition of between C_n-symmetric superconductors with different topological invariants. As stated above, the stacked Dirac models capture *differences* between topological phases. Consider two regions $\mathcal{I}$ and $\mathcal{O}$ with BdG Hamiltonians $\mathcal{H}_\mathcal{I}(\mathbf{k})$ and $\mathcal{H}_\mathcal{O}(\mathbf{k})$, respectively, understood as being the regions inside ($\mathcal{I}$) and outside ($\mathcal{O}$) our system of interest. Each system has

independent occupancies $\#\Pi_p^{(n)}$, meaning that we can define differences in occupancies:

$$\Delta\#\Pi_p^{(n)} \equiv \#\Pi_p^{(n)}|_{\mathcal{I}} - \#\Pi_p^{(n)}|_{\mathcal{O}}. \tag{2.30}$$

For a meaningful description in terms of stacked Dirac models, we require the rotation operators in both regions $\mathcal{O}$ and $\mathcal{I}$ to be the same. This is always possible through the addition of trivial bands to either region, which can safely be added since they do not change the topological invariants. Once the rotation operator is the same in both systems, each must have the same total number of each rotation eigenvalue, so $\#\Pi_p^{(n)}|_{\mathcal{I}} + \bar{\#}\Pi_p^{(n)}|_{\mathcal{I}} = \#\Pi_p^{(n)}|_{\mathcal{O}} + \bar{\#}\Pi_p^{(n)}|_{\mathcal{O}}$, where $\bar{\#}$ counts unoccupied states. Using PH symmetry which relates occupied and unoccupied states, we see that these differences are not all independent [cf. Eq. (2.5)]:

$$\Delta\#\Pi_p^{(n)} = -\Delta\#\Pi_{n-p+1}^{(n)}. \tag{2.31}$$

For example, in a C_4-symmetric system one has ten occupancies ($\Gamma_{1,2,3,4}$, $M_{1,2,3,4}$ and $X_{1,2} = X'_{1,2}$) to consider, which are in this way reduced to five independent differences, chosen as $\Delta\#X_1$, $\Delta\#\Gamma_1$, $\Delta\#\Gamma_2$, $\Delta\#M_1$ and $\Delta\#M_2$.

For each independent difference $\Delta\#\Pi_p^{(n)}$, one adds $|\Delta\#\Pi_p^{(n)}|$ Dirac Hamiltonians to the stack with the appropriate rotation representations and masses. Closing and reopening every gap by taking $m_\alpha \to -m_\alpha$ for all α then reproduces the transition $\mathcal{H}_{\mathcal{I}}(\mathbf{k}) \to \mathcal{H}_{\mathcal{O}}(\mathbf{k})$.

We now address the feature of Dirac Hamiltonians deriving from $\mathbf{X}/\mathbf{X}'$, demonstrated in Table 2.2, which is that the occupation of either eigenvalues $X_1 = i$ or $X_2 = -i$ does not uniquely determine the sign of the bulk mass nor the rotation representation. Thus, a given change $\Delta\#X_1$ may be realised through stacks of two different types of Dirac Hamiltonians. Looking at Table 2.2, these two types can be distinguished by the sign η_α of the twofold rotation operator $r_2^\alpha = \eta_\alpha e^{-i\sigma_3\pi/2}$. Let $\Delta\#X_1^\pm$ denote the contributions to $\Delta\#X_1$ from Hamiltonians with $\eta_\alpha = \pm 1$, such that the overall change in occupation is $\Delta\#X_1 = \Delta\#X_1^+ + \Delta\#X_1^-$. Note that this decomposition is specific to the construction of a Dirac model, rather than a direct property of the original Bloch Hamiltonians $\mathcal{H}_{\mathcal{I}}(\mathbf{k})$ and $\mathcal{H}_{\mathcal{O}}(\mathbf{k})$. Distinguishing between $\Delta\#X_1^\pm$, as we now explain, allows us to construct a Dirac stack that does not change the Chern number when $m_\alpha \to -m_\alpha$, as we require for the anomalous boundary states we wish to investigate.

Zero change in the Chern number implies that there should be an equal number of left- and right-moving modes at the $\mathcal{I} - \mathcal{O}$ interface. This is equivalent to the statement that there should be an equal number of Dirac Hamiltonians in the stack with positive and negative bulk masses (since we consider the scenario where all m_α change sign across the $\mathcal{I} - \mathcal{O}$ boundary). From Table 2.1, it is evident that these bulk masses are uniquely determined from changes in

occupied rotation eigenvalues, which is not the case for Dirac Hamiltonians derived from gap closings at $\mathbf{X}/\mathbf{X}'$. Looking again at Table 2.2, and recalling that all the Dirac Hamiltonians have the same chirality, we see that for the same $\Delta\#X_1^+$ and $\Delta\#X_1^-$ the contribution to $\Delta\mathrm{Ch}$ is opposite because, for a given $\Pi_p^{(2)}$ being occupied, opposite signs of η_α imply opposite signs for m_α. Combining all these observations, we may rewrite the $\Delta\mathrm{Ch} = 0$ condition as

$$\begin{aligned} 0 &= \Delta\mathrm{Ch} && (2.32)\\ &= 2\Delta\#X_1^- - 2\Delta\#X_1^+ - \Delta\#\Gamma_1 - \Delta\#M_1 + \Delta\#\Gamma_2 + \Delta\#M_2 && (2.33)\\ &= -4\Delta\#X_1^+ + 2\Delta[X] - \Delta[M_1] + \Delta[M_2], && (2.34) \end{aligned}$$

Taken on their own, changes in rotation invariants $[M_1]$, $[M_2]$ and $[X]$ of Eq. (2.6) determine $\Delta\mathrm{Ch} \mod 4$ [123, 56], but with a specific stacked Dirac model realisation we could equate $\Delta\mathrm{Ch} = 0$ exactly. (The modulo 4 ambiguity reappears if one does not have access to the $\Delta\#X_1^\pm$ extra information because changing $\Delta\#X_1^+ \to \Delta\#X_1^+ + 1$ and $\Delta\#X_1^- \to \Delta\#X_1^- - 1$ would not affect $\Delta[X]$ but would change $\Delta\mathrm{Ch} \to \Delta\mathrm{Ch} - 4$.)

2.3.4 Effective Edge Theory

We are interested in what happens at the boundary between systems in different topological classes, which in our continuum model above occurs when the masses $\{m_\alpha\}$ change sign. Each bulk gap closing has an associated chiral edge mode localised at the boundary [31, 126]. Its effective edge theory, allowing also for smooth (on the scale of the lattice spacing) variations in the local boundary direction, can be derived as described in Appendix A.2.1. The resulting stack of decoupled left- and right-moving chiral edge modes is described by the edge Hamiltonian

$$h_{\mathbf{r},\mathbf{k}_\parallel} = h^{\rightarrow}_{\mathbf{r},\mathbf{k}_\parallel} \oplus h^{\leftarrow}_{\mathbf{r},\mathbf{k}_\parallel}, \quad \text{with} \quad h^{s}_{\mathbf{r},\mathbf{k}_\parallel} = \bigoplus_{\alpha} h^{\alpha s}_{\mathbf{r},\mathbf{k}_\parallel}, \tag{2.35}$$

where $s \in \{\rightarrow, \leftarrow\}$ such that right- and left-moving modes

$$h^{\alpha\rightarrow}_{\mathbf{r},\mathbf{k}_\parallel} = +v_\alpha k_\parallel \quad \text{and} \quad h^{\alpha\leftarrow}_{\mathbf{r},\mathbf{k}_\parallel} = -v_\alpha k_\parallel \tag{2.36}$$

have been placed in different sub-blocks [5]. The subscript $\parallel$ denotes a projection onto the direction $\hat{\mathbf{n}}_\parallel$ along the edge (i.e., $k_\parallel = \mathbf{k}\cdot\hat{\mathbf{n}}_\parallel$) and the subscript $\mathbf{r}$, indicating the position along the boundary, is present to allow for the aforementioned smooth boundary variations.

[5] This 2×2 block-diagonal structure is possible by choosing the original stacking order in Eq. (2.21) to be such that Dirac Hamiltonians with $m_\alpha < 0$ in the bulk appear first.

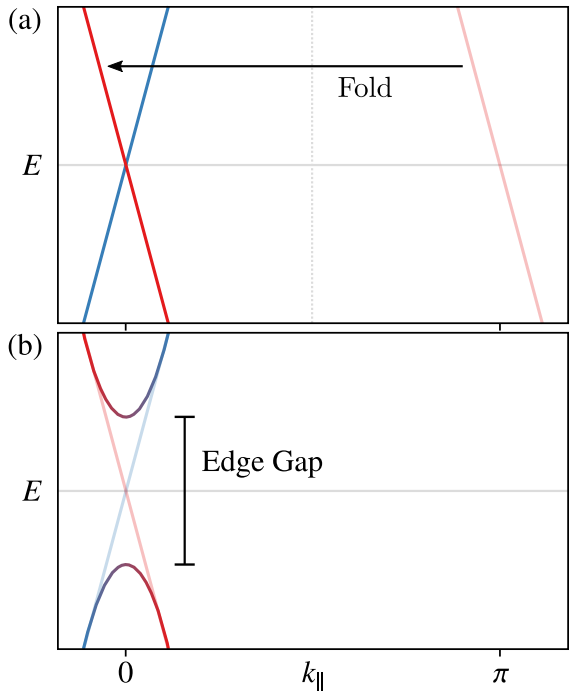

Fig. 2.4 Example spectrum along the edge of a 2D superconductor. Each sign change of a bulk mass m_α manifests itself as a chiral mode on the edge. (a) The folding process which takes all HSPs to $\mathbf{\Gamma}$, meaning that all edge modes are centred on $k_\parallel = 0$ in the continuum description. (b) An edge mass term that couples a left-mover to a right-mover, opening up a gap on the edge.

Having limited ourselves to $\Delta\mathrm{Ch} = 0$ transitions, there are as many left-movers as right-movers in the stack. Since gap closings happening at $\mathbf{X}$ must also happen at $\mathbf{X}'$ by rotational symmetry, the corresponding edge modes appear in pairs on the boundary with the same propagation direction (because their bulk masses and chiralities are the same). We show an example spectrum for the edge Hamiltonian in Fig. 2.4(a).

The edge Hamiltonian also possesses a PH symmetry that follows from the original PH symmetry of the bulk. With a particular basis choice for the edge Hamiltonian (detailed in Appendix A.2.3), the PH operator is simply complex conjugation $\mathcal{K}$ and the symmetry is given by

$$h_{\mathbf{r},\mathbf{k}_\parallel} = -\mathcal{K}\, h_{\mathbf{r},-\mathbf{k}_\parallel}\, \mathcal{K}. \tag{2.37}$$

Edge Projections of Rotation Representations

We now describe how the sign of the bulk rotation representation is transmitted to the representations on the edge, while also recalling the fact that the rotation operator used to classify periodic Hamiltonians may be different to the rotation operator compatible with the

$r^{\alpha}_{4,\mathbf{0}}$	$r^{\alpha}_{4,(\mathbf{a}_1+\mathbf{a}_2)/2}$	
	$\mathbf{\Pi}_\alpha = \mathbf{\Gamma}$	$\mathbf{\Pi}_\alpha = \mathbf{M}$
$+e^{-i\sigma_3\pi/4}$	$+e^{-i\sigma_3\pi/4}$	$-e^{-i\sigma_3\pi/4}$
$-e^{-i\sigma_3\pi/4}$	$-e^{-i\sigma_3\pi/4}$	$+e^{-i\sigma_3\pi/4}$

Table 2.3 The correspondence from $r^{\alpha}_{4} \equiv r^{\alpha}_{4,\mathbf{0}}$ to the shifted rotation operator at the fourfold fixed points. The representation changes sign at $\mathbf{M}$ but is unchanged at $\mathbf{\Gamma}$.

$r^{\oplus}_{4,\mathbf{0}}$	$r^{\oplus}_{4,(\mathbf{a}_1+\mathbf{a}_2)/2}$
$e^{-i\sigma_3\pi/4}\otimes i\tau_2$	$e^{-i\sigma_3\pi/4}\otimes \tau_1$
$e^{-i\sigma_3\pi/4}\otimes \tau_1$	$e^{-i\sigma_3\pi/4}\otimes i\tau_2$

Table 2.4 The correspondence from $r^{\oplus}_{4} \equiv r^{\oplus}_{4,\mathbf{0}}$ to the shifted rotation operator. These rotation representations only occur at $\mathbf{X}/\mathbf{X}'$ points.

boundary. As shown in Sec. 2.2, these operators are related in terms of the location $\mathbf{c}$ of the rotation centre within a unit cell as

$$r^{\alpha}_{n,\mathbf{c}} = \exp\left\{[i\mathbf{\Pi}_\alpha \cdot (1 - R_n^{-1})\mathbf{c}]\right\} r^{\alpha}_{n}. \tag{2.38}$$

For C_4 symmetry, this is shown explicitly in Tables 2.3 and 2.4.

It is from this operator that the rotation operator of the edge theory must be derived $r^{\alpha}_{n,\mathbf{c}} \to u^{\alpha}_{n,\mathbf{c}}$. The rotational symmetry for the edge Hamiltonian is then expressed through

$$h_{R_n\mathbf{r},R_n\mathbf{k}_\parallel} = u_{n,\mathbf{c}}\, h_{\mathbf{r},\mathbf{k}_\parallel}\, u^{T}_{n,\mathbf{c}}, \tag{2.39}$$

where $u_{n,\mathbf{c}} = \bigoplus_\alpha u^{\alpha}_{n,\mathbf{c}}$ is the direct sum of all the edge-projected rotation representations, and $u_{n,\mathbf{c}}$ consists only of real elements due to PH symmetry being simply complex conjugation.

For C_4-symmetric systems, $u_{4,\mathbf{c}}$ is block-diagonal with 1×1 blocks for edge modes deriving from gap closings at $\mathbf{\Gamma}$ or $\mathbf{M}$, and 2×2 blocks to transform between $\mathbf{X}$- and $\mathbf{X}'$-deriving edge modes. These are derived explicitly for C_4 in Appendix A.2.2 and summarised in Table 2.5.

2.3.5 Boundary Mass Terms

In general, counterpropagating modes on the edges become gapped due to symmetry-allowed terms that couple these modes. Such gapping terms (or *mass* terms) $\mu_{\mathbf{r}}$ couple left-moving to right-moving modes, appearing as off-diagonal terms in the (previously gapless) edge

$\mathbf{\Pi}_\alpha$	$r^\alpha_{4,\mathbf{c}}$	$\eta_{\alpha,\mathbf{c}}$	$u^\alpha_{4,\mathbf{c}}$	$\det u^\alpha_{4,\mathbf{c}}$
$\mathbf{\Gamma}$, $\mathbf{M}$	$+e^{-i\sigma_3\pi/4}$	$+1$	$+1$	$+1$
	$-e^{-i\sigma_3\pi/4}$	-1	-1	-1
$\mathbf{X}/\mathbf{X}'$	$e^{-i\sigma_3\pi/4}\otimes i\tau_2$	-1	$i\tau_2$	$+1$
	$e^{-i\sigma_3\pi/4}\otimes \tau_1$	$+1$	τ_1	-1

Table 2.5 The edge rotation representations $u^\alpha_{4,\mathbf{c}}$ resulting from the bulk representation $r^\alpha_{4,\mathbf{c}}$ at $\mathbf{\Gamma}$, $\mathbf{M}$, and $r^\oplus_{4,\mathbf{c}}$ at $\mathbf{X}$, $\mathbf{X}'$. The signs of these representations are denoted by $\eta_{\alpha,\mathbf{c}}$, where $\eta_{\alpha,\mathbf{0}} \equiv \eta_\alpha$.

Hamiltonian

$$h_{\mathbf{r},\mathbf{k}_\parallel} = \begin{pmatrix} h^{\rightarrow}_{\mathbf{r},\mathbf{k}_\parallel} + i\lambda^{\rightarrow}_{\mathbf{r}} & i\mu_{\mathbf{r}} \\ -i\mu^T_{\mathbf{r}} & h^{\leftarrow}_{\mathbf{r},\mathbf{k}_\parallel} + i\lambda^{\leftarrow}_{\mathbf{r}} \end{pmatrix}, \tag{2.40}$$

where we also included the (skew-symmetric) forward scattering matrices $\lambda^s_{\mathbf{r}}$ with $s \in \{\rightarrow, \leftarrow\}$. (These terms are 'forward scattering' in the sense that they scatter between modes moving in the same direction.) Because of PH symmetry, $\mu_{\mathbf{r}}$ and $\lambda^s_{\mathbf{r}}$ must be real. To see why $\mu_{\mathbf{r}}$ can be interpreted as mass terms, it is illuminating to consider a simplified case where all $2p$ edge modes have the same velocity $v_\alpha = 1$ and to ignore all forward-scattering terms, giving the edge Hamiltonian

$$h^0_{\mathbf{r},\mathbf{k}_\parallel} = \begin{pmatrix} k_\parallel \mathbb{I}_p & i\mu_{\mathbf{r}} \\ -i\mu^T_{\mathbf{r}} & -k_\parallel \mathbb{I}_p \end{pmatrix}. \tag{2.41}$$

Because $\mu_{\mathbf{r}}$ is a real matrix, it may be decomposed via a singular value decomposition (SVD) into $\mu_{\mathbf{r}} = YDW^T$ where Y and W are orthogonal matrices and $D = \mathrm{diag}(\Delta_1, \Delta_2, \ldots, \Delta_p)$ is a diagonal matrix. Using the SVD, the edge Hamiltonian can be factorised as

$$h^0_{\mathbf{r},\mathbf{k}_\parallel} = \begin{pmatrix} Y & 0 \\ 0 & W \end{pmatrix} \begin{pmatrix} k_\parallel \mathbb{I}_p & iD \\ -iD & -k_\parallel \mathbb{I}_p \end{pmatrix} \begin{pmatrix} Y^T & 0 \\ 0 & W^T \end{pmatrix}, \tag{2.42}$$

i.e., it is unitarily equivalent to p stacked one-dimensional massive Dirac Hamiltonians. Each band separation is set by Δ_α and the energy eigenvalues are $E^2_\alpha = k^2_\parallel + \Delta^2_\alpha$. In an SVD, the matrices Y and W are typically chosen such that all $\Delta_\alpha \geq 0$. Here, we fix $\det Y = \det W = 1$ by multiplying an appropriate number of rows of Y (and W) by minus one, that is, an odd number of rows when initially $\det Y = -1$ ($\det W = -1$), and an even number of rows when initially $\det Y = +1$ ($\det W = +1$). Keeping $h^0_{\mathbf{r},\mathbf{k}_\parallel}$ the same then requires changing the signs of the corresponding Δ_α accordingly, such that $\mathrm{sgn}\det D = \prod_\alpha \mathrm{sgn}\,\Delta_\alpha = \pm 1$, where the minus sign arises when the number of sign changes in Y and W add up to an odd number.

When rotating from one edge to the neighbouring one using Eq. (2.39), the matrix $\mu_{\mathbf{r}}$ transforms as $\mu_{\mathbf{r}} \to \mu_{R\mathbf{r}}$. A Δ_α changing sign under this transformation expresses that there is a Δ_α mass kink in the edge Dirac theory as we turn from one edge to the neighbouring one. Such a mass kink binds a Majorana state [151]; it gives rise to a corner Majorana mode in the system. Considering all Δ_α, therefore, a sign change of $\det D$ along a corner results in an odd number of Majorana bound states, i.e., a single Majorana after the hybridisation of pairs. Since $\det Y = \det W = 1$, the determinant of D changing sign is captured by a relative sign between $\operatorname{sgn}\det \mu_{\mathbf{r}}$ and $\operatorname{sgn}\det \mu_{R\mathbf{r}}$.

While this observation is illuminating, it relies on all edge modes dispersing in the same way and the absence of forward-scattering terms. The next subsection will use a more robust characterisation in terms of Pfaffians that works even in this more general scenario.

Topologically Distinct Boundary Phases

Having seen how back-scattering terms on the edge can be interpreted as mass terms in a one-dimensional theory, we now reframe this in terms of a topological invariant for Class D systems in 1D—the Pfaffian invariant, familiar from Sec. 1.1.3. More precisely, this invariant is the product of Pfaffians at the HSPs in the BZ [25, 29], where the Hamiltonian is skew-symmetric. The continuum theory we use only captures changes of the topological invariant along a corner, but not any invariant itself. Such a change in the topological invariant manifests in a sign change of the Pfaffian at $k_\parallel = 0$, a point where the Hamiltonian is skew-symmetric (guaranteed by PH symmetry, $h_{\mathbf{r},\mathbf{k}_\parallel=\mathbf{0}} = -h^*_{\mathbf{r},\mathbf{k}_\parallel=\mathbf{0}}$). Considering the Pfaffian at $k_\parallel = 0$ (but not at $k_\parallel = \pi$) is sufficient because having folded the HSPs (see Fig. 2.4) all edge mass kinks involve edge gap closings in the proximity of $k_\parallel = 0$. Of these only the gap closings *at* $k_\parallel = 0$ are of importance: While forward scattering may cause some of the gap closings to split away symmetrically from $k_\parallel = 0$, we need not account for these because they only result in *pairs* of bound states which can hybridise and gap out. More explicitly, we define $A_{\mathbf{r}} \equiv -ih_{\mathbf{r},\mathbf{k}_\parallel=\mathbf{0}}$, which is a real and skew-symmetric matrix, and the indicator $\delta_{\mathbf{r}}$ using which we shall track changes in the edge invariant [29]

$$\delta_{\mathbf{r}} = \operatorname{sgn}\operatorname{Pf} A_{\mathbf{r}} = \operatorname{sgn}\left[(-i)^p \operatorname{Pf} h_{\mathbf{r},\mathbf{k}_\parallel=\mathbf{0}}\right]. \tag{2.43}$$

We can also verify that this gives the same result as our simplified example $h^0_{\mathbf{r},\mathbf{k}_\parallel=\mathbf{0}}$ introduced above. The Pfaffian of $A^0_{\mathbf{r}} = -ih^0_{\mathbf{r},\mathbf{k}_\parallel=\mathbf{0}}$ equals

$$\mathrm{Pf}\left(A^0_{\mathbf{r}}\right) = \det\begin{pmatrix} Y & 0 \\ 0 & W \end{pmatrix} \mathrm{Pf}\begin{pmatrix} 0 & D \\ -D & 0 \end{pmatrix} = \mathrm{Pf}\begin{pmatrix} 0 & D \\ -D & 0 \end{pmatrix} \tag{2.44}$$

$$= (-1)^{p(p-1)/2} \det D, \tag{2.45}$$

where we used that $\det Y = \det W = 1$. As the matrix dimension p does not change around a corner, sign changes in $\mathrm{Pf}\left(A^0_{\mathbf{r}}\right)$ thus capture sign changes in $\det D$. We emphasize, however, that Eq. (2.43) goes beyond the counting argument for $h^0_{\mathbf{r},\mathbf{k}_\parallel=\mathbf{0}}$, as it also takes into account forward-scattering terms and allows different velocities v_α.

2.4 Bulk Rotation Invariants and Corner Majoranas

The bulk rotational symmetry has direct implications for the Pfaffian invariant $\delta_{\mathbf{r}}$ that distinguishes topological phases along the edge. Using the rotational symmetry relation of Eq. (2.39), which also holds for $A_{\mathbf{r}}$, we use a Pfaffian identity to assess the difference in topology for neighbouring edges as follows:

$$\begin{aligned} \delta_{R_n\mathbf{r}} &= \mathrm{sgn}\,\mathrm{Pf}(A_{R_n\mathbf{r}}) = \mathrm{sgn}\,\mathrm{Pf}(u_{n,\mathbf{c}} A_{\mathbf{r}} u^T_{n,\mathbf{c}}) = \mathrm{sgn}\,\mathrm{Pf}(A_{\mathbf{r}}) \det u_{n,\mathbf{c}} \\ &= \delta_{\mathbf{r}} \det u_{n,\mathbf{c}}, \end{aligned} \tag{2.46}$$

where we used that $\det u_{n,\mathbf{c}} = \pm 1$ since $u_{n,\mathbf{c}}$ is orthogonal. Thus, the Pfaffian invariants for edges related by R_n are the same only if $\det u_{n,\mathbf{c}} = +1$.

For $\det u_{n,\mathbf{c}} = -1$, neighbouring edges are topologically distinct and consequently must harbor an odd number of Majorana states bound between them. The topological index $\Upsilon^{(n)}_{\mathbf{c}} = 0, 1$ equal to the number (modulo 2) of Majorana zero modes localised between neighbouring edges is therefore [6]

$$(-1)^{\Upsilon^{(n)}_{\mathbf{c}}} = \det u_{n,\mathbf{c}}. \tag{2.47}$$

[6] $\det u_{n,\mathbf{c}} = +1$ corresponding to the case without boundary Majorana bound states is also consistent with the fact that if $\det u_{n,\mathbf{c}} = +1$, then for a circular boundary the transformation $h_{\mathbf{r},\mathbf{k}} \to h_{R_n\mathbf{r},R_n\mathbf{k}}$ could be achieved via many infinitesimal orthogonal transformations (connected to the identity). There would therefore exist a continuous deformation between the two Hamiltonians that does not close any gaps and respects all the symmetries, thereby making them topologically equivalent.

Note that the sign of $\det u_{n,\mathbf{c}} = \prod_\alpha \det u^\alpha_{n,\mathbf{c}}$ flips with each addition onto the stack of a representation with $\det u^\alpha_{n,\mathbf{c}} = -1$. It is also reassuring that had we (arbitrarily) chosen the basis states of the edge Hamiltonian to transform trivially under the *negative* representation instead (amounting to redefining $u^\alpha_{n,\mathbf{c}} \to -u^\alpha_{n,\mathbf{c}}$), then this index would be unchanged since $\det u_{n,\mathbf{c}} \to (-1)^{2p} \det u_{n,\mathbf{c}} = \det u_{n,\mathbf{c}}$.

Another way to derive higher-order surface signatures for topological crystalline phases [37, 46, 129, 152] is the construction of a minimal set of mutually anticommuting mass matrices $\Omega \equiv \{\Omega_i\}$ (with $\{\Omega_i, \Omega_j\} = 2\delta_{ij}$) that also anticommute with a (simplified) model surface Hamiltonian. These mass terms are added to the surface in a symmetry-respecting manner, where the transformation properties of Ω_i under crystalline symmetry operations dictate the possible existence of gapless regions on the boundary. The presence of anomalous surface states is predicted from the cardinality of Ω. However, such an approach is not immediately applicable to our edge Hamiltonian Eq. (2.40) because $\mu_\mathbf{r}$ is a generic mass term that may not be constructed from Ω as $\mu_\mathbf{r} = \sum_i \epsilon^i_\mathbf{r} \Omega_i$ everywhere along the boundary[7]. Our edge Hamiltonian may also contain forward scattering terms $\lambda^s_\mathbf{r}$ that do not follow this prescription. An advantage of our Pfaffian invariant approach is therefore that it swiftly demonstrates the relation between boundary Majoranas and rotation representations, without any special algebraic structure in the boundary Hamiltonian beyond that required by PH symmetry.

2.4.1 Path Independence

It should be pointed out that because the original classification [56] is in terms of a stable (i.e., robust under the addition of trivial bands) equivalence, many different stacked Dirac models can realise the same change in topological phase. Conversely, it means that every phase change can be realised through many 'paths' of gap closings in a phase diagram; for example a change in phase $\Delta(\mathrm{Ch}, [X], [M_1], [M_2]) = (0, 0, 1, 1)$ could be realised through $\Delta(\#\Gamma_1, \#\Gamma_2) = (-1, -1)$ or through $\Delta(\#M_1, \#M_2) = (1, 1)$. For the $\det u_{n,\mathbf{c}}$ index to be truly topological, it must be independent of the path of gap closings chosen to go from one phase to another. We demonstrate that this is so focusing on the C_4-symmetric case below.

In our C_4-symmetric Dirac construction, multiple possible paths arise because there are six independent parameters for gap closings [namely $\Delta(\#X_1^-, \#X_1^+, \#\Gamma_1, \#\Gamma_2, \#M_1, \#M_2)$] but only four constraints in the form of the four topological invariants $\Delta(\mathrm{Ch}, [X], [M_1], [M_2])$, leaving two degrees of freedom. Because of the additive structure of the invariants, these two degrees of freedom define a plane in the space of $\Delta(\#X_1^-, \#X_1^+, \#\Gamma_1, \#\Gamma_2, \#M_1, \#M_2)$. This

[7] Furthermore, a set Ω will not always be closed under rotation $\Omega_i \to u_{n,\mathbf{c}} \Omega_i u^T_{n,\mathbf{c}} \notin \Omega$ when all the Dirac Hamiltonians in the stack are allowed to be different.

plane can be spanned by two gap closing patterns which do not change the phase, namely $\Delta(\#X_1^-, \#\Gamma_1, \#M_1) = (1,1,1)$ and $\Delta(\#X_1^-, \#\Gamma_2, \#M_2) = (-1,1,1)$. The first set of of occupation number changes is consistent with adding a trivial Dirac (sub)stack with $\Gamma_p^{(4)} = e^{i\pi/4}$, and the second with adding a trivial Dirac stack with $\Gamma_p^{(4)} = e^{3i\pi/4}$, where both additions are to the inside ($\mathcal{I}$) region, with their PH conjugates appearing outside ($\mathcal{O}$). One may verify that the Dirac (sub)stacks implementing these changes in occupation number have $\det u_{4,\mathbf{c}} = +1$, both for $\mathbf{c} = \mathbf{0}$ and $\mathbf{c} = (\mathbf{a}_1 + \mathbf{a}_2)/2$. This means that each plane in the parameter space has a definite value of $\det u_{4,\mathbf{c}}$.

We now explain why trivial bands cannot change $\det u_{4,\mathbf{c}}$. In our Dirac model, adding PH conjugate pairs of trivial bands to $\mathcal{I}$ and $\mathcal{O}$ correspond to Dirac (sub)stacks that upon $m_\alpha \to -m_\alpha$ leave topological invariants unchanged. Consider the minimal stack involving Dirac Hamiltonians $\mathcal{H}^1_{\mathbf{\Gamma}}$, $\mathcal{H}^2_{\mathbf{M}}$, and $\mathcal{H}^\oplus = \mathcal{H}^3_{\mathbf{X}} \oplus \mathcal{H}^4_{\mathbf{X}'}$, at $\mathbf{\Gamma}$ and $\mathbf{M}$ and $\mathbf{X}/\mathbf{X}'$ respectively. Requiring $\Delta[M_i] = \Delta[X] = 0$ sets $M_p = \Gamma_p$ and $X_p = (\Gamma_p)^2$. (In this paragraph we understand $\Pi_p^{(4)}$ to mean the *occupied* eigenvalue of this minimal stack.) The value of Γ_p sets the sign of m_1 and η_1, and consequently $\operatorname{sgn} m_2 = \operatorname{sgn} m_1$ and $\eta_2 = \eta_1$ (see Tables 2.1 and 2.3). Ensuring $\Delta\mathrm{Ch} = 0$ then requires us to choose a mass at $\mathbf{X}/\mathbf{X}'$ ($m_3 = m_4$) with opposite sign to $m_{1,2}$. Together with $X_p = (\Gamma_p)^2$ this singles out a specific η_3 (Tables 2.2 and 2.4). (Recall from Table 2.5 that the signs η_α are associated with a specific $\det u^\alpha_{4,\mathbf{0}}$.) Crucially, no matter what the value of Γ_p is we always find $\det u^1_{4,\mathbf{c}} \det u^2_{4,\mathbf{c}} \det u^3_{4,\mathbf{c}} = 1$, both for $\mathbf{c} = \mathbf{0}$ and $\mathbf{c} = (\mathbf{a}_1 + \mathbf{a}_2)/2$. Specifically: for $\mathbf{c} = \mathbf{0}$, $\det u^1_{4,\mathbf{0}} \det u^2_{4,\mathbf{0}} = 1$ and $\det u^3_{4,\mathbf{0}} = 1$ (Tables 2.1 and 2.3); and for $\mathbf{c} = (\mathbf{a}_1 + \mathbf{a}_2)/2$, both $\det u^2_{4,(\mathbf{a}_1+\mathbf{a}_2)/2}$ and $\det u^3_{4,(\mathbf{a}_1+\mathbf{a}_2)/2}$ change sign (Tables 2.2 and 2.4) while $\det u^1_{4,(\mathbf{a}_1+\mathbf{a}_2)/2}$ stays unchanged.

The corner mode index is therefore independent of the exact sequence of gap closings leading to a particular topological phase.

2.4.2 Constructing Topological Index for Corner States

Having thus established the path independence, and thus the topological nature of our $\det u_{n,\mathbf{c}}$ index, we must be able to express it in terms of the bulk topological invariants. As seen from Table 2.5, only certain bulk rotation representations $\{r^\alpha_{4,\mathbf{c}}, r^\oplus_{4,\mathbf{c}}\}$ lead to edge rotation representations with $\det u^\alpha_{4,\mathbf{c}} = -1$. In turn, these $\{r^\alpha_{4,\mathbf{c}}, r^\oplus_{4,\mathbf{c}}\}$ are characteristic of changes in the occupation number of certain rotation eigenvalues. Thus, by tracking changes in occupation of a subset of rotation eigenvalues, one may deduce the number of edge modes with $\det u^\alpha_{n,\mathbf{c}} = -1$, giving us $\det u_{n,\mathbf{c}}$. We expect a $\mathbb{Z}_2$-valued index $\Upsilon^{(n)}_{\mathbf{c}}$ defined, as in Eq. (2.47), by $(-1)^{\Upsilon^{(n)}_{\mathbf{c}}} \equiv \det u_{n,\mathbf{c}}$, where $\Upsilon^{(n)}_{\mathbf{c}}$ counts the number of Majorana modes between neighbouring edges.

We now describe how such a relation is obtained in C_4-symmetric systems. The central idea is to track how the changes $\Delta(\#X_1^-, \#X_1^+, \#\Gamma_1, \#\Gamma_2, \#M_1, \#M_2)$ influence $\det u_{n,\mathbf{c}}$. We start with the case of the rotation centre being at $\mathbf{c} = \mathbf{0}$. Consider the fourfold fixed point $\mathbf{\Gamma}$: We see from Tables 2.1 and 2.5 that for a change in occupation $\Delta\#\Gamma_2$, there will be $|\Delta\#\Gamma_2|$ Dirac Hamiltonians added to the stack that have $\det u^\alpha_{4,\mathbf{0}} = -1$. On the other hand, the $|\Delta\#\Gamma_1|$ other Dirac Hamiltonians at $\mathbf{\Gamma}$ have $\det u^\alpha_{4,\mathbf{0}} = 1$ so need not be counted. Similarly, we should also count $|\Delta\#M_2|$ but not $|\Delta\#M_1|$. As for the Dirac Hamiltonian pair at the $\mathbf{X}/\mathbf{X}'$ points, Tables 2.2 and 2.5 show that we should count $|\Delta\#X_1^+|$ because $\det u^\alpha_{4,\mathbf{0}} = -\eta_\alpha$ for these Dirac Hamiltonians.

Thus, recalling that $\det u_{4,\mathbf{c}} = \prod_\alpha \det u^\alpha_{4,\mathbf{c}}$, the index for $\mathbf{c} = \mathbf{0}$ is

$$\Upsilon^{(4)}_{\mathbf{0}} = \Delta\#\Gamma_2 + \Delta\#M_2 + \Delta\#X_1^+ \mod 2, \tag{2.48}$$

where due to the modulo 2 we could drop the absolute value symbols. When $\mathbf{c} = \frac{1}{2}(\mathbf{a}_1 + \mathbf{a}_2)$, however, one can see from Tables 2.3 and 2.4 that representations at $\mathbf{M}$ and $\mathbf{X}, \mathbf{X}'$ acquire a minus sign, so that by analogous arguments

$$\Upsilon^{(4)}_{(\mathbf{a}_1+\mathbf{a}_2)/2} = \Delta\#\Gamma_2 + \Delta\#M_1 + \Delta\#X_1^- \mod 2. \tag{2.49}$$

This shifted index and the original are related through

$$\begin{aligned}\Upsilon^{(4)}_{(\mathbf{a}_1+\mathbf{a}_2)/2} &= \Upsilon^{(4)}_{\mathbf{0}} + \Delta\#M_1 + \Delta\#M_2 + \Delta\#X_1 \mod 2 &(2.50)\\ &= \Upsilon^{(4)}_{\mathbf{0}} + \Delta[M_1] + \Delta[M_2] + \Delta[X] \mod 2. &(2.51)\end{aligned}$$

The rotation centre thus only influences the existence of Majoranas on the edge if $\Delta\nu = \Delta[M_1] + \Delta[M_2] + \Delta[X] \mod 2 \neq 0$. Recognizing that ν is precisely the weak topological invariant in C_4-symmetric systems [56], Eq. (2.51) can be seen to express the combined effect of the weak invariant and the rotation centre announced in the Introduction. It remains to rewrite $\Upsilon^{(4)}_{\mathbf{0}}$ purely in terms of rotation invariants, which is possible using $\Delta\mathrm{Ch} = 0$ derived earlier. Substituting $\Delta\#X_1^+$ from Eq. (2.34), and using that $\Upsilon^{(4)}_{\mathbf{0}} = \Delta[M_2] + \Delta\#X_1^+ \mod 2$ we get

$$\Upsilon^{(4)}_{\mathbf{0}} = \frac{1}{4}\left(\Delta[M_1] + 3\Delta[M_2] - 2\Delta[X]\right) \mod 2. \tag{2.52}$$

Summarizing the bulk-boundary correspondence in one equation, we have

$$\Upsilon^{(4)}_{\mathbf{c}} = \frac{1}{4}\left(\Delta[M_1] + 3\Delta[M_2] - 2\Delta[X]\right) + \frac{1}{2\pi}\Delta\mathbf{G}_\nu \cdot \mathbf{c} \mod 2, \tag{2.53}$$

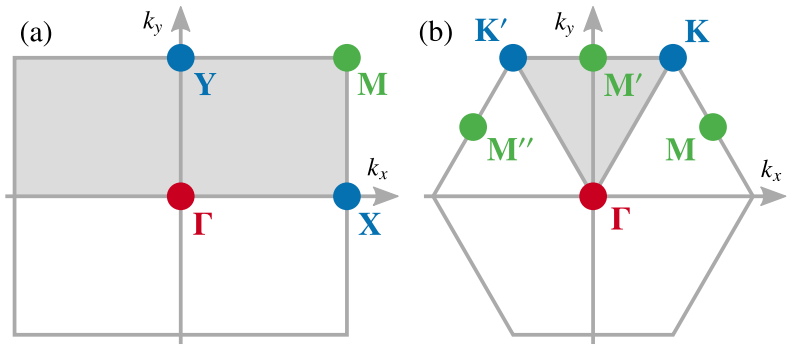

Fig. 2.5 (a) Brillouin zone for C_2-symmetric models. All HSPs are twofold fixed points, i.e., they map to themselves under a C_2 rotation. (b) Brillouin zone for C_6-symmetric models. Only $\mathbf{\Gamma}$ is a sixfold fixed point, whereas the threefold fixed point $\mathbf{K}$ and $\mathbf{K}'$ map to each other under a sixfold rotation. The twofold fixed points $\mathbf{M}$, $\mathbf{M}'$, and $\mathbf{M}''$ form an orbit $\mathbf{M} \to \mathbf{M}' \to \mathbf{M}''$ under sixfold rotation.

where $\Delta\mathbf{G}_\nu = \Delta\nu(\mathbf{b}_1 + \mathbf{b}_2)$ is the weak index vector (in terms of reciprocal lattice vectors $\mathbf{b}_i$ satisfying $\mathbf{a}_i \cdot \mathbf{b}_j = 2\pi\delta_{ij}$). This index between rotation invariants and boundary Majorana bound states is one of the central predictions of our stacked Dirac approach.

Although the intermediate steps made use of 'extra' information $\Delta\#X_1^+$ specific to the stacked Dirac model construction, the physical conclusion depends only on the topological invariants. The way that similar indices have been derived before is to find example systems with corner modes (corner charge) and appeal to the linearity of indices in terms of the invariants [121, 56, 71] to reconstruct their form. In contrast, here we have shown how any continuum description consistent with a given change of bulk topological invariants of rotationally symmetric topological superconductors encodes transformation properties of adjacent edge Hamiltonians and thus the topological index for corner Majorana modes.

2.5 Other Rotational Symmetries

We now briefly outline how our construction is applied to different rotational symmetries, namely for C_2- and C_6-symmetric systems. The C_2-symmetric BZ contains only twofold fixed points, and so is contained within the C_4 construction, but the C_6 BZ contains threefold and sixfold fixed points that are not contained in the C_4 case and require some further discussion.

2.5.1 Twofold Symmetry

The C_2 case is simpler in some respects than the C_4 case because all the HSPs are twofold fixed points and so we keep this discussion brief. The $\Delta\mathrm{Ch} = 0$ condition is now:

$$\begin{aligned} 0 = \Delta\mathrm{Ch} = {} & \Delta\#X_1^+ - \Delta\#X_1^- + \Delta\#Y_1^+ - \Delta\#Y_1^- \\ & + \Delta\#M_1^+ - \Delta\#M_1^- + \Delta\#\Gamma_1^+ - \Delta\#\Gamma_1^-, \end{aligned} \tag{2.54}$$

where we again split contributions according to η_α, the sign of the twofold rotation operators r_2^α. This can be rewritten in terms of the C_2 rotation invariants (now $[X] = \#X_1 - \#\Gamma_1$, $[Y] = \#Y_1 - \#\Gamma_1$ and $[M] = \#M_1 - \#\Gamma_1$):

$$\begin{aligned} 0 = {} & -\Delta[X] + \Delta[Y] + \Delta[M] - 4\Delta\#\Gamma_1 \\ & + 2(\Delta\#X_1^- + \Delta\#Y_1^- + \Delta\#M_1^- + \Delta\#\Gamma_1^-), \end{aligned} \tag{2.55}$$

which reproduces the Ch $\mod 2$ relation of Ref. [56]. Counting the parity of negative representations, we have

$$\Upsilon_{\mathbf{0}}^{(2)} = \Delta\#X_1^- + \Delta\#Y_1^- + \Delta\#M_1^- + \Delta\#\Gamma_1^- \mod 2, \tag{2.56}$$

which we may combine with Eq. (2.55) to write

$$\Upsilon_{\mathbf{0}}^{(2)} = \frac{1}{2}(\Delta[X] + \Delta[Y] + \Delta[M]) \mod 2 \tag{2.57}$$

when the physical rotation centre is at the centre of the unit cell ($\mathbf{c} = \mathbf{0}$). In C_2-symmetric systems, there are more choices for $\mathbf{c}$ than with C_4 symmetry: both $\mathbf{c} = \mathbf{a}_1/2$ and $\mathbf{c} = \mathbf{a}_2/2$ in addition to $\mathbf{c} = (\mathbf{a}_1 + \mathbf{a}_2)/2$. The C_2 case also has two independent weak invariants $\nu_1 = [X] + [M] \mod 2$ and $\nu_2 = [Y] + [M] \mod 2$, combined into the weak invariant vector $\Delta\mathbf{G}_\nu = \Delta\nu_1\mathbf{b}_1 + \Delta\nu_2\mathbf{b}_2$. Again, the indices for systems with different rotation centres are found to be related through

$$\Upsilon_{\mathbf{c}}^{(2)} = \Upsilon_{\mathbf{0}}^{(2)} + \frac{1}{2\pi}\Delta\mathbf{G}_\nu \cdot \mathbf{c} \mod 2. \tag{2.58}$$

To arrive at Eq. (2.58), we used Eq. (2.20) with $R_2^T = -1$ which shows that now the sign of the representation can change at $\mathbf{X}$, $\mathbf{Y}$, and $\mathbf{M}$ depending on $\mathbf{G}_\nu$ and $\mathbf{c}$. For example, when considering $\mathbf{c} = \mathbf{a}_1/2$, one starts by counting

$$\Upsilon_{\mathbf{a}_1/2}^{(2)} = \Delta\#X_1^+ + \Delta\#Y_1^- + \Delta\#M_1^+ + \Delta\Gamma_1^- \mod 2, \tag{2.59}$$

consistent with the above.

2.5.2 Sixfold Symmetry

The BZ of a C_6-symmetric system has three different sets of high-symmetry points: One sixfold fixed point at $\mathbf{\Gamma}$, two threefold fixed points at $\mathbf{K}$ and $\mathbf{K}'$, and three twofold fixed points at $\mathbf{M}$, $\mathbf{M}'$ and $\mathbf{M}''$; cf. Fig. 2.5(b). Within a C_6-symmetric lattice, there is only one centre of sixfold rotation at $\mathbf{c} = \mathbf{0}$ so it need not be specified. The bulk is characterised by the Chern number and the two rotational invariants [56]

$$[M] = \#M_1 - (\#\Gamma_1 + \#\Gamma_3 + \#\Gamma_5) \tag{2.60}$$

$$[K] = \#K_1 - (\#\Gamma_1 + \#\Gamma_4). \tag{2.61}$$

Any gap closing away from $\mathbf{\Gamma}$ can be implemented analogously to the previously established description of stacked Dirac models at $\mathbf{X}/\mathbf{X}'$; cf. Sec. 2.3.2. Gap closings at $\mathbf{K}/\mathbf{K}'$ require a stack of two Dirac Hamiltonians, and gap closings at $\mathbf{M}/\mathbf{M}'/\mathbf{M}''$ require a stack of three Dirac Hamiltonians.

We must proceed slightly differently with gap closings at $\mathbf{\Gamma}$, however. While a simple Dirac Hamiltonian [Eq. (2.22)] is sufficient to describe gap closings that change $\#\Gamma_1$ or $\#\Gamma_3$ (and accordingly $\#\Gamma_6$ or $\#\Gamma_4$), a 2×2 Hamiltonian describing changes to $\#\Gamma_2$ (and hence $\#\Gamma_5$) with rotation representation $r_6^\alpha = \pm i\sigma_3$ requires cubic momentum terms [150]:

$$\mathcal{H}_{\mathbf{\Gamma}}^{\alpha}(\mathbf{k}) = (v_\alpha k)^3(\cos(3\theta)\sigma_1 + \sin(3\theta)\sigma_2) + m_\alpha\sigma_3. \tag{2.62}$$

Deriving an edge theory in the same way as in Sec. A.2.1 is impeded by the presence of these non-linear terms, although we can conclude from the Chern number that a transition $m_\alpha \to -m_\alpha$ would harbor three gapless modes.

Our strategy will instead be to add trivial bands such that the transition for the whole system has $\Delta\#\Gamma_5 = 0$, which can be modelled with only linear Dirac Hamiltonians. Specifically, a trivial band with sixfold eigenvalue $\Gamma_5 = -i$ has threefold eigenvalue $(\Gamma_5)^2 = (\Gamma_5^*)^2 = -1 = K_2$ and twofold eigenvalue $(\Gamma_5)^3 = i = M_1$. Thus, there exists a trivial superconductor that, when transitioning to its PH-conjugate, changes $\Delta\#\Gamma_5 = 1$ and $\Delta\#M_1 = 1$ [and $\Delta\#K_2 = 0$ in accordance with Eq. (2.31)]. Adding multiples of this trivial superconductor allows us to trade a description involving Eq. (2.62) at $\mathbf{\Gamma}$ for one with three Dirac models at $\mathbf{M}/\mathbf{M}'/\mathbf{M}''$.

By associating the masses and rotation representations of Dirac Hamiltonians with occupied rotation eigenvalues as in the main text, we find

$$\begin{aligned} 0 = \Delta\mathrm{Ch} = &-\Delta\#\Gamma_1 + \Delta\#\Gamma_3 + 3\Delta\#\Gamma_5^+ - 3\Delta\#\Gamma_5^- \\ &- 2\Delta\#K_1 + 3\Delta\#M_1^- - 3\Delta\#M_1^+, \end{aligned} \tag{2.63}$$

consistent with the Ch mod 6 relation for the invariants in Ref [56]. The need to split contributions according to η_α again originates from $i\sigma_3$ being a traceless representation (see Sections 2.3.2 and 2.3.3).

Counting negative representations and considering $\Delta\#\Gamma_5 = 0$, the index is

$$\Upsilon_{\mathbf{0}}^{(6)} = \Delta\#K_1 + \Delta\#\Gamma_3 + \Delta\#M_1^- \mod 2, \tag{2.64}$$

where $|\Delta\#K_1|$ is counted because $r_6^\oplus = e^{-i\sigma_3\pi/6} \otimes \tau_1$ is the only rotation representation for Dirac Hamiltonians at $\mathbf{K}/\mathbf{K}'$, which becomes $u_6^\oplus = \tau_1$ on the edge. Gap closings at $\mathbf{M}/\mathbf{M}'/\mathbf{M}''$ permit rotation representations

$$r_6^\oplus = \pm e^{-i\sigma_3\pi/6} \otimes \begin{pmatrix} 0 & 0 & 1 \\ 1 & 0 & 0 \\ 0 & 1 & 0 \end{pmatrix}, \tag{2.65}$$

which have $\det u_6^\oplus = \pm 1$ and hence $|\Delta\#M_1^-|$ is also counted. Upon substitution of Eq. (2.63) for $\Delta\#K_1$, the index is simply

$$\Upsilon_{\mathbf{0}}^{(6)} = \frac{1}{2}\Delta[M] \mod 2. \tag{2.66}$$

We have thus derived the second-order bulk-boundary correspondence for the C_6-symmetric case using our stacked Dirac framework. This index coincides with the index for Majoranas bound to disclinations in a C_6-symmetric crystal [56].

2.5.3 Other Rotation Representations for the Superconducting Order Parameter

When determining the rotation operator of the BdG Hamiltonian from the symmetry of the underlying crystal, one must also consider the symmetry of the superconducting order parameter. A BCS pairing term $\hat{\Delta} + \hat{\Delta}^\dagger$ is different to the normal-state part of the Hamiltonian because it need only be invariant *up to a gauge transformation* under the act of rotation $\hat{R}_n$, so that $\hat{R}_n \hat{\Delta} \hat{R}_n^{-1} = e^{i\Theta_n}\hat{\Delta}$ [50]. In the first-quantised picture, the off-diagonal pairing term $\Delta(\mathbf{k}) = -\Delta^T(-\mathbf{k})$ transforms under rotation as [52]

$$\mathcal{R}(\mathbf{k})\Delta(\mathbf{k})\mathcal{R}^T(-\mathbf{k}) = e^{i\Theta_n}\Delta(R_n\mathbf{k}), \tag{2.67}$$

where the action of rotation on momentum space operators

$$\hat{R}_n \hat{c}^\dagger_\alpha(\mathbf{k}) \hat{R}_n^{-1} = \hat{c}^\dagger_\beta(R_n\mathbf{k})\mathcal{R}_{\beta\alpha}(\mathbf{k}) \tag{2.68}$$

was derived in Sec. 2.2.1. The symmetry of the pairing is therefore defined by a one-dimensional rotation representation $e^{i\Theta_n}$ where $\Theta_n = 2\pi\ell_n/n$ and $\ell_n \in \mathbb{Z}_n$, arising from the angular momentum of Cooper pairs. The rotation operator for the BdG Hamiltonian should therefore be

$$r_n(\mathbf{k}) = \begin{pmatrix} \mathcal{R}(\mathbf{k}) & \\ & e^{i\Theta_n}\mathcal{R}^*(-\mathbf{k}) \end{pmatrix} \tag{2.69}$$

to reproduce the symmetry relation Eq. (2.13). (The "rotation" operator $r_n(\mathbf{k})$ is now the composition of physical rotation with a gauge transformation $U = e^{i\Theta_n/2}e^{-i\Theta_n\sigma_3/2}$ [50].) This implies that the algebraic relation between PH and rotation operators is [52]

$$\Xi r_n(\mathbf{k})\Xi^{-1} = e^{-i\Theta_n} r_n(-\mathbf{k}), \tag{2.70}$$

which is different to the $\ell_n = 0$ relation that reduced to commutation at HSPs. We now discuss the consequences of $\ell_n \neq 0$ for the bulk-boundary correspondence.

One can always define an alternative operator $\tilde{r}_n(\mathbf{k}) = e^{-i\Theta_n/2} r_n(\mathbf{k})$ that commutes with PH symmetry at HSPs:

$$\Xi \tilde{r}_n(\mathbf{k})\Xi^{-1} = \tilde{r}_n(-\mathbf{k}). \tag{2.71}$$

When ℓ_n is even, $\tilde{r}_n(\mathbf{k})$ is a spinful operator satisfying $\tilde{r}_n^n = -\mathbb{1}$ for which we can use our stacked Dirac model construction to derive a valid corner mode index in terms of the eigenvalues of $\tilde{r}_n(\mathbf{k})$. This may be translated to an index in terms of the eigenvalues of $r_n(\mathbf{k})$ by recalling the labeling convention in Eq (2.3), which gives an equivalence

$$\Pi_p^{(n)} \iff \tilde{\Pi}^{(n)}_{p-\ell_n/2} \tag{2.72}$$

between the eigenvalues of a state under both operators. Thus the case of even ℓ_n is qualitatively identical to the $\ell_n = 0$ case.

When ℓ_n is odd, however, it has been argued by Geier *et al.* [49] that the boundary classification does not permit a second-order (nor weak) phase. This qualitative difference arises because $\tilde{r}_n(\mathbf{k})$ now behaves like a spinless operator satisfying $\tilde{r}_n^n = +\mathbb{1}$. The real eigenvalues of $\tilde{r}_n(\mathbf{k})$ are mapped onto themselves under PH symmetry, rather forming complex conjugate pairs (as in Figure 2.2), leading to a different bulk classification.

2.6 Examples

The numerics for this section were performed by Jan Behrends.

We illustrate our approach using a lattice model. Consider a generalisation of two models introduced by Benalcazar *et al.* that are realised on a square lattice with primitive lattice vectors $\mathbf{a}_1 = a\hat{\mathbf{x}}$, $\mathbf{a}_2 = a\hat{\mathbf{y}}$ [56]. The combinations $\mathbf{a}_1' = \mathbf{a}_1 + \mathbf{a}_2$ and $\mathbf{a}_2' = -\mathbf{a}_1 + \mathbf{a}_2$ connect next-nearest-neighbour sites. The BdG Hamiltonian

$$H(\mathbf{k}) = \begin{pmatrix} f_1(\mathbf{k})\sigma_3 + g_1(\mathbf{k})\sigma_2 & m(\sigma_3 - i\sigma_0) \\ m(\sigma_3 + i\sigma_0) & f_2(\mathbf{k})\sigma_3 + g_2(\mathbf{k})\sigma_2 \end{pmatrix} \tag{2.73}$$

with the onsite coupling m and the two functions

$$f_i(\mathbf{k}) = \cos\phi\cos(\mathbf{k}\cdot\mathbf{a}_i) + \sin\phi\cos\left(\mathbf{k}\cdot\mathbf{a}_i'\right) \tag{2.74}$$

$$g_i(\mathbf{k}) = \cos\phi\sin(\mathbf{k}\cdot\mathbf{a}_i) + \sin\phi\sin\left(\mathbf{k}\cdot\mathbf{a}_i'\right) \tag{2.75}$$

describes a C_4-symmetric superconductor with PH symmetry $\Xi = \sigma_1\mathcal{K}$ and fourfold rotation

$$r_4 = \begin{pmatrix} & -i\sigma_3 \\ \sigma_0 & \end{pmatrix} \tag{2.76}$$

where $r_4^4 = -\mathbb{1}$. (All units of energy are absorbed into the Hamiltonian.) As discussed in Sec. 2.2, each gapped phase is characterised by a set four invariants, which we show in the phase diagram in Fig. 2.6. Changing the parameters $\phi \to \phi + \pi$ and $m \to -m$ results in $H \to -H$ hence in Fig. 2.6 we consider only positive m values. For $|m| > 1$, the onsite coupling dominates and the Hamiltonian is trivial, independently of the parameter ϕ.

Two regimes are relevant for our classification: phase I around $(\phi, m) = (0, 0)$ and phase II around $(\phi, m) = (\pi/2, 0)$. Phase I is characterised by $\Upsilon^{(4)}_{\mathbf{0}} = 1$ and $\Upsilon^{(4)}_{(\mathbf{a}_1+\mathbf{a}_2)/2} = 0$, thus, it only supports corner modes when the physical rotation centre is in the centre of a unit cell (cf. Sec. 2.2.1 and Appendix A.1 for our notion of the unit cell). To couple counterpropagating chiral edge modes, we add a density-wave-type boundary perturbation that respects rotation invariance but has periodicity of two unit cells. Specifically, on each edge we couple every second pair of lattice sites via a nearest-neighbour hopping term $it\hat{c}_j^\dagger\tau_3\hat{c}_{j+1}$ (where τ_i acts on the outer degree of freedom) to break translation invariance and open a gap. (In Fig. 2.8 we show the boundary perturbation together with the $m = \phi = 0$ limit of the bulk system.) We show the energy eigenvalues for square lattices with $L \times L$ sites in Fig. 2.7(a). When L is odd, the rotation centre is in the centre of a unit cell, when L is even, it is at its corner. Corner modes therefore only arise when L is odd. Phase II, however, is characterised by

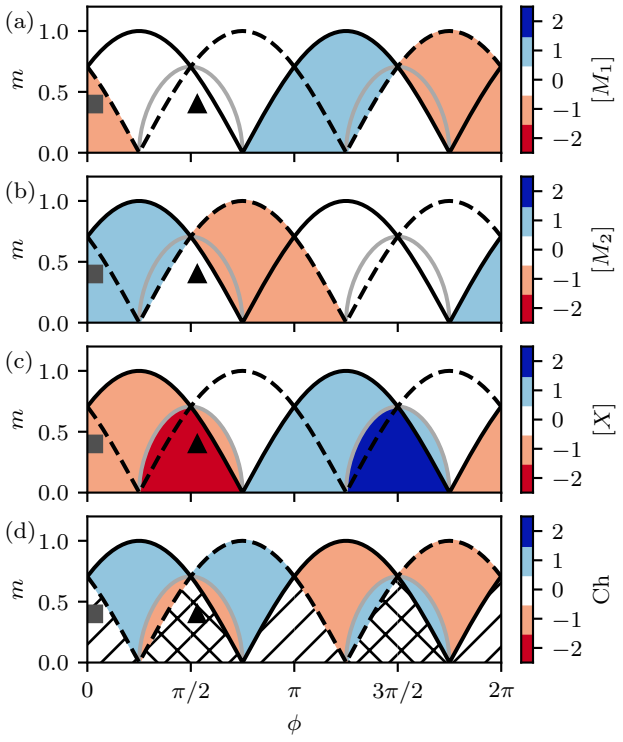

Fig. 2.6 Phase diagram for the lattice Hamiltonian Eq. (2.73). The black lines denote gap closings at $\mathbf{\Gamma}$, the black dashed lines at $\mathbf{M}$ and the gray lines at $\mathbf{X}, \mathbf{X}'$. In panel (d), the black stripes in phases with Ch = 0 denote values of the topological index predicting corner modes. Diagonal stripes $\Upsilon^{(4)}_{\mathbf{0}} = 1$ and $\Upsilon^{(4)}_{(\mathbf{a}_1+\mathbf{a}_2)/2} = 0$, and a crossed pattern $\Upsilon^{(4)}_{\mathbf{0}} = \Upsilon^{(4)}_{(\mathbf{a}_1+\mathbf{a}_2)/2} = 1$. The gray square and black triangles mark the parameters used in Fig. 2.7(a) and (b), respectively.

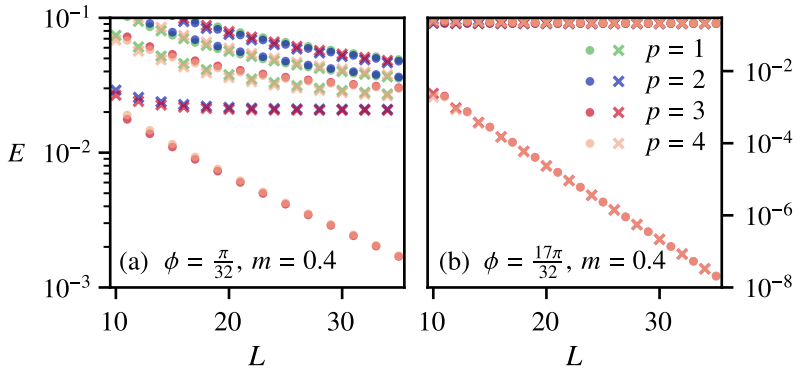

Fig. 2.7 Energy eigenvalues of the Hamiltonian defined in Eq. (2.73) with a boundary perturbation (with $t = 0.025$) for a finite square lattice with $L \times L$ sites. The different colours denote the rotation eigenvalue $e^{i\pi/4(2p-1)}$ and the different symbols distinguish different rotation centres (crosses and circles corresponding to even and odd L, respectively). In panel (a), we show an example of phase I with $\phi = \pi/32$ and $m = 0.4$. The system only supports gapless corner modes for odd L, which corresponds to a physical rotation centre in the centre of a unit cell. In panel (b), we show an example of phase II with $\phi = 17\pi/32$ and $m = 0.4$. The corner modes remain for both rotation centres, i.e., both even and odd L. We choose the logarithmic scale of the y axis to visualise the exponential decrease in energy.

$\Upsilon^{(4)}_{\mathbf{0}} = \Upsilon^{(4)}_{(\mathbf{a}_1+\mathbf{a}_2)/2} = 1$, meaning that the presence of corner modes does not depend on the position of the rotation centre, as we show in Fig. 2.7(b).

In phase II, the surface gap closes when $m = 0$. Then, the corner modes delocalise along the edge and their energy in any finite system increases accordingly. When tuning the parameters of the Hamiltonian to cross $m = 0$, the localisation length of the corner modes first increases when approaching $m = 0$ and then decreases again with increasing surface gap size. Thus, the presence of corner modes solely depends on bulk properties. Corner modes may at most delocalise for fine-tuned points in parameter space, but they cannot be removed by attempting a surface-only topological phase transition via a surface gap closing.

Using the above phases, more phases can be constructed by stacking different copies of this model. For example, stacking phases I and II results in hybridisation of the corner modes, such that $\Upsilon^{(4)}_{\mathbf{0}} = 0$ and $\Upsilon^{(4)}_{(\mathbf{a}_1+\mathbf{a}_2)/2} = 1$, i.e., only systems with the physical rotation centre at the corners of the unit cell support corner modes. Stacking the four primitive models introduced in Ref. [56] enables us to construct models that realise all possible combinations of the bulk invariants.

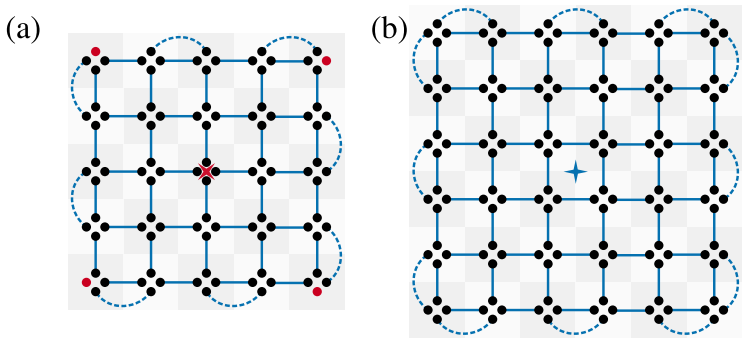

Fig. 2.8 Lattice model that demonstrates the importance of the rotation centre. The Hamiltonian (2.73) at $\phi = m = 0$ only contains terms, illustrated by the solid blue lines, that couple neighbouring Majorana modes, illustrated by the black circles; cf. Ref. [56]. In this case, Majorana modes at the edge are completely decoupled from the bulk and do not contribute to the Hamiltonian, i.e., all edge modes have zero energy. This degeneracy can be lifted by a density wave [56] modelled by coupling every second nearest-neighbour site on the edge (dashed blue lines). (a) When the rotation centre is in the centre of a unit cell, any coupling that respects rotational invariance is bound to leave Majoranas at the corners uncoupled (red circles). This completely decoupled case is topologically equivalent to any case with a finite localisation length of the corner modes, as for example considered in Fig. 2.7. (b) However, when the rotation centre is at the corner of a unit cell, it is possible to open a surface gap without Majorana bound states.

2.7 Conclusion

In this Chapter, we formulated a second-order bulk-boundary correspondence for C_n-symmetric 2D crystalline superconductors: We related the bulk topological invariants of Ref. [56] to a topological index $\Upsilon_{\mathbf{c}}^{(n)}$ accounting for the presence of Majorana corner states in systems with C_n-symmetry-respecting boundaries. The exact form of the corner index depends on the interplay of the weak invariants and the location of the physical rotation centre with respect to the unit cell. In particular, certain systems only support corner modes when the rotation centre is in the centre of a unit cell, while other systems require it to be at the unit cell boundary. (These statements have no unit-cell-choice ambiguity: For a well-defined bulk-boundary correspondence we must use unit-cell choices described in Sec. 2.2 and Appendix A.1.) Our approach to identify the corner index is based on stacked Dirac Hamiltonians. It is thus extendable to other crystal symmetries, as long as they can be represented for a minimal model of stacked Dirac Hamiltonians.

The index we find is consistent with previous classification schemes in rotationally symmetric superconductors. For example, Teo and Hughes found an invariant for Majorana modes trapped at lattice defects that strongly resembles the indices given in Eqs. (2.52) and (2.53) [121, 56]. When predicting trapped Majorana modes, the Burgers vector of a

lattice defect only matters when the weak invariant is nonzero, similar to the fact that $\Upsilon^{(n)}_{\mathbf{c=0}}$ and $\Upsilon^{(n)}_{\mathbf{c\neq 0}}$ may only be different if the weak invariant is nonzero.

Invoking a counting argument, Ref. [121] noted that the invariants constructed for lattice defects can also be used to predict corner modes in finite systems. Our work elucidates why this is so from an entirely different viewpoint: We established how bulk invariants relate to the transformation properties of adjacent edge Hamiltonians, the latter having become the unifying perspective for constructing various examples of higher-order topological phases [46, 37, 129].

We illustrated our results using lattice models. In particular, we showed that the physical rotation centre in finite systems may indeed give rise to different corner mode configurations. Furthermore, we explicitly demonstrated that the bulk-boundary correspondence is robust against gap closings at the boundary, i.e., that the presence of corner modes is purely determined by bulk quantities that relate different edges to another. In all lattice model examples, we identified corner modes using the scaling of the energies: For finite 2D square samples of size $L \times L$, the energy of the second-order bound states decays exponentially with L.

The latter scaling observation may be particularly helpful for future studies considering hybrid higher-order topology [131], expected to arise in our systems when we allow for nonzero Chern number. In such cases, the quantised energy levels of the delocalised chiral edge modes are expected to show a $1/L$ decay with increasing L, in sharp contrast with the exponential decay of the second-order bound state energies.

Chapter 3

Quantum tunnelling in the presence of a topology-changing fermionic bath

3.1 Motivation

In the previous Chapter, our concern was the gapless states that formed at the interface between topologically distinct (crystalline) superconductors. Here, we are interested in an effect purely attributed to the bulk gap closing between topological phases. This is inherent to any topological phase transition, regardless of the nature of any associated gapless boundary states, so we expect qualitative results from this Chapter to be applicable to any symmetry class. This effect has to do with quantum tunnelling.

Quantum tunnelling of a particle can be significantly altered in the presence of a bath. At zero temperature, a gapless bath reduces the tunnelling amplitude by a factor that is exponentially small in the system-to-bath coupling and the tunnelling potential width [153, 154]. For gapped baths, however, the exponent decreases with the ratio of the bath's gap and the oscillation frequency characterizing the minima of the tunnelling potential [155–157], and so the bath can be neglected for large gaps. This feature is crucial for the coherence of Josephson-junction-based superconducting qubits [158, 159, 157, 160, 108], where the position of the tunnelling "particle" is the superconducting phase difference ϕ; in these systems the gapped fermionic bath of electrons merely renormalises the junction's capacitance [161, 162].

In-gap fermionic levels change this picture [161, 163]: For example, an approximate [164, 165] or symmetry-enforced [25, 166, 113, 167, 168, 163] crossing of in-gap levels along the tunnelling path acts to suppress quantum tunnelling. In this Chapter, we consider a more dramatic scenario: What happens if the bath is gapped at the minima of the tunnelling

potential, but undergoes a *bulk gap closing* (i.e., merging of level continua, instead of a single level crossing) when the particle tunnels between the minima?

Such gap closings can be enforced by topology: When the bath Hamiltonian depends on the particle coordinate such that potential minima correspond to gapped bath Hamiltonians but with different minima corresponding to different values of a suitable Hamiltonian topological invariant [12, 127, 169, 170], then the robustness of this invariant under deformations that do not close the bulk gap implies that the bath must undergo a bulk gap closing somewhere along the tunnelling path. This scenario is different from previous works on gauge theories with topologically distinct vacua [171, 172, 109, 110]: there, topology is that of gauge field configurations, i.e., of instantons, while for us the crucial form topology is fermionic, in the sense of topological insulators and superconductors [12, 127, 169].

Instantons, however, also enter the scenario we aim to study, as they provide a general field theoretical framework for tunnelling amplitudes [109, 110]. In this field theoretical language, the problem we are interested in corresponds to, as we shall explain, instantons linking the topology change of a d-dimensional bath to protected gapless modes in interfaces between topologically distinct phases in $d+1$ dimensions.

The question we set to answer is inspired by theoretical [100, 101] and experimental [102, 103] work on planar Josephson junctions, motivating the $d = 1$ example that we shall be mostly focusing on. In these setups, the fermionic topology changes as a function of the superconducting phase difference ϕ across the junction [100, 101], resulting in two topologically inequivalent minima of the effective Josephson potential. The concept we investigate is however more general and can arise in other settings where the control parameter for whether a fermionic system is in a topological phase can be promoted into a quantum variable.

In the language of planar Josephson junctions, the new ingredient we add is charging energy, a contribution to the Hamiltonian to be considered, e.g., in Cooper pair box systems [173] that we reviewed in Sec. 1.2.1. Charging energy serves as a kinetic term for ϕ, hence it is its presence that enables ϕ to quantum tunnel between the minima of the effective Josephson potential it experiences.

Our main finding is that the topology-enforced gap closing reduces the tunnelling amplitude exponentially in the size of the bath (which for our planar-junction inspired model is also the system size). We derive, and quantify, this result using instantons, a method which we employ both analytically in illuminating limits, and in variational numerics in more general cases. We find that our variational approach, although focused on a certain instanton ansatz, performs excellently, as confirmed by comparisons with the ground state energy splitting obtained by exact diagonalisation.

The rest of the Chapter is organised as follows: After introducing our $d = 1$ model in Sec. 3.2, we describe the field theory for the general problem in Sec. 3.3. We then link instantons coupled to d-dimensional fermions to topological boundary modes of systems in $d+1$ dimensions in Sec. 3.4, a section which also includes a detailed analytical study of our $d = 1$ model, focusing on the "sharp-instanton limit" to illuminate key topological features. We describe our variational approach in Sec. 3.5 and compare our instanton-based results with exact diagonalisation in Sec. 3.5.4. We summarise our results and discuss some implications and generalisations in Sec. 3.6.

3.2 Model

Our model is inspired by proposals that implement a nontrivial topological superconductor in planar Josephson junctions [101, 100]. In these quasi-one-dimensional systems at the interface between two superconductors, the phase difference ϕ between the superconductors drives a transition between topologically trivial and nontrivial regimes, with the latter hosting zero-energy Majorana end modes. Importantly, the ground state energy forms a potential landscape with two topologically inequivalent minima [100]. This behaviour is captured by the effective Hamiltonian

$$\mathcal{H}_\phi(k) = \Delta\cos^2\left(\frac{\phi}{2}\right)\sigma_3 - \Delta\sin^2\left(\frac{\phi}{2}\right)\left[\cos(k)\sigma_3 + \sin(k)\sigma_2\right], \tag{3.1}$$

which is topologically trivial around $\phi = 0$ and nontrivial [25] around $\phi = \pi$, with transitions occurring at $\phi = \pi/2, 3\pi/2$. It interpolates between the two dimerised limits of the Kitaev chain at $\phi = 0$ and $\phi = \pi$, where Majoranas are coupled either only on the same site or only between neighbouring sites, respectively [25]. The Pauli matrices σ_μ act in particle-hole (PH) space and $\mathcal{H}_\phi$ respects both PH (with $\Xi = \sigma_1\mathcal{K}$, where $\mathcal{K}$ is complex conjugation) and time-reversal symmetry (with $T = \mathcal{K}$). The first term proportional to $\cos^2(\phi/2)$ is a chemical potential, whose value we chose to match the superconducting order parameter Δ. The single-particle energies $\varepsilon^\pm_\phi(k) = \pm\Delta\sqrt{1-\sin^2(\phi)\cos^2(k/2)}$ equal $\pm\Delta$ at both $\phi = 0$ and $\phi = \pi$.

We show the single-particle and ground state energies $V_\phi = \frac{1}{2}\sum_k \varepsilon^-_\phi(k)$ for different boundary conditions in Fig. 3.1. For periodic boundary conditions (PBC), the ground state parity changes a function of ϕ, whereas for antiperiodic boundary conditions (APBC) the ground state remains in the same parity sector. With open boundary conditions (OBC), Majorana zero modes form at the ends of the chain in the topological phase such that the ground state becomes approximately degenerate (with exponentially small splitting that

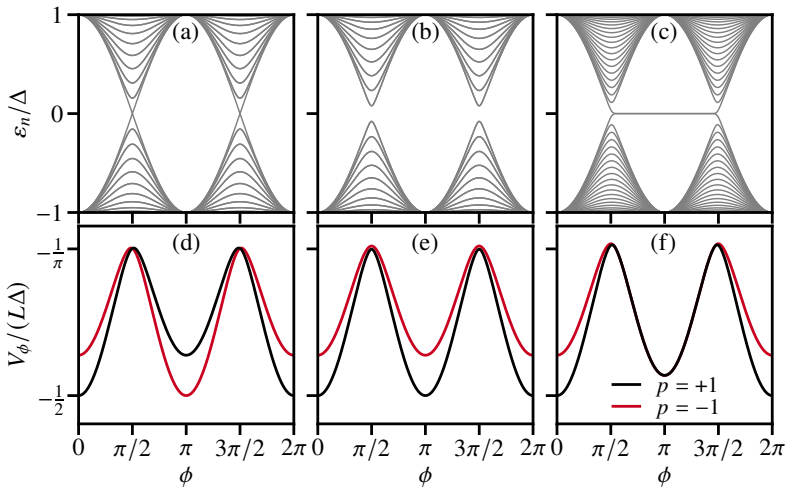

Fig. 3.1 (a)–(c) Single-particle energies of the fermionic Hamiltonian (3.1) for $L = 20$ sites. (a) For periodic boundary conditions, the single-particle gap closes, while (b) for anti-periodic boundary conditions, a gap of order $1/L$ remains; (c) for open boundaries, Majorana zero mode end states exist in the topological regime for $\pi/2 < \phi < 3\pi/2$; their energy splitting vanishes exactly for $\phi = \pi$. (d)–(f) Energies of the ground state and the first excited state, with the colour denoting even (black, $p = +1$) and odd (red, $p = -1$) fermion parity. (d) For periodic boundary conditions, the ground state parity is different in trivial and nontrivial sectors, while (e) the ground state parity is the same for anti-periodic boundaries; (f) for open boundaries, even and odd parities are nearly degenerate in the topological regime and exactly degenerate at $\phi = \pi$. When investigating tunnelling with open boundaries, we will consider a variant of this model where the ground state minima have equal depth, unlike in (f).

disappears at $\phi = \pi$) [25]. While OBC are conceptually closest to existing experimental planar Josephson junction setups [102, 103], our model (3.1) can serve as a prototypical example for tunnelling between topologically distinct phases also for the other boundary conditions.

A key ingredient to our considerations is a kinetic term for ϕ, motivated by the charging energy in superconducting islands [160]. Including this, the full Hamiltonian governing the fermionic $\hat{c}_k$ modes and the bosonic phase mode ϕ reads

$$\hat{H} = E_{\mathrm{C}}(\hat{N} - N_g)^2 + \frac{1}{2}\sum_k \hat{\xi}_k^\dagger \mathcal{H}_{\hat{\phi}}(k)\hat{\xi}_k \tag{3.2}$$

with the Nambu spinors $\hat{\xi}_k = (\hat{c}_k, \hat{c}_{-k}^\dagger)$, the charging energy E_{C}, and the bias charge N_g (in a superconductor this arises due to a gate voltage). The bosonic number operator $\hat{N}$ and the phase mode $\hat{\phi}$ are conjugate variables that satisfy $[\hat{\phi}, \hat{N}] = 2i$ for reasons we motivated in Sec. 1.2.1.

As is often the case when coupling a particle to a bath, $\hat{\phi}$ interacts with every fermion mode [153–157]; for our system this makes the coupling nonlocal. The system can be made local by including spatial fluctuations $\partial_x\phi$; in a superconducting system, neglecting these is justified provided that the length of the system is smaller than the Josephson penetration depth λ_J [174, 107] and the characteristic length L_H [175, 176] induced by a perpendicular magnetic field component [177].

Naïvely, we could replace the fermionic Hamiltonian (3.1) by its ground state energy; this corresponds to the particle tunnelling in the potential V_ϕ. The resulting dynamics would be essentially described by a $0-\pi$ Cooper pair box [178, 179]. Alluding to the superconductor analogy, we refer to energy scale characterizing V_ϕ as the Josephson energy, which for concreteness we define as $E_J \equiv (V_{\pi/2} - V_0)/2$. The scenario we outlined in the Introduction is one where the fermionic bath is gapped at the potential minima. This implies $\omega_0 \ll \Delta$ where $\omega_0 \propto \sqrt{E_C E_J}$ is the Josephson plasma frequency: the characteristic energy scale for the oscillations of the particle in the potential minima. We shall be interested in the regime where the tunnelling between these minima can be read off from the splitting between the energies of the particle's ground and first excited states. We thus require this splitting to be much smaller than the level spacing ω_0 characterizing each minima. In terms of the naïve potential tunnelling picture, this corresponds to $E_J/E_C \gg 1$.

3.3 Tunnelling and Instantons

Our goal is to estimate the influence of the fermions' topology change on the amplitude for tunnelling between V_ϕ's adjacent minima. Owing to the fermions being gapped near V_ϕ's minima, the particle simply experiences potential V_ϕ near the corresponding values of ϕ. However, since the tunnelling path involves a topology-changing gap closing, the picture of a particle tunnelling in potential V_ϕ is qualitatively incomplete.

To calculate the fermionic correction to the amplitude, one may consider taking a boson×fermion factorised wave function ansatz near the potential minima and applying a generalisation of linear combination of atomic orbitals (LCAO) [180] to this ansatz. While the exponential decaying overlap of the topologically distinct fermionic ground states already suggests a correction factor suppressing tunnelling exponentially with the fermionic system size, LCAO is known to inaccurately capture tunnelling exponents even in simple cases [181, 182]. Hence, one might worry that elevating LCAO to our more intricate scenario might miss key features. We therefore use a field theoretical approach instead that can incorporate bosonic and fermionic features on the same footing. In such field theories, tunnelling problems can be addressed via instantons [109], which will also be our method.

This is a semiclassical approach and hence requires working in the small tunnel splitting regime we are interested in.[1]

3.3.1 Path Integral

Our starting point is the partition function corresponding to the Hamiltonian (3.2). It can be written as a path integral over fields defined on an interval of imaginary time $\tau \in [0,\beta)$:

$$Z = \int \mathcal{D}\phi \mathcal{D}\boldsymbol{c} \mathcal{D}\bar{\boldsymbol{c}}\, e^{-S}, \tag{3.3}$$

where $\boldsymbol{c}, \bar{\boldsymbol{c}}$ are Grassmann variables satisfying anti-periodic temporal boundary conditions. The action $S = S_\phi + S_\mathrm{f}$ is composed of a bosonic part

$$S_\phi = \int_0^\beta d\tau \left[\frac{1}{2}\frac{1}{8E_\mathrm{C}}(\partial_\tau \phi_\tau)^2 + i\frac{N_g}{2}(\partial_\tau \phi_\tau)\right] \tag{3.4}$$

and a fermionic part [114]

$$S_\mathrm{f} = \frac{1}{2}\int_0^\beta d\tau\, \bar{\Psi}^T(\partial_\tau + \mathcal{H}_{\phi_\tau})\Psi, \tag{3.5}$$

where $\Psi = (\boldsymbol{c}, \bar{\boldsymbol{c}})$ is the Nambu spinor and $\mathcal{H}_\phi$ is the fermionic Bogoliubov-de-Gennes (BdG) Hamiltonian (3.1). The phase ϕ_τ appearing in the path integral is no longer compact and instead takes on any real value, subject to quasiperiodic boundary conditions $\phi_\beta = \phi_0 + 2\pi w$ which allow for nontrivial windings $w \in \mathbb{Z}$. The $\beta \to \infty$ limit of Z will give us information about the ground state of the system.

3.3.2 The Instanton Gas

To gain intuition into the tunnelling problem and a baseline to quantify the effect of the topology-changing fermions, we now consider a simpler problem, where we replace the fermionic Hamiltonian in Eq. (3.1) by its ground state energy V_ϕ, a double-well potential with minima $V_0 = V_\pi$ at $\phi = 0$ and $\phi = \pi$, respectively. (This is exemplified by APBC in Fig. 3.1(e) and can also be achieved for PBC and OBC by a suitable symmetrisation to be described below.) The resulting action $S_\mathrm{n} = S_\phi + U_\mathrm{n}$ is similar to Eq. (3.3), but since fermions

[1] The semiclassical nature of the small splitting regime can be seen from the tunnelling exponent $\hbar^{-1}\int\sqrt{2m[V(x)-E)}]dx$ for a particle of mass m and energy E in a potential V.

are absent, the fermionic action S_f has been replaced with what we dub the 'naïve potential'

$$U_\mathrm{n}[\phi_\tau] = \int_0^\beta d\tau\, V_{\phi_\tau}. \tag{3.6}$$

The naïve calculation closely follows that of Sec. 1.3.2, whose main results we now briefly recapitulate. The dominant contributions to this path integral come from ϕ_τ configurations that minimise S_n, the most significant being $\phi_\tau = 0$ and $\phi_\tau = \pi$, which stay at a minimum of the potential throughout. The action also has other subsidiary minima that contribute to Z at next-leading order, arising from extremal configurations of ϕ_τ which solve $\delta S_\mathrm{n} = 0$. Looking at the Euler-Lagrange equations resulting from S_n, the dynamics of ϕ (thought of as a position coordinate) are equivalent to a classical particle moving in a potential landscape $-V_\phi$ [114]. Thus in addition to staying at the top of the potential, the particle can move down from one extremum and up to another, where it can spend an arbitrary amount of time before returning, if the minima of V_ϕ are symmetric. The ϕ_τ solutions that connect the minima are called *instantons* (or *anti-instantons* when moving in the opposite direction) [109]. Their name refers to them being well-localised in (imaginary) time: their width (i.e., the time spent between the potential extrema) is of the order $1/\omega_0$, the harmonic oscillator frequency of the two wells, assumed to be the same. Each classical instanton has action $S_\mathrm{n}^\star$, and these can be chained together to form approximate solutions of the classical equations of motion. To capture the effect of tunnelling on the low-energy spectrum, we sum over all such solutions in the *instanton gas* summation [109].

Following Coleman's calculation [109], the symmetry of the minima $V_0 = V_\pi$ allows q instantons and $\bar{q}$ anti-instantons to appear at any time and in any order (provided one starts and ends in a minimum of the same type). Summing over all winding numbers $w \in \mathbb{Z}$, the leading terms in the partition function are given by

$$Z \propto e^{-\beta\left(V_0 + \frac{\omega_0}{2}\right)} \sum_w \sum_{q,\bar{q}=0}^{\infty} \delta_{w,\frac{q-\bar{q}}{2}} \frac{\left(\beta K e^{-S_\mathrm{n}^\star}\right)^{q+\bar{q}} e^{-i\frac{\pi}{2}N_g(q-\bar{q})}}{q!\,\bar{q}!}. \tag{3.7}$$

K is a fluctuation factor associated with each instanton, whose value shall not concern us. Splitting up the $\sum_{q/\bar{q}}$ summations into even and odd contributions, we see that the partition function is given by

$$Z \propto e^{-\beta\left(V_0 + \frac{\omega_0}{2}\right)} \cosh\left[2\beta K e^{-S_\mathrm{n}^\star} \cos\left(\frac{\pi}{2} N_g\right)\right]. \tag{3.8}$$

By comparing this to the form $Z = \mathrm{Tr}\{[\sum_n e^{-\beta E_n} |n\rangle \langle n|]\}$, we deduce that the low-energy spectrum is given by

$$E_{\pm}(N_g) = V_0 + \frac{\omega_0}{2} \pm 2Ke^{-S_{\mathrm{n}}^{\star}} \cos\left(\frac{\pi}{2} N_g\right), \tag{3.9}$$

which is the familiar tight-binding dispersion with tunnelling amplitude $t_{0\to\pi} = 2Ke^{-S_{\mathrm{n}}^{\star}}$ between states at $\phi = 2m\pi$ and $\phi = (2m+1)\pi$ that otherwise have equal energy. The action appearing in the exponent consists of equal kinetic and potential energy parts and is given by

$$S_{\mathrm{n}}^{\star} = \frac{1}{2\sqrt{E_{\mathrm{C}}}} \int_0^{\pi} d\phi \sqrt{V_\phi - V_0}, \tag{3.10}$$

which is the source of the exponential suppression of charge noise with $E_{\mathrm{J}}/E_{\mathrm{C}}$ in transmons [108, 183].

A key assumption behind the instanton gas summation is that the gas is dilute [109]. The instanton density is $\propto \exp(-S_{\mathrm{n}}^{\star})$ [109], hence the diluteness assumption amounts to requiring small tunnel splitting, placing us in the regime we are interested in.

Note that to be able to read out the $0 \to \pi$ tunnelling amplitude from the spectrum, we required the minima to be equal. Had this not been the case, supposing instead that $V_0 < V_\pi$, the classical solutions would more closely resemble a sequence of $0 \to 2\pi$ instantons separated by large imaginary time durations, rather than $0 \to \pi$ instantons [116]. In this limit we would get a ground state energy that disperses as $\cos(\pi N_g)$, i.e., with halved N_g periodicity, corresponding to the 2π-periodicity of the potential encoding Cooper pair tunnelling (instead of the electron quartet tunnelling encoded by π periodicity [178, 179]). We mention this because the ground state energy of the double-well Kitaev model, as written in Eq. (3.1), is symmetric only for APBC, as seen from Fig. 3.1. With PBC, although the minima have equal energies, their ground state parities are different due to the gap closing, and hence the minima are completely decoupled for fixed parity. OBC has an asymmetric ground state profile even without fixing parity because the gapped bulk modes are replaced by zero-energy Majorana end modes in the topological phase, which do not contribute to the ground state energy. For PBC and OBC, we therefore have to consider variants of the model with symmetric minima, in order for the magnitude of the $0 \to \pi$ tunnelling to be visible in the low-energy spectrum. Due to its closer link to our inspiring topological superconducting systems [100–103] and features that Majorana end modes may present, of these two cases we mainly focus on OBC, while we include APBC for its relative technical simplicity.

3.3.3 Integrating Out Fermions

Our goal is to capture the modification of $t_{0\to\pi}$ due to the topology-changing fermions. To compute this, we now return to the full many-body path integral in Eq. (3.3). The fermionic Lagrangian is bilinear in the fermionic fields and so we can perform a Gaussian integral to obtain [184]

$$\int \mathcal{D}\boldsymbol{c}\mathcal{D}\bar{\boldsymbol{c}}\, e^{-S_{\mathrm{f}}} = \mathrm{Pf}\left[\partial_\tau + \mathcal{H}^M_{\phi_\tau}\right], \tag{3.11}$$

where $\mathcal{H}^M_\phi = -[\mathcal{H}^M_\phi]^T = W\mathcal{H}_\phi W^\dagger$ is the Hamiltonian written in the Majorana basis with $W = \frac{1}{\sqrt{2}}\left(\begin{smallmatrix} 1 & 1 \\ -i & i \end{smallmatrix}\right)$. Thus by integrating out the fermions we have obtained a partition function expressed as a path integral of the phase only

$$Z = \int \mathcal{D}\phi\, e^{-S_\phi}\, \mathrm{Pf}\left[\partial_\tau + \mathcal{H}^M_{\phi_\tau}\right] / \mathrm{Pf}\left[\partial_\tau + \mathcal{H}^M_{0\mathrm{i}}\right], \tag{3.12}$$

albeit one with a complicated (temporally nonlocal) action. Because of the continuous ∂_τ term, the Pfaffian needs to be regularised and so we divide by the Pfaffian for the static phase profile $\phi_\tau = 0 \equiv \phi_{0\mathrm{i}}$ without instantons.[2] The suppression of tunnelling due to topology-changing fermions originates in the deviation of this Pfaffian ratio from the naïve potential, a point we will further elucidate in Sec. 3.5.1 (where we will also find that our regularisation is analogous to an offset sending $V_0 \to 0$).

Since we are interested only in the magnitude of this fermionic suppression, it will be simpler work with the determinant. In terms of this,

$$\sqrt{\det\left[\partial_\tau + \mathcal{H}_{\phi_\tau}\right]} = \mathrm{Pf}\left[\partial_\tau + \mathcal{H}^M_{\phi_\tau}\right] \tag{3.13}$$

up to a sign that plays no role in our considerations[3]. This fermionic factor defines what we refer to as the 'fermionic potential'

$$U_{\mathrm{f}}[\phi_\tau] \equiv -\frac{1}{2}\log\det\left[\partial_\tau + \mathcal{H}_{\phi_\tau}\right], \tag{3.14}$$

although as it stands only $U_{\mathrm{f}}[\phi_\tau] - U_{\mathrm{f}}[\phi_{0i}]$ corresponding to the Pfaffian ratio is well defined. Unless stated otherwise (cf. Sec. 3.5.1), henceforth we consider this difference and compare with the naïve case with a similarly subtracted naïve potential (this subtraction is just an inconsequential energy offset in the naïve case). Crucially, the relevant phase profiles ϕ_τ

[2] We choose subscript 0i to represent zero instantons and use it with both phase profiles and Hamiltonians.

[3] For the chirally symmetric system we consider, we always have a real quantity $\det\left[\partial_\tau + \mathcal{H}_{\phi_\tau}\right] / \det[\partial_\tau + \mathcal{H}_{0\mathrm{i}}] > 0$ for all ϕ_τ, so the sign of the corresponding Pfaffian never changes.

contributing to the path integral still resemble those of the instanton gas, so our partition function can be expanded in the same way as Eq. (3.7) but with modified action.

3.4 Tunnelling Suppression via Topology in $d+1$ Dimensions

We next explain how the instantons connecting minima where $\mathcal{H}_{\phi_\tau}$ has distinct topology can be linked to topologically protected d-dimensional gapless boundary modes in a topological Hamiltonian in $d+1$ dimensions. At the core of this correspondence is imaginary time supplying an extra dimension that, in a manner akin to reversing dimensional reduction [17, 18, 127, 169], allows one to climb a step higher in a dimensional hierarchy.

By Eq. (3.13), we require the product of all eigenvalues of the (non-Hermitian) kernel $\mathcal{L}(\tau) = \partial_\tau + \mathcal{H}_{\phi_\tau}$. When $\mathcal{H}_{\phi_\tau}$ enjoys a chiral symmetry, $\{\Gamma, \mathcal{H}_\phi\} = 0$ with Γ a gamma matrix (i.e., a Pauli matrix or its Hermitian higher-dimensional generalisation [185]), then $\tilde{\mathcal{H}}(\tau) = i\Gamma\mathcal{L}(\tau)$ is a Hermitian operator. [Note that $\det\tilde{\mathcal{H}}(\tau) = \det\mathcal{L}(\tau)$ since $\det i\Gamma = 1$.] If chiral symmetry is absent, it can be introduced by doubling, i.e., considering $\mathcal{L}'(\tau) = \partial_\tau + \mathcal{H}_{\phi_\tau}\otimes\sigma_a$ with Pauli matrix σ_a (and taking another square root of the corresponding determinant to recover the Pfaffian, as done in the $d=0$ example of Ref. [168]). Now $\tilde{\mathcal{H}}(\tau) = i\Gamma\mathcal{L}'(\tau)$, with $\Gamma = \mathbb{1}\otimes\sigma_b$ ($b\neq a$), which is again Hermitian. The operator $\tilde{\mathcal{H}}(\tau)$ can be interpreted as a Hamiltonian in $d+1$ dimensions. The steps leading to $\tilde{\mathcal{H}}(\tau)$, including the doubling in the non-chiral case, parallel closely (the reversal of) features in dimensional reduction procedures for topological insulators and superconductors [18].

Topologically protected gapless interface states at instanton locations are guaranteed to arise because, at low energies, the topological transition (with ϕ_τ) of $\mathcal{H}_{\phi_\tau}$ reduces to a mass inversion of a d-dimensional Dirac Hamiltonian which, in turn, becomes a τ-dependent mass kink for $\tilde{\mathcal{H}}(\tau)$ in $d+1$ dimensions. Such mass kinks, by a generalisation of the Jackiw-Rebbi mechanism [31], bind d-dimensional topologically protected gapless modes, a key feature underlying topological insulators' and superconductors' robust boundary modes [186, 17, 18].

For our toy model Eq. (3.1), $\{\sigma_1, \mathcal{H}_\phi\} = 0$ and thus

$$\begin{aligned}\tilde{\mathcal{H}}(\tau) = i\sigma_1\mathcal{L}(\tau) = &\frac{\Delta}{2}\cos\phi_\tau\left[(1+\cos k)\,\sigma_2 - \sin k\,\sigma_3\right]\\ &+\frac{\Delta}{2}\left[(1-\cos k)\,\sigma_2 + \sin k\,\sigma_3\right] + i\partial_\tau\sigma_1\end{aligned} \tag{3.15}$$

is Hermitian. It is a $d=2$ class D superconductor Hamiltonian. Each instanton, i.e., a phase slip of ϕ by π, corresponds to a topological transition of $\tilde{\mathcal{H}}(\tau)$; the corresponding interface states are shown schematically in Figs. 3.2 and 3.3.

3.4.1 Sharp Instanton Limit

While the shape of ϕ_τ and the fermionic spectrum are interdependent and hence solving for them is a nontrivial problem, certain limiting cases for ϕ_τ allow for tractable examples that illuminate generic topological features dictating the behaviour of the Pfaffian ratio. We next focus on such a case, specifically on the "sharp instanton limit" of instantons with vanishingly short width. Although, since the instanton width is set by $1/\omega_0$, such sharp instantons are beyond the $\omega_0 \ll \Delta$ regime, they are not only analytically tractable, but (as we shall justify in Sec. 3.5.2) they also correspond to the biggest discrepancy between the fermionic and naïve potentials, and hence will allow us to bound the fermionic suppression of $t_{0\to\pi}$.

A key simplification of the sharp instanton limit is that for such instantons there is no time spent away from the minima to accumulate potential contributions to the naïve action and so $U_\mathrm{n}[\phi_{2m\mathrm{i}}] = U_\mathrm{n}[\phi_{0\mathrm{i}}]$ for a profile $\phi_{2m\mathrm{i}}$ with $2m$ sharp instantons. For the fermionic potential, however, we will show that $U_\mathrm{f}[\phi_{2m\mathrm{i}}] \gg U_\mathrm{f}[\phi_{0\mathrm{i}}]$. Evaluating the Pfaffian ratio for a profile $\phi_{2m\mathrm{i}}$ amounts to comparing the energies of $\tilde{\mathcal{H}}_{2m\mathrm{i}}(\tau)$ with those of a static Hamiltonian $\tilde{\mathcal{H}}_{0\mathrm{i}}(\tau)$, where $\tilde{\mathcal{H}}_{n\mathrm{i}}(\tau)$ is $\tilde{\mathcal{H}}(\tau)$ on the background of n sharp instantons. Since the spectrum of $\tilde{\mathcal{H}}(\tau)$ is qualitatively different for OBC versus APBC, we discuss each case separately.

APBC

Antiperiodic boundary conditions are the simplest to deal with: Translational invariance means we can stay in momentum space along the spatial direction. Each instanton changes the sign of $\cos\phi_\tau$ and corresponds to a topological transition of $\tilde{\mathcal{H}}(k,\tau)$ that binds low-energy chiral modes with dispersion

$$E_\parallel^\pm(k) = \pm\Delta\sin(k/2) \tag{3.16}$$

to the interface (derived in Appendix B.1), where chirality depends on the direction of the sign change of $\cos\phi_\tau$. To find the contribution of each instanton to $\det\{\tilde{\mathcal{H}}(\tau)\}$, we take the product of the energies of all sub-gap states sampled by momenta $k_n = (2n+1)\pi/L$ consistent with APBC for L sites. All these states would otherwise be at the gap energy Δ, so the determinant ratio for a configuration with $2m$ phase transitions is given, up to an inconsequential sign, by

$$\frac{\det\{\tilde{\mathcal{H}}_{2m\mathrm{i}}(\tau)\}}{\det\{\tilde{\mathcal{H}}_{0\mathrm{i}}(\tau)\}} = \left[\prod_{n=0}^{L-1}\sin(k_n/2)\right]^{2m} = \left[2^{-(L-1)}\right]^{2m}, \tag{3.17}$$

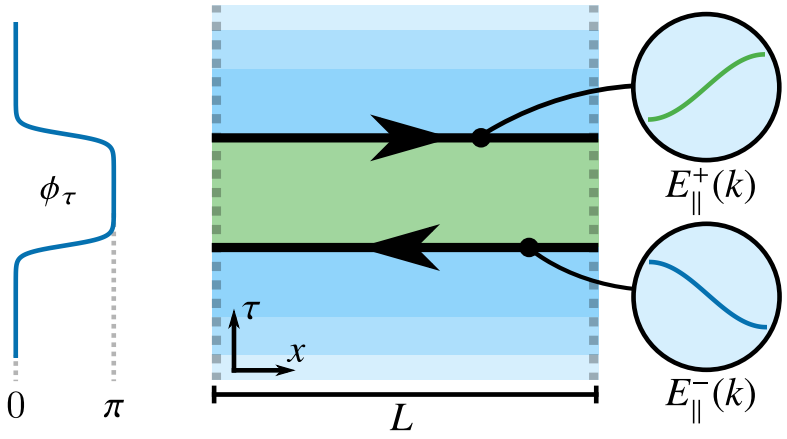

Fig. 3.2 A cartoon showing the edge modes of $\tilde{\mathcal{H}}(k,\tau)$ for an instanton-anti-instanton configuration (left) with twisted boundary conditions. On the right are the dispersions $E_\parallel^\pm(k)$ of the two edge modes, showing they have different chirality.

since other supra-gap states remain unchanged. The last equality makes use of a trigonometric identity [4], but one expects an $e^{-\alpha L}$ dependence for edge mode dispersions of any shape since the logarithm of the product can be approximated by an integral in the large L limit [5].

When instantons are very close, the exponentially localised edge modes with opposite chirality can overlap and gap out, but as instantons separate, this small exponential splitting is quickly dwarfed by $E_\parallel^+(\pi/L)$. Thus, the dilute instanton gas approximation [109] remains valid. (In fact, the approximation is even better justified than in the naïve case since the instanton density is exponentially suppressed in the instanton action [109] so the gas is further rarefied in the presence of fermions due to the increased instanton action.)

Generalizing the calculation of Eq. (3.9) to the case with fermions, the tunnel amplitude is still set by the single-instanton action, which is half of that of the two-instanton case, the minimal configuration allowed by the $\phi_0 \equiv \phi_\beta$ temporal boundary conditions imposed by the partition function. (While $\phi \equiv \phi + 2\pi$ due to charge quantisation, $\phi \not\equiv \phi + \pi$ notwithstanding $V_0 = V_\pi$.) Although the naïve potential $U_\mathrm{n}[\phi_{2\mathrm{i}}] - U_\mathrm{n}[\phi_{0\mathrm{i}}] \to 0$ vanishes for sharp instantons $\phi_{2\mathrm{i}}$ (where the subtraction of $U_\mathrm{n}[\phi_{0\mathrm{i}}]$ follows the naive potential limit of the Pfaffian ratio, cf. Sec. 3.5.1), the topologically guaranteed chiral modes of $\tilde{\mathcal{H}}_{2\mathrm{i}}(\tau)$ mean that the fermionic potential approaches a lower bound $U_\mathrm{f}[\phi_{2\mathrm{i}}] - U_\mathrm{f}[\phi_{0\mathrm{i}}] \to (L-1)\log 2$ upon reducing the instanton width.

[4] This is a specific case of the general identity $\sin(Lx) = 2^{L-1}\prod_{k=0}^{L-1}\sin(x + k\pi/L)$ which follows from writing the L roots of unity as $z^L - 1 = \prod_{k=0}^{L-1}(z - e^{-i2\pi k/L})$. Dividing by the first term and taking $x \to 0$ also gives $L = 2^{L-1}\prod_{k=1}^{L-1}\sin(k\pi/L)$, which can be used for PBC.

[5] For a positive function $f(k)$ we have $\log\prod_{n=0}^{L-1} f(k_n) = \sum_{n=0}^{L-1}\log f(k_n) \to ([L-1]/2\pi)\int_0^{2\pi} dk\, f(k)$ for $L \gg 1$.

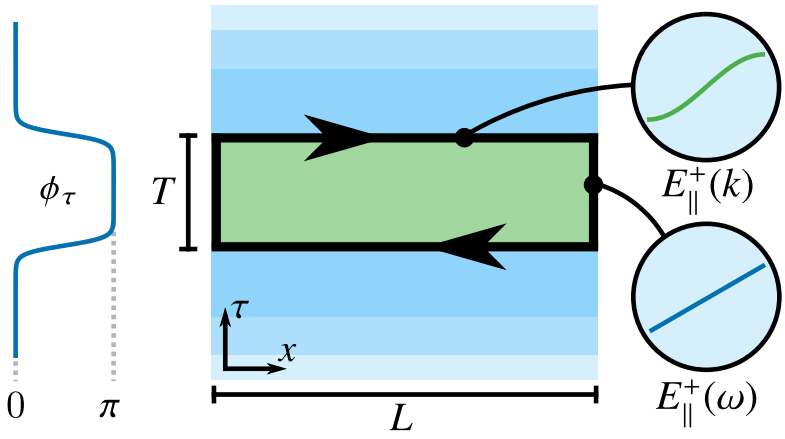

Fig. 3.3 A cartoon showing the edge mode for an instanton-anti-instanton configuration with OBC, separated by imaginary time T. The chiral mode runs along the entire boundary of the topological region. Shown on the right are the dispersions along different sections of the perimeter.

This sharp instanton limit is the regime with the strongest suppression of tunnelling due to fermions (cf. Sec. 3.5.2), and so by modifying the instanton action appearing in the spectrum (3.9), we can bound by how much the naïve tunnelling amplitude $t^{(\mathrm{n})}_{0\to\pi}$ can be modified by fermions. For APBC, Eq. (3.17) implies

$$t^{(\mathrm{f})}_{0\to\pi} \geq e^{-\frac{1}{2}(L-1)\log 2}\, t^{(\mathrm{n})}_{0\to\pi}. \tag{3.18}$$

Thus the tunnelling is exponentially suppressed as a function of system size. Since it derives entirely from the topological boundary modes of $\tilde{\mathcal{H}}_{2\mathrm{i}}(\tau)$, this bound on the scaling exponent is purely due to the topological inequivalence of the two ground states, and is unrelated to the trivial scaling of V_ϕ with L. (Any information about the energy scale Δ was lost when taking the ratio of energies, but this is unique to the sharp instanton limit since we will later see that the scale of the potential influences the instanton timescale and hence the fermionic factor.)

OBC

Open boundary conditions are technically more difficult to treat because we cannot work in momentum space. Recall that the topological limit of the 1D Kitaev chain has zero-energy Majorana end modes [25]. When adding the $i\partial_\tau\sigma_1$ term, these Majorana modes gain a linear dispersion in the temporal direction, given by

$$E_{\parallel}^{\pm}(\omega) = \pm\omega. \tag{3.19}$$

This means that for two instantons separated by imaginary time T, instead of having counterpropagating chiral edge modes in a ribbon geometry as for APBC, these edge modes run all the way around the perimeter of the 2D $(T \times L)$-sized topological region, shown in Fig. 3.3. The differing dispersions in each direction mean that the frequency ω and wave vector k on the different sections are related through the energy matching condition

$$E_{\parallel}^{+}(\omega) = E_{\parallel}^{+}(k). \tag{3.20}$$

As a fermion traverses this perimeter, it undergoes one whole rotation and must acquire a phase $e^{i\pi}$, which gives a quantisation condition

$$2T\omega + 2Lk = (2n+1)\pi, \tag{3.21}$$

with $n \in \mathbb{Z}$ that can be solved simultaneously with Eq. (3.20) to obtain the quantised energies of the chiral modes. We then follow the same principle of taking the product of these energies as a fraction of the gap.

Although the quantisation condition lacks algebraic solutions, we numerically find that Eq. (3.21) leads to a product [generalizing Eq. (3.17)] that depends exponentially on T. Intuitively, this is a consequence of the asymmetry in the ground state for OBC: Recall from Fig. 3.1 that for OBC the ground state minima are offset by Δ, which means that the naïve action would accumulate a contribution $\int d\tau V_{\phi_\tau} = T\Delta$ when ϕ_τ spends a duration T in the higher well. The result for multiple pairs of instantons follows by summing over all pair separations $\tau_{2j} - \tau_{2j-1}$ which govern the sizes of topological regions. The presence of $e^{-(\tau_{2j}-\tau_{2j-1})\Delta}$ terms prevents us from plugging our result into Eq. (3.7) as a modified instanton action because the integral over instanton locations $\{\tau_i\}$ (a key step leading to Eq. (3.7), c.f. Ref. [109]) will be fundamentally different—the instantons are now *interacting*. However, as mentioned in Sec 3.3.2, asymmetric wells do not tell us about $0 \to \pi$ tunnelling, so we must symmetrise the wells. We therefore change the gap on the trivial side to $\Delta' = \Delta(1 - 1/L)$. One intuitively expects that having thus symmetrised the wells, i.e., removed the $\int d\tau V_{\phi_\tau} = T\Delta$ contribution, we have eliminated the instanton interactions, which allows us to interpret what remains as a modified instanton action. This will indeed turn out to be the case, however it requires more careful justification: by symmetrizing the wells we introduced a gap asymmetry and this requires us to consider more than just the chiral edge modes (which themselves are also modified).

The first modification is that when changing $\Delta \to \Delta'$ in the trivial phase, the dispersion of the chiral modes along x is replaced by $E_{\parallel}'^{\pm}(k)$, as we detail in Appendix B.1, which changes the energy matching equation (3.20). Letting $k_n^\star$ denote the quantised momenta of states

running around the edge of length $2T+2L$, we numerically find that

$$\prod_n \frac{E'^{+}_{\parallel}(k^\star_n)}{\Delta'} \approx \exp\{[-2(L-1)\log 2 - 4T\Delta'/\pi]\}. \tag{3.22}$$

For OBC, energies above the gap are also modified by the existence of a topological region. There are two kinds of supra-gap states that are modified. The first kind is the set of states that are localised at the ends of the chain, but propagate along the temporal direction. In the trivial gapped region, these end states have dispersion

$$E^{\pm}_{\Delta'}(\tilde{\omega}) = \pm\sqrt{\tilde{\omega}^2+\Delta'^2} \tag{3.23}$$

that must match the energy $E^{\pm}_{\parallel}(\omega)$ in the topological region. This time, the quantisation condition comes from the APBC for fermions in the path integral:

$$(\beta - T)\tilde{\omega} + T\omega = (2n+1)\pi. \tag{3.24}$$

The supra-gap energies in the absence of any instantons are recovered by setting $T=0$ in the above equation. Denoting the quantised frequencies by $\tilde{\omega}^\star_n$ and counting both positive and negative energies, as $\beta\to\infty$ the relevant ratio tends to

$$\left[\prod_n \frac{E^{+}_{\Delta'}(\tilde{\omega}^\star_n)}{\sqrt{(2n+1)^2\pi^2/\beta^2+\Delta'^2}}\right]^2 = \exp\{[-2T\Delta'(1-2/\pi)]\}. \tag{3.25}$$

The other kind of supra-gap states describes those in the bulk of the superconducting chain, whose energies are affected by the presence of instantons only because we have $\Delta'\neq\Delta$, but not for topological reasons. Since $\Delta>\Delta'$, these energies *increase* when more time is spent in the topological phase and their combined effect will be to cancel the exponential decay with instanton separation that we have seen in Eqs. (3.22) and (3.25). The most significant contribution comes from states above the larger gap Δ. These are solved through a quantisation condition similar to Eq. (3.24), but this time one must match $E^{\pm}_{\Delta'}(\tilde{\omega})$ with $E^{\pm}_{\Delta}(\omega)=\pm\sqrt{\omega^2+\Delta^2}$. Each of these states are $(L-1)$-fold degenerate because each can be localised on any of the $2L-2$ Majoranas not on the ends of the chain. There are also bulk states with energies between Δ' and Δ, whose increasing energies with T make up the remaining contribution. Since these states do not fully penetrate the topological region, their energies are approximately as though their frequencies $\tilde{\omega}$ were quantised through being antiperiodic over a shorter system of length $(\beta-T)$. Taking into account both types of bulk

states, in the same $\beta \to \infty$ limit, we now have

$$\left[\prod_n \frac{E^+_\Delta(\omega^\star_n)}{\sqrt{(2n+1)^2\pi^2/\beta^2+\Delta'^2}}\right]^{2(L-1)} = \exp[2T\Delta']. \tag{3.26}$$

Combining all these contributions, the determinant ratio for two sharp instantons separated by T is

$$\frac{\det\tilde{\mathcal{H}}_{2\mathrm{i}}(\tau)}{\det\tilde{\mathcal{H}}_{0\mathrm{i}}(\tau)} \approx \exp[-2(L-1)\log 2]. \tag{3.27}$$

Thus, after symmetrisation, one finds the same bound on the suppression due to fermions for OBC as in Eq. (3.18) for APBC.

3.5 Tunnelling Suppression from a Variational Approach

Although the argument based on topological edge modes quickly gave us an upper bound on the suppression due to fermions, it cannot easily be extended to give full quantitative results. The problem is that typical instantons in the gas are not perfectly sharp, and instead have a finite timescale. Despite the spectrum of the topological edge modes being independent of instanton shape, a finite instanton timescale leads to other nontopological bound states at the phase transition whose energies *do* depend on instanton shape [187]. Analytic results for the full spectrum of a generic phase profile do not exist, and an approximate spectrum would not suffice because estimating the tunnelling suppression relies on the precise difference between the fermionic determinant and its naïve equivalent.

3.5.1 Fermionic Factor as a Generalisation of the Ground State Potential

We now describe an exact approach to calculating the fermionic potential. This approach works directly with the kernel underlying the Pfaffian, without requiring converting to a Hermitian matrix and hence chiral symmetry. It will also give an interpretation of the fermionic determinant by linking it to the one-dimensional potential generated by the ground state of the BdG system.

We start by writing

$$\det\left[\partial_\tau + \mathcal{H}_{\phi_\tau}\right] = \prod_{nm} \lambda_{nm}, \tag{3.28}$$

where λ_{nm} are the eigenvalues of the differential equation

$$\left[\partial_\tau + \mathcal{H}_{\phi_\tau}\right]\psi_{nm}(\tau) = \lambda_{nm}\psi_{nm}(\tau), \tag{3.29}$$

which has eigenfunctions of the form

$$\psi_{nm}(\tau) = \mathcal{T}\exp\left[\int_0^\tau d\tau' \left(\lambda_{nm} - \mathcal{H}_{\phi_{\tau'}}\right)\right]\psi_{nm}(0). \tag{3.30}$$

Time-ordering (with later times appearing on the left) is required because the BdG Hamiltonian does not generally commute at different times, $\left[\mathcal{H}_{\phi_\tau}, \mathcal{H}_{\phi_{\tau'}}\right] \neq 0$. Temporal APBC for fermions $\psi_{nm}(\beta) = -\psi_{nm}(0)$ fixes the eigenvalues to be

$$\lambda_{nm} = i\omega_n + \frac{1}{\beta}\log\left\{\mathcal{T}\exp\left[-\int_0^\beta d\tau\, \mathcal{H}_{\phi_\tau}\right]\right\}_m \tag{3.31}$$

$$\equiv i\omega_n - \{\mathcal{H}_{\text{eff}}[\phi_\tau]\}_m\,, \tag{3.32}$$

where $\omega_n = (2n+1)\pi/\beta$ with $n \in \mathbb{Z}$ are the Matsubara frequencies and $\{\bullet\}_m$ denotes the mth eigenvalue of an operator we denote as the effective Hamiltonian $\mathcal{H}_{\text{eff}}[\phi_\tau]$ (emphasizing that it depends on the entire ϕ_τ profile). The spectrum of $\mathcal{H}_{\text{eff}}[\phi_\tau]$ inherits PH symmetry.

When taking the product of these eigenvalues, we may use the Weierstrass factorisation theorem to rewrite the determinant as [188]

$$\det\left[\partial_\tau + \mathcal{H}_{\phi_\tau}\right] = \prod_m \left(\prod_n i\omega_n\right)\cosh\left[\frac{\beta}{2}\{\mathcal{H}_{\text{eff}}[\phi_\tau]\}_m\right]. \tag{3.33}$$

Upon taking the ratio, the normalisation-dependent prefactor drops out to give

$$\frac{\det\left[\partial_\tau + \mathcal{H}_{\phi_\tau}\right]}{\det[\partial_\tau + \mathcal{H}_{0\text{i}}]} = \prod_m \frac{\cosh\left[(\beta/2)\{\mathcal{H}_{\text{eff}}[\phi_\tau]\}_m\right]}{\cosh\left[(\beta/2)\{\mathcal{H}_{\text{eff}}[\phi_{0\text{i}}]\}_m\right]}, \tag{3.34}$$

whose numerator is the partition function for a BdG Hamiltonian $\mathcal{H}_{\text{eff}}[\phi_\tau]$.

To make the link to the naïve potential, consider a case where $\mathcal{H}_{\phi_\tau}$ commutes at all times, such that $\mathcal{H}_{\text{eff}}[\phi_\tau] = \frac{1}{\beta}\int_0^\beta d\tau\, \mathcal{H}_{\phi_\tau}$ and hence $\{\mathcal{H}_{\text{eff}}[\phi_\tau]\}_m = I_m[\phi_\tau] = \frac{1}{\beta}\int_0^\beta d\tau \varepsilon_{\phi_\tau,m}$ with $\varepsilon_{\phi_\tau,m}$ the instantaneous single particle energies of $\mathcal{H}_{\phi_\tau}$ (taken to evolve continuously with ϕ_τ through any level crossing). In the sense of $I_m[\phi_\tau]$, both the APBC and OBC systems are gapped provided ϕ_τ spends significant time near $\phi = 0$. Therefore, when ignoring the evolution of eigenstates with superconducting phase, the fermionic factor tends (upon taking β much larger than the inverse of the I_m gap) to the action of a potential that is the ground state energy. By the same logic, by noting $I_m[\phi_{0\text{i}}] = \varepsilon_{\phi=0,m}$, the denominator in Eq. (3.34) can be seen to subtract $\varepsilon_{\phi=0,m}$ from each $\varepsilon_{\phi_\tau,m}$, thus supplying an offset setting the minimum value of this potential to zero.

When the eigenstates of the BdG Hamiltonian evolve as a function of phase, Eq. (3.34) is viewed as the generalisation of the ground state potential action and the spectrum of the time-ordered quantity $\mathcal{H}_{\text{eff}}[\phi_\tau]$ must be evaluated properly. The importance of eigenstate evolution is also clear if we diagonalise the BdG Hamiltonian in the path integral from the outset as $\mathcal{H}_\phi = X_\phi[\oplus_m \varepsilon^+_{\phi,m}\sigma_3]X^\dagger_\phi$. Then, the fermionic determinant is replaced by[6]

$$\det\left[\partial_\tau + \mathcal{H}_{\phi_\tau}\right] \to \det\left[\partial_\tau + \oplus_m \varepsilon^+_{\phi_\tau,m}\sigma_3 + X^\dagger_{\phi_\tau}\partial_\tau X_{\phi_\tau}\right], \tag{3.35}$$

where we see the last term, i.e., the eigenstate evolution, being responsible for the deviation from $\{\mathcal{H}_{\text{eff}}[\phi_\tau]\}_m = I_m[\phi_\tau]$, i.e., from the naïve case. In Appendix B.2, we show that including eigenstate evolution always increases the naïve action.

These considerations, in particular the cancellation in Eq. (3.34), also show how one can define an unsubtracted variant of the fermionic potential: the functional

$$\tilde{U}_{\text{f}}[\phi_\tau] = -\frac{1}{2}\sum_m \log\cosh\left[(\beta/2)\,\{\mathcal{H}_{\text{eff}}[\phi_\tau]\}_m\right] \tag{3.36}$$

satisfies $\tilde{U}_{\text{f}}[\phi_\tau] - \tilde{U}_{\text{f}}[\phi_{0i}] = U_{\text{f}}[\phi_\tau] - U_{\text{f}}[\phi_{0i}]$ hence is a useful candidate for a "standalone" fermionic potential. Another useful feature is $\tilde{U}_{\text{f}}[\phi_{0i}] = U_{\text{n}}[\phi_{0i}]$, thus the difference of subtracted fermionic and naïve potentials is simply $\tilde{U}_{\text{f}}[\phi_\tau] - U_{\text{n}}[\phi_\tau]$. In what follows, one can thus envision Eq. (3.36) as a fermionic potential, and view the regularisation in Eq. (3.12) as providing a constant energy offset via $\tilde{U}_{\text{n}}[\phi_{0i}]$. In what follows, we refer to $\tilde{U}_{\text{f}}[\phi_\tau]$, together with this constant offset (to maintain consistency with previous sections) as our fermionic potential and drop the tilde to ease notations.

3.5.2 Variational Instanton Strategy

The effective bosonic theory has a potential $U_{\text{f}}[\phi_\tau]$ that is nontrivial to evaluate even for a given profile ϕ_τ, and the dependence of the profile itself on $U_{\text{f}}[\phi_\tau]$ leads to an even more complex problem. We now outline a strategy to tackle this problem variationally. The crux of this strategy is to again expand the partition function as an instanton gas, motivated by the link we made in Sec. 3.5.1 between the fermionic Pfaffian factor and the ground state potential. The shapes of the classical instantons making up the gas are still the result of competition between kinetic and potential energy but with the new effective potential $U_{\text{f}}[\phi_\tau]$ their features may change compared with the naïve case. To facilitate relating to our sharp-instanton results we use the instanton width as a variational parameter. Specifically, we will allow

[6] This equivalent form is generally less convenient for numerical calculations for the same reasons that Wilson loops are often more convenient than Berry phase integrals.

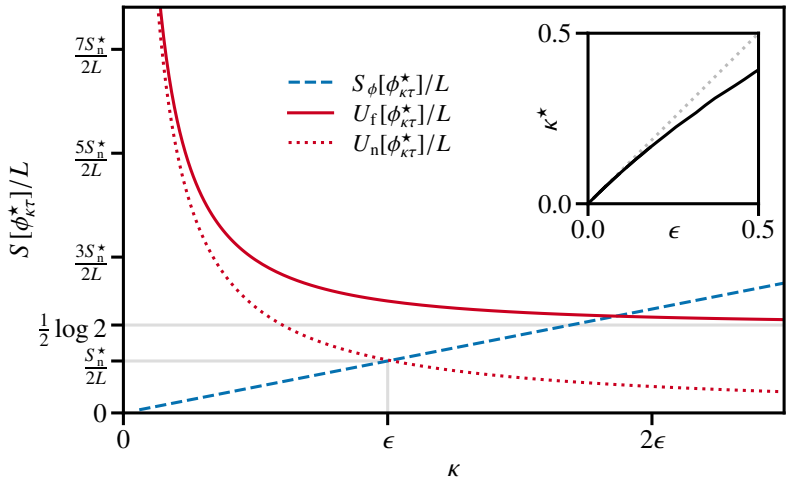

Fig. 3.4 A typical plot of $U_f[\phi^\star_{\kappa\tau}]/L$ and $U_n[\phi^\star_{\kappa\tau}]/L$ against κ. As $\kappa \to 0$, the fermionic potential tends to the naïve one, but as $\kappa \to \infty$ it approaches $\frac{1}{2}\log 2 + O(1/L)$. Also plotted is the kinetic energy $S_\phi[\phi^\star_{\kappa\tau}]/L$. In terms of κ and $\epsilon = \sqrt{E_C E_J}/\Delta$ (set to $\epsilon = 0.3$ above), the kinetic and naïve potential energies of an individual instanton are $S_\phi[\phi^\star_{\kappa\tau}] = S_n^\star \kappa/(2\epsilon) \propto \kappa\Delta/E_C$ and $U_n[\phi^\star_{\kappa\tau}] = S_n^\star \epsilon/(2\kappa) \propto E_J/(\kappa\Delta)$, respectively, where $S_n^\star$ is the classical action given in Eq. (3.10). The inset shows how the optimal rescaling factor $\kappa^\star$ tracks its naïve counterpart ϵ.

the timescale of instantons to be different to their naïve counterparts $\phi^\star_\tau$ by considering scaled instantons $\phi^\star_{\kappa\tau}$ where we replace $\tau \to \kappa\tau$. Since naïve instantons for different values of $\omega_0 \propto \sqrt{E_C E_J}$ are themselves related to each other by rescaling [in the action, $E_C E_J$ sets merely the overall scale of the potential relative to $(\partial_\tau \phi)^2$], we can choose to define $\phi^\star_\tau$ as the naïve instanton for $\sqrt{E_C E_J} = \Delta$. (As this is just a reference classical configuration, it need not obey the $\sqrt{E_C E_J} \ll \Delta$ restriction.) By defining $\phi^\star_\tau$ in this way, and optimizing over $\phi^\star_{\kappa\tau}$, the naïve action is minimised for $\kappa = \sqrt{E_C E_J}/\Delta$, the rescaling required to get from the reference instanton to the one with $\omega_0 \propto \sqrt{E_C E_J}$. We shall, of course, be optimizing not the naïve action but the one with $U_f[\phi_\tau]$. By using κ as a variational parameter, allowed to deviate from $\sqrt{E_C E_J}/\Delta$, we will better approximate the new classical action in the presence of fermions, without comprehensively probing the large space of all possible instanton shapes. Calculating the quantity $U_f[\phi^\star_{\kappa\tau}]$ for a range of κ and comparing the minimal value of $S[\phi^\star_{\kappa\tau}] = S_\phi[\phi^\star_{\kappa\tau}] + U_f[\phi^\star_{\kappa\tau}]$ (which includes the kinetic energy $S_\phi[\phi^\star_{\kappa\tau}]$) to the minimal value of $S_n[\phi^\star_{\kappa\tau}]$ will finally give the correction to the tunnelling amplitude. (We also set $N_g = 0$ to make $S_\phi[\phi^\star_{\kappa\tau}]$ real, knowing that the complex winding term $\exp\{[-i\pi N_g w]\}$ is accounted for later.)

From Fig. 3.4, one can observe the key features of $U_f[\phi^\star_{\kappa\tau}]$ and $U_n[\phi^\star_{\kappa\tau}]$ as a function of κ. Taking $\kappa \to \infty$ corresponds to the sharp instanton limit, where $U_n[\phi^\star_{\kappa\tau}] \to 0$ and $U_f[\phi^\star_{\kappa\tau}] > 0$ was evaluated in Sec. 3.4. (We provide another analytical derivation for this limit, using

a different method, in Sec. 3.5.3.) As the arguments in Sec. 3.4 suggested, the difference $U_\mathrm{f}[\phi^\star_{\kappa\tau}] - U_\mathrm{n}[\phi^\star_{\kappa\tau}]$ is largest in this limit. The opposite "adiabatic" limit of $\kappa \to 0$ is most easily understood from Eq. (3.35). From $X^\dagger_{\phi_{\kappa\tau}} \partial_\tau X_{\phi_{\kappa\tau}} = \kappa X^\dagger_{\phi_\tau} \partial_\tau X_{\phi_\tau}$, we see that for $\kappa \to 0$ the last term becomes vanishingly small compared with $\oplus_m \varepsilon^+_{\phi_\tau m} \sigma_3$ as this remains gapped for APBC and OBC, even if the gap is exponentially small in system size for OBC. (We need not worry about the gap closing for PBC because the $k = 0$ eigenstate does not evolve with ϕ.) Therefore, for increasingly slow instantons the fermionic potential tends to the naïve potential: $U_\mathrm{f}[\phi^\star_{\kappa\tau}] \to U_\mathrm{n}[\phi^\star_{\kappa\tau}]$ as $\kappa \to 0$.

Fig. 3.4 also shows that the first order condition $dS[\phi^\star_{\kappa\tau}]/d\kappa = 0$ for minimizing the action yields a similar optimal rescaling factor $\kappa^\star$ whether one uses the fermionic or the naïve potential. Hence, $\sqrt{E_\mathrm{C} E_\mathrm{J}}/\Delta$ remains a good proxy for $\kappa^\star$ in our $\sqrt{E_\mathrm{C} E_\mathrm{J}} \ll \Delta$ regime. Furthermore, since the kinetic term is the same for the fermionic and the naïve case, once the optimal value $\kappa^\star$ is found, the fermionic suppression will approximately be given by $U_\mathrm{f}[\phi^\star_{\kappa^\star\tau}] - U_\mathrm{n}[\phi^\star_{\kappa^\star\tau}]$. Since both $U_\mathrm{f}[\phi^\star_{\kappa^\star\tau}]$ and $U_\mathrm{n}[\phi^\star_{\kappa^\star\tau}]$ are $\propto L$, topology-changing fermions suppress tunnelling exponentially in L.

3.5.3 Evaluating Time-Ordered Exponentials with Scattering Matrices

This translation into scattering matrices was done by Jan Behrends, as was the analytical result for OBC. I separately implemented the scattering matrices numerically.

We now present a method to numerically calculate $U_\mathrm{f}[\phi^\star_{\kappa\tau}]$ for intermediate values of κ and any boundary condition. Recall that to compute the fermionic determinant, we need to evaluate the eigenvalues λ_{nm} via the time-ordered exponential [cf. Eq. (3.31)]

$$\mathsf{M}(\beta, 0) \equiv \exp\left(-\beta \mathcal{H}_\mathrm{eff}[\phi_\tau]\right) = \mathcal{T} \exp\left[-\int_0^\beta d\tau\, \mathcal{H}_{\phi_\tau}\right]. \tag{3.37}$$

The time-ordered exponential can be evaluated numerically by discretizing the integral into N steps

$$\mathsf{M}(\beta, 0) = \lim_{N\to\infty} \mathsf{M}_N \mathsf{M}_{N-1} \ldots \mathsf{M}_1 \tag{3.38}$$

with $\mathsf{M}_n = \exp\left[-(\beta/N)\mathcal{H}_{\phi_{\tau_n}}\right]$ and $\tau_n = \beta(n - 1/2)/N$. Since $\mathsf{M}(\beta, 0)$ has both exponentially large and small eigenvalues [189], the matrix product (3.38) is numerically unstable.

While the matrix product (3.38) itself does not rely on chiral symmetry, our system does have this symmetry. This allows us to interpret each M_n as a transfer matrix that satisfies flux-conservation via $\sigma_1 \mathsf{M}_n^\dagger \sigma_1 = \mathsf{M}_n^{-1}$, which is ensured by the chiral symmetry of $\mathcal{H}_\phi(k) = -\sigma_1 \mathcal{H}_\phi(k) \sigma_1$. This allows us to transform the product of transfer matrices (3.38) into a composition of scattering matrices, whose contraction is numerically more stable [190].

The reformulation of the time-ordered exponential as a scattering problem has the further advantage of simplifying the expressions we are ultimately interested in. For profiles symmetric around $\beta/2$, i.e., $\phi_{\beta/2-\tau} = \phi_{\beta/2+\tau}$, corresponding to an instanton-anti-instanton pair, the transfer matrices $\mathsf{M}(0,\beta/2)$ and $\mathsf{M}(\beta/2,\beta)$ are related via imaginary time reversal, $\mathsf{M}(\beta/2,0) = [\mathsf{M}(\beta,\beta/2)]^\dagger$, which relates their respective scattering matrices $\mathsf{S}(\beta/2,0) = -\sigma_2[\mathsf{S}(\beta,\beta/2)]^\dagger\sigma_2$. A straightforward calculation using the polar decomposition reveals that the transmission eigenvalues of the full scattering matrix are $T_{\text{full},m} = T_m^2/(2-T_m)^2$, where T_m are the transmission eigenvalues of $\mathsf{S}(\beta/2,0)$. The transmission eigenvalues are related to $e^{\pm x_m}$, the eigenvalues of $\mathsf{M}(\beta,0)$ with real x_m, via $T_{\text{full},m} = 1/\cosh^2 x_m$ [189]. Since $\pm x_m/\beta$ are the eigenvalues of the effective Hamiltonian $\mathcal{H}_{\text{eff}}[\phi_\tau]$, the fermionic determinant is thus proportional to the product of all [cf. Eq. (3.33)]

$$\cosh\left(\frac{1}{2}x_m\right) = \cosh\left[\frac{1}{2}\operatorname{arccosh}\left(\frac{2-T_m}{T_m}\right)\right] = \frac{1}{\sqrt{T_m}}, \tag{3.39}$$

i.e., the fermionic determinant for such symmetric configurations is proportional to $1/\det(\mathbf{t})$, where $\mathbf{t}$ is the transmission matrix for *half* of the imaginary time evolution, consisting of *one* instanton.

Analytic Results for Sharp Instantons with OBC

The scattering matrix formalism also allows us to compute the fermionic determinant analytically in the sharp-instanton limit, including for OBC, without explicitly referring to the chiral boundary modes. We first rotate the fermionic Hamiltonian (3.1) $\mathcal{H}_\phi \to \mathcal{H}'_\phi$ via $\sigma_3 \to \sigma_1$, giving

$$\mathcal{H}'_\phi = \begin{pmatrix} & A_\phi \\ A_\phi^\dagger & \end{pmatrix}, \qquad A_\phi(k) = \Delta[\cos^2(\phi/2) - \sin^2(\phi/2)e^{-ik}]. \tag{3.40}$$

Using the singular value decomposition $A_\phi = W_\phi \Sigma_\phi Y_\phi^\dagger$, each transfer matrix for a $\delta\tau$ slice can be brought into its polar form [191, 192], hence each scattering matrix is

$$\mathsf{S} = \begin{pmatrix} -Y_\phi & \\ & W_\phi \end{pmatrix} \begin{pmatrix} -\tanh(\delta\tau\Sigma_\phi) & \operatorname{sech}(\delta\tau\Sigma_\phi) \\ \operatorname{sech}(\delta\tau\Sigma_\phi) & \tanh(\delta\tau\Sigma_\phi) \end{pmatrix} \begin{pmatrix} W_\phi^\dagger & \\ & -Y_\phi^\dagger \end{pmatrix}. \tag{3.41}$$

For a system of size L with OBC each sub-block is an $L\times L$ matrix. At $\phi = 0$, we consider the modified chemical potential $\Delta \to \Delta' = \Delta(1-1/L)$ to ensure that the ground state energies match (cf. Sec. 3.4.1). The singular value decomposition at $\phi = 0$ is trivial ($\Sigma_0 = \Delta'$ with

$W_0 = Y_0 = 1$), and at $\phi = \pi$ yields $W_\pi = -1$, $\Sigma_\pi = \Delta\,\mathrm{diag}(0, 1, \ldots 1)$ and

$$Y_\pi^\dagger = \begin{pmatrix} 0 & & & 1 \\ 1 & 0 & & \\ & \ddots & \ddots & \\ & & 1 & 0 \end{pmatrix}. \tag{3.42}$$

The sharp instanton limit of a symmetric instanton-anti-instanton configuration, where according to Eq. (3.39) one may consider just the instanton, has two scattering matrices: one for imaginary time interval $[0, \beta/4)$ at $\phi = 0$ and another $[\beta/4, \beta/2)$ at $\phi = \pi$. Their contraction [190] gives the lower triangular transmission matrix

$$\mathbf{t} = \frac{1}{\cosh\left(\frac{\beta\Delta'}{4}\right)\cosh\left(\frac{\beta\Delta}{4}\right)} \begin{pmatrix} \cosh(\beta\Delta/4) & & & & \\ y & 1 & & & \\ y^2 & y & 1 & & \\ & \ddots & \ddots & \ddots & \\ y^{L-1} & \ldots & y^2 & y & 1 \end{pmatrix}, \tag{3.43}$$

with $y = \tanh(\beta\Delta/4)\tanh(\beta\Delta'/4)$. Its product of singular values

$$\prod_m \sqrt{T_m} = |\det \mathbf{t}_{\mathrm{tot}}| = \frac{\cosh(\beta\Delta/4)}{[\cosh(\beta\Delta'/4)\cosh(\beta\Delta/4)]^L} \tag{3.44}$$

equals the determinant of the transmission matrix.

The product of singular values is proportional to the square root of the fermionic determinant [Eqs. (3.33) and (3.39)], which gives for the ratio of a two-instanton and zero-instanton configuration in the sharp-instanton limit

$$\sqrt{\frac{\det[\partial_\tau + \mathcal{H}_{2\mathrm{i}}]}{\det[\partial_\tau + \mathcal{H}_{0\mathrm{i}}]}} = \frac{[\cosh(\beta\Delta'/2)]^L}{[\cosh(\beta\Delta'/4)]^L\,[\cosh(\beta\Delta/4)]^{L-1}}, \tag{3.45}$$

and, for $\beta\Delta \gg 1$,

$$\sqrt{\frac{\det[\partial_\tau + \mathcal{H}_{2\mathrm{i}}]}{\det[\partial_\tau + \mathcal{H}_{0\mathrm{i}}]}} = 2^{L-1}\left[1 + O\left(e^{-\left(1-\frac{1}{L}\right)\frac{\beta\Delta}{2}}\right)\right]. \tag{3.46}$$

Therefore, when the instanton separation $\beta/2$ is well beyond the width Δ^{-1} of the instanton-bound fermionic edge mode in the temporal direction (Δ^{-1} is the "temporal coherence length" owing to the temporal velocity equalling unity), the determinant ratio does not depend on the instanton separation. Note that, as in Sec. 3.4.1, this OBC result relies on the matching

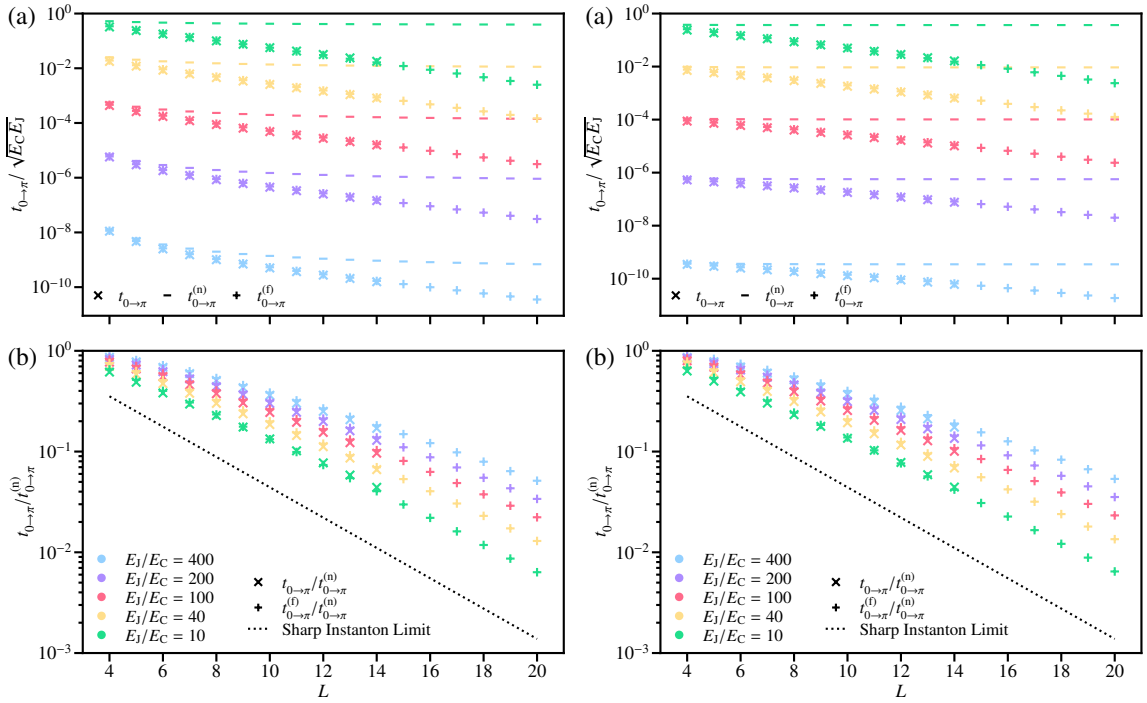

Fig. 3.5 Scaling of the tunnelling amplitude for OBC (left) and APBC (right) systems of size L, plotted on a logarithmic scale for different ratios of E_J/E_C. The effective Josephson energy is defined as $E_J = L\Delta(\pi-2)/4\pi$ for simplicity. (a) The tunnelling amplitude predicted by our instanton-based approach $[t^{(f)}_{0\to\pi}]$ and by the energy splitting obtained from exact diagonalisation $[t_{0\to\pi}]$, in contrast to the naïve approach $[t^{(n)}_{0\to\pi}]$ that takes only the fermionic ground state energy into account. Although plotted up to $L = 20$, the instanton calculation can easily estimate the tunnelling suppression for even larger systems, whereas exact diagonalisation quickly becomes impractical. (b) The ratio of exact and naïve results, compared with our prediction. We also plot the sharp instanton limit results (dotted line), which bound the suppression of the tunnelling amplitude.

ground state energies at $\phi = 0, \pi$; for values of Δ' other than $\Delta(1-1/L)$, the ratio generally grows exponentially with instanton separation. Eq. (3.46) agrees with the result Eq. (3.27) from the boundary-mode approach.

3.5.4 Results

We now calculate the tunnelling suppression due to the topology-changing fermions obtained from our variational approach. To test our results, we will compare with the splitting of the lowest two energies obtained by exact diagonalisation.

As we noted in Secs. 3.2 and 3.3, E_J/E_C and $\sqrt{E_J E_C}/\Delta \propto \omega_0/\Delta$ are two key dimensionless parameters of the problem. The small tunnelling, i.e., semiclassical, limit is $E_J/E_C \gg 1$; this

is also the criterion for instanton methods to be valid (cf. Sec. 3.3.2). Conversely, working in the regime where the fermionic gap near the potential minima is operative (in the sense of ϕ's dynamics) requires $\sqrt{E_J E_C}/\Delta \ll 1$.

Since the scale of the Josephson potential $E_J \approx (V_{\pi/2} - V_0)/2$ grows linearly with L, we require different scaling of E_C depending on which of the key dimensionless parameters we keep fixed in our calculations: one needs $E_C \sim L^{-1}$ (a scaling that can naturally arise in planar Josephson junction systems) to keep ω_0/Δ fixed, while $E_C \sim L$ is required for fixing E_J/E_C.

To assess the performance of our variational calculation, below we focus on fixing the parameter E_J/E_C characterizing the adequacy of the semiclassical limit. In using this parameter, we must bear in mind however, that now $\sqrt{E_J E_C} \sim L$ hence we must keep L finite to remain in the $\omega_0 \ll \Delta$ regime.

In our numerical exact diagonalisation of the full Hamiltonian (3.2), we work in the charge basis. Terms proportional to $\cos\phi$ are off-diagonal in this basis, $e^{i\phi} = \sum_N |N+2\rangle\langle N|$. Owing to the $\sim (N - N_g)^2$ charging term, only a certain number of charge states centred around N_g contribute to the ground state, hence the charge basis can be truncated to N_s states and the low-energy spectrum will still converge to acceptable accuracy. The naïve bosonic problem, where we replace the fermionic Hamiltonian by its ground state energy, is also solved by diagonalizing a Hamiltonian with a truncated basis.

As suggested by the form of the low-energy dispersion $E_\pm(N_g)$ in Eq. (3.9), the desired tunnelling amplitude is observable from the energy splitting when the wells are symmetric [diagnosed by the condition $E_+(1) = E_-(1)$] and is given by

$$t_{0\to\pi} = [E_+(0) - E_-(0)]\,/2. \tag{3.47}$$

However, even after the symmetrisation procedure in Secs. 3.4.1 and 3.5.3, the curvature of the two wells is different. To counter this effect, we add another Josephson potential to ensure that the harmonic-oscillator-like states in both wells would have the same energy were it not for tunnelling.

In Fig. 3.5(a), we show the tunnelling amplitude $t^{(\mathrm{f})}_{0\to\pi}$ based on the instanton calculation and, for small systems up to $L = 14$, the tunnelling amplitude $t_{0\to\pi}$ from the energy splitting that we computed by exact diagonalisation. We compare these results with the naïve tunnelling $t^{(\mathrm{n})}_{0\to\pi}$. While $t^{(\mathrm{n})}_{0\to\pi}/\sqrt{E_J E_C}$ quickly approaches an L-independent value, the tunnelling amplitude $t_{0\to\pi}$ decreases exponentially with L. The instanton-based result $t^{(\mathrm{f})}_{0\to\pi}$ and the exact $t_{0\to\pi}$ almost coincide.

To highlight the suppression by the fermionic contribution, we compare the ratios $t^{(\mathrm{f})}_{0\to\pi}/t^{(\mathrm{n})}_{0\to\pi}$ and $t_{0\to\pi}/t^{(\mathrm{n})}_{0\to\pi}$ in Fig. 3.5(b). The suppression gets weaker with larger E_J/E_C and would eventually approach the naïve result. This can be understood by noting that for fixed

E_J/E_C, and due to $E_J \propto L\Delta$ in our system, we have $\sqrt{E_J E_C}/\Delta \propto L\sqrt{E_C/E_J}$. Therefore, larger E_J/E_C leads to smaller ω_0 which implies larger instanton width, and hence smaller optimal value $\kappa^\star$. The smaller $\kappa^\star$ the more the fermionic and naïve potentials are alike (Fig. 3.4), and, since the fermionic suppression is due to the difference between these two potentials, the closer we are to the naïve result. Conversely, for small E_J/E_C, the tunnelling suppression approaches the upper bound derived from the sharp instanton limit. Upon increasing L, the $\omega_0 \propto L$ dependence, by narrowing instantons and hence increasing $\kappa^\star$, also pushes $t^{(f)}_{0\to\pi}/t^{(n)}_{0\to\pi}$ towards the sharp instanton limit; this leads to a slight downward bend in $t^{(f)}_{0\to\pi}/t^{(n)}_{0\to\pi}$ as a function of L.

While a fuller estimate would require evaluating the fermionic Pfaffian factor beyond classical instanton configurations, we see that using just the classical configuration works remarkably well. One would anticipate more deviation from our prediction in parameter regimes departing from the semiclassical regime $E_J/E_C \gg 1$, where fluctuations in the path integral give a greater contribution to the tunnelling amplitude [114]. For numerically accessible system sizes, an exponential fit to instanton and exact diagonalisation results produces the same fermionic suppression scaling exponent (within the standard error of the fit) for each E_J/E_C series, with only a small offset. This agreement persists across a wide parameter range, but it becomes worse with smaller E_J/E_C ratios as is expected upon gradually departing from the semiclassical regime. While, to maintain $\sqrt{E_J E_C} \lesssim \Delta$ (with $\sqrt{E_J E_C} \approx 0.57\Delta$ for $E_J/E_C = 10$ and $L = 20$), Fig. 3.5 focuses on moderate L, the range considered already emphasises that the instanton calculation allows for the treatment of system sizes well beyond the reach of exact diagonalisation.

3.6 Conclusion

In this Chapter, we studied how coupling to a fermionic bath impacts the tunnel amplitude of a particle, if the tunnelling between potential minima, where the bath is gapped, requires a change in fermionic topology and hence a gap closing. In general, for fermions in d dimensions, we used the field theoretical language of instantons to map this tunnelling problem to that of interfaces between topologically distinct regions in $d+1$ dimensions. This relation, as we elucidated in Sec. 3.4, amounts to stepping up on a dimensional ladder, akin to the reversal of topological insulators' and superconductors' dimensional reduction procedures discussed in Refs. [17, 18, 127, 169]. The existence of topologically protected gapless boundary modes in these $(d+1)$-dimensional geometries leads to a suppression of tunnelling amplitude compared to the value one would naïvely expect by taking the bath at its instantaneous ground state. This suppression is exponential in the size of the fermionic system.

We demonstrated this in detail on our $d = 1$ example, including establishing an analytical bound setting out the strongest possible fermionic suppression. This bound corresponds to sharp instantons, a tractable scenario also applicable to $d > 1$ where it is expected to lead to analogous results: an exponential suppression with L^d, with the exponent set by the boundary modes' density of states.

Complementary to this picture, we also showed how to use instanton field theory to incorporate topology-changing fermions into a variational calculation. This method, which also revealed an unexpected link to scattering matrices that usually arise in quantum transport calculations, allowed us to probe a range between wide instantons (no fermionic suppression) and sharp instantons (maximal fermionic suppression). We compared the tunnelling amplitude obtained from this variational path-integral method with the energy splitting computed by exact diagonalisation of the full many-body system. Our method uses only one variational parameter (the instanton width), and this already yields results that match excellently with exact diagonalisation, while being able to reach much larger systems sizes. In particular, while we demonstrated its use on our $d = 1$ system, the method is equally well applicable to higher dimensions where exact diagonalisation would be limited to exceedingly small systems.

Although we focused on conceptual aspects, our results may be relevant for the planar Josephson systems [100–103] that served as inspiration. As in our $d = 1$ model, the key dimensionless parameters are $E_\mathrm{J}/E_\mathrm{C}$ and $\omega_0/\Delta \sim \sqrt{E_\mathrm{J}E_\mathrm{C}}/\Delta$ with Δ the induced superconducting gap. (Large $E_\mathrm{J}/E_\mathrm{C}$ again corresponds to the semiclassical regime where instanton methods are expected to work, while $\sqrt{E_\mathrm{J}E_\mathrm{C}} \ll \Delta$ renders the fermionic gap operative near the potential minima.) In these systems, the effective Josephson energy $\propto L$ and the charging energy $\propto 1/L$ (being inversely proportional to capacitance). Hence, ω_0/Δ is fixed thus, unlike the fixed $E_\mathrm{J}/E_\mathrm{C}$ case we used for assessing our variational method, the large L regime can be taken consistently with $\omega_0 \ll \Delta$. Although due to $\sqrt{E_\mathrm{J}/E_\mathrm{C}} \propto L$ even the naïve tunnelling amplitude is suppressed exponentially, we stress that the suppression we found enhances the tunnelling exponent. (In other setups, it may be possible to have kinetic and naïve potential terms that do not scale with the size L of the fermionic bath; then one may have an L-independent naïve tunnelling exponent, together with fixed ω_0 and thus a consistent large L limit, and an exponential-in-L suppression solely from fermionic topological effects.)

Since the fermionic ground state energies in trivial and nontrivial regimes are not necessarily equal, the observation of the fermionic suppression of the tunnelling amplitude via the energy splitting may be challenging in these Josephson systems. However, the tunnelling amplitude also impacts non-equilibrium effects which may be more amenable for observation

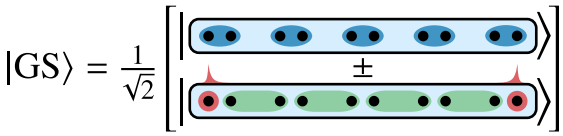

Fig. 3.6 Cartoon of a ground state that is a superposition of two topologically distinct phases. Such a superposition is not blocked on topological grounds in our setup, only suppressed exponentially in the size of the system.

in experiments. In investigating these and other features, studying local versions of our model (obtained by incorporating $\partial_x \phi$) may offer a useful direction for the future.

The fermionic tunnelling suppression we found may be relevant for considering combining topological and transmon qubits, as for example when applying schemes that utilise the charging energy for braiding and parity readout [193–195, 95, 196] to planar Josephson junctions [100, 101]. The tunnelling suppression could also potentially be used to better suppress phase slips (and thus charge noise) in transmon qubits [108, 183].

The fact that tunnelling is only suppressed (but not completely blocked) between topologically distinct minima is also suggestive of the prospects to realise quantum superpositions between topologically distinct fermionic ground states. This is especially intriguing for OBC, where, as in our $d = 1$ model, it can translate to superpositions of fermionic many-body states with and without Majorana end modes, depicted in Figure 3.6. Owing to the exponentially localised nature of these Majorana end states, and to their localisation exponent being unrelated to that of the tunnel suppression, these end states can meaningfully exist in moderate-sized systems where tunnelling between topologically distinct minima can play a considerable role.

Chapter 4

Summary and Outlook

In this thesis, we have explored topological superconductivity in the presence of two extra ingredients: crystalline symmetry and charging energy.

By adding rotational symmetry to 2D superconductors in Chapter 2, we observed MZMs localised at the corners of a sample that, according to the Chern number, should be topologically trivial. Moreover, we were able to predict this *higher-order topology* using bulk quantities, namely the symmetry representations of negative-energy (occupied) states. These irreps form the basis of the wider *symmetry indicator* approach to classifying topological crystalline phases, which provides an efficient—though not exhaustive—mapping of this symmetry-enriched space of topological phases. A consequence of this symmetry indicator abstraction, however, is that the direct link between bulk invariants and the boundary signature is lost. We restored this link by systematically mapping invariants to symmetry properties of stacked Dirac models, which provide the natural low-energy description of most topological phase transitions. With this description, constraints on the boundary theory follow immediately in the form of a symmetry-enforced gap-closing on the surface, which defines our second-order bulk-boundary correspondence. One of our key findings is that this correspondence can crucially depend on which point group symmetry is left unbroken by the termination, which manifested here as an interplay between the weak invariants and the location of the rotation centre.

In Chapter 3, we considered a fermionic topological phase being controlled by a separate variable that is itself subject to quantum fluctuations. The corresponding ingredients are present in the modern planar Josephson junction platform for MZMs, so we chose to frame our discussion in the language of circuit QED, where the control variable is the Josephson phase difference ϕ, whose fluctuations arise from charging energy. Fermions act as a bath for ϕ, whose tunneling amplitude is exponentially suppressed by the fermions' topology change. We were able to accurately quantify this tunneling thanks to the powerful field-theoretic

method of instantons, which we adapted to include and later integrate out a lattice of fermions. The central difficulty was evaluating the resulting temporally-nonlocal effective action, though we could bound the suppression from above through an analogy to the low-energy spectrum of a topological superconductor in one dimension higher; there, we found the suppression exponent to be linear in the number of fermions comprising the bath. This result agreed with a numerically efficient novel time-ordered exponential calculation, which we could verify for modest system sizes using exact diagonalisation.

This thesis brings to light many possible directions for future research. The most obvious open question that follows from Chapter 2 is whether our stacked Dirac construction can give the higher-order bulk boundary correspondence for other crystalline symmetry groups. If symmetry indicators can be combined with other topological invariants to fully classify the bulk, then the generality of stacked Dirac models would make it a promising candidate to bridge between the bulk and boundary classification groups.[1] However, we also saw a sixfold rotation symmetry representation that could be furnished only by a *cubic* Dirac model, so this approach would be strengthened by a separate analytical study into the boundary theory of this $\Delta\mathrm{Ch} = \pm 3$ two-band model. Luckily, we were able to avoid these nonlinearly-dispersing Dirac models by choosing substitutes from the same stable equivalence class, and this strategy may also work in other symmetry classes. Nevertheless, being able to directly treat these cases without relying on stability would be advantageous, especially for potential links to fragile topology [42], which is yet to be fully defined for superconductors.

Our results from adding crystalline symmetry also prompt us to reflect on what symmetries are reasonable to impose on a system. In the bulk, crystalline symmetries are enforced by the comparatively large electrostatic energy cost of moving ions away from thermodynamically stable configurations, generating symmetric potentials for the electrons. On the boundary, those electrostatic forces are very different and the symmetry constraints on the ions would not be expected to be as rigid. Yet, our present conclusions about the boundary signature assumed a nonlocal point group symmetry that applied globally across the boundary; indeed, some features relied on the precise boundary symmetry, as exemplified in Sec. 2.6 where the choice of rotation centre was critical. Nevertheless, one still expects MZMs at the corners of a fully symmetric crystalline system to be robust against disorder that does not close the boundary gap or bring corners together. This suggests a stability under local perturbations away from the symmetric limit. A practically relevant question is what higher-order bulk boundary correspondence survives when the spatial symmetry is only respected on average (especially on the boundary), or when the system is *polycrystalline* with multiple misaligned

[1] Recall that on their own, symmetry indicators give only a *proxy* to the boundary classification group, as seen from Eq. (1.34).

grains of moderate size. A similar question is being pursued in the more extreme case of amorphous topological insulators [197, 198, 137], sometimes using a generalisation of the Chern number to a real space topological marker [199, 200]. In the intermediate case, crystalline symmetry would be loosely retained so one could take advantage of the recent real space formulation of symmetry indicators [146] to investigate disorder. Disorder was investigated for weak topological phases [201, 202] (the forerunner to topological crystalline phases) where, as for strong topological phases, surface states did not Anderson-localise, so long as the disorder respected translation-symmetry on average. Developing our approach to the higher-order bulk-boundary correspondence in this case would be an interesting direction for future research.

Coupling a bosonic quantum variable to a system of fermions is also a general scenario that could arise in other condensed matter tunneling problems. We showed that adding fermions always suppresses the tunneling compared to a naive potential because of the fermionic part of the wavefunction. While this effect is most drastic when the fermions undergo a bulk gap closing, our instanton technique can quantify the transition from adiabaticity to a sharp inner product between two distinct fermionic wavefunctions. This type of tunneling calculation could be relevant for mesoscale quantum phase transitions. Such transitions may not be that far out of experimental reach: for example, the entanglement between many fermions recently observed in ferromagnets [203] has some parallels to the type of superposition we proposed in Chapter 3. In transmon qubits, the suppression of tunneling due to fermions also provides a separate mechanism to reduce charge noise without compromising anharmonicity. It would also be interesting to explore the consequences of finite temperature on these tunneling effects.

Chapter 3 has demonstrated how the consequences of single-particle topology are still felt even when adding interactions. This shows that other fruitful directions open up from adding interactions to free-fermion topological systems separate from constructing the interacting SPT classification. [Indeed, in our case the non-locality of the charging term $(\hat{N} - N_g)^2$ means it cannot neatly fit into an SPT classification.] The controllability of charging energy in particular allows interacting systems to be engineered that build on the properties of the underlying non-interacting topological superconducting phase. This principle is already on display in 2D second-order topological superconductors where local parity constraints (implementable through charging energy) can create topological ordered stabiliser codes [97] that rely on the degeneracy from corner MZMs.

References

[1] B. Zeng, X. Chen, D.-L. Zhou, X.-G. Wen, *et al.*, *Quantum Information Meets Quantum Matter* (Springer, 2019).

[2] J. Eisert, M. Cramer, and M. B. Plenio, Rev. Mod. Phys. **82**, 277 (2010).

[3] X. Chen, Z.-C. Gu, and X.-G. Wen, Phys. Rev. B **82**, 155138 (2010).

[4] X.-G. Wen, Rev. Mod. Phys. **89**, 041004 (2017).

[5] X.-G. Wen, Phys. Rev. Lett. **90**, 016803 (2003).

[6] T. Hansson, V. Oganesyan, and S. Sondhi, Annals of Physics **313**, 497 (2004).

[7] K. v. Klitzing, G. Dorda, and M. Pepper, Phys. Rev. Lett. **45**, 494 (1980).

[8] D. J. Thouless, M. Kohmoto, M. P. Nightingale, and M. den Nijs, Phys. Rev. Lett. **49**, 405 (1982).

[9] L. Fu, C. L. Kane, and E. J. Mele, Phys. Rev. Lett. **98**, 106803 (2007).

[10] C.-K. Chiu, J. C. Y. Teo, A. P. Schnyder, and S. Ryu, Rev. Mod. Phys. **88**, 035005 (2015).

[11] R. Roy, Phys. Rev. B **79**, 195322 (2009).

[12] M. Z. Hasan and C. L. Kane, Rev. Mod. Phys. **82**, 3045 (2010).

[13] J. E. Moore and L. Balents, Phys. Rev. B **75**, 121306 (2007).

[14] A. Altland and M. R. Zirnbauer, Phys. Rev. B **55**, 1142 (1997).

[15] X.-L. Qi, T. L. Hughes, and S.-C. Zhang, Phys. Rev. B **78**, 195424 (2008).

[16] A. P. Schnyder, S. Ryu, A. Furusaki, and A. W. W. Ludwig, Phys. Rev. B **78**, 195125 (2008).

[17] A. Kitaev, AIP Conf. Proc. **1134**, 22 (2009).

[18] S. Ryu, A. P. Schnyder, A. Furusaki, and A. W. W. Ludwig, New J. Phys. **12**, 065010 (2010).

[19] J. Bardeen, L. N. Cooper, and J. R. Schrieffer, Phys. Rev. **108**, 1175 (1957).

[20] S. Bravyi and D. Gosset, Commun. Math. Phys. **356**, 451 (2017).

[21] D. C. Youla, Can. J. Math. **13**, 694–704 (1961).

[22] E. Majorana, Il Nuovo Cimento (1924-1942) **14**, 171 (1937).

[23] J. Alicea, Rep. Prog. Phys. **75**, 076501 (2012).

[24] C. Beenakker, Annu. Rev. Condens. Matter Phys. **4**, 113 (2013).

[25] A. Y. Kitaev, Physics-Uspekhi **44**, 131 (2001).

[26] A. Kitaev, Ann. Phys. (N. Y). **303**, 2 (2003).

[27] C. Nayak, S. H. Simon, A. Stern, M. Freedman, and S. Das Sarma, Rev. Mod. Phys. **80**, 1083 (2008).

[28] E. Gibney, Nature (2016), 10.1038/nature.2016.20774.

[29] J. C. Budich and E. Ardonne, Phys. Rev. B **88**, 075419 (2013).

[30] N. Read and D. Green, Phys. Rev. B **61**, 10267 (2000).

[31] R. Jackiw and C. Rebbi, Phys. Rev. D **13**, 3398 (1976).

[32] V. Gurarie and L. Radzihovsky, Phys. Rev. B **75**, 212509 (2007).

[33] R.-J. Slager, A. Mesaros, V. Juričić, and J. Zaanen, Nat. Phys. **9**, 98 (2013).

[34] K. Shiozaki and M. Sato, Phys. Rev. B **90**, 165114 (2014).

[35] K. Shiozaki, M. Sato, and K. Gomi, Phys. Rev. B **93**, 195413 (2016).

[36] L. Fu and C. L. Kane, Phys. Rev. B **76**, 045302 (2007).

[37] E. Khalaf, H. C. Po, A. Vishwanath, and H. Watanabe, Phys. Rev. X **8**, 031070 (2018).

[38] J. Kruthoff, J. de Boer, J. van Wezel, C. L. Kane, and R.-J. Slager, Phys. Rev. X **7**, 041069 (2016).

[39] E. Cornfeld and S. Carmeli, Phys. Rev. Research **3**, 013052 (2021).

[40] K. Shiozaki, M. Sato, and K. Gomi, Phys. Rev. B **106**, 165103 (2022).

[41] H. C. Po, Journal of Physics: Condensed Matter **32**, 263001 (2020).

[42] H. C. Po, H. Watanabe, and A. Vishwanath, Phys. Rev. Lett. **121**, 126402 (2018).

[43] J. E. Moore, Y. Ran, and X.-G. Wen, Phys. Rev. Lett. **101**, 186805 (2008).

[44] Z.-D. Song, L. Elcoro, and B. A. Bernevig, Science **367**, 794 (2020).

[45] J. C. Y. Teo, L. Fu, and C. L. Kane, Phys. Rev. B **78**, 045426 (2008).

[46] M. Geier, L. Trifunovic, M. Hoskam, and P. W. Brouwer, Phys. Rev. B **97**, 205135 (2018).

[47] B. Bradlyn, L. Elcoro, J. Cano, M. G. Vergniory, Z. Wang, C. Felser, M. I. Aroyo, and B. A. Bernevig, Nature **547**, 298 (2017).

[48] H. C. Po, A. Vishwanath, and H. Watanabe, Nat. Commun. **8**, 50 (2017).

[49] M. Geier, P. W. Brouwer, and L. Trifunovic, Phys. Rev. B **101**, 245128 (2020).

[50] C. Fang, B. A. Bernevig, and M. J. Gilbert, arXiv:1701.01944 [cond-mat] (2017).

[51] J. Cano, B. Bradlyn, Z. Wang, L. Elcoro, M. G. Vergniory, C. Felser, M. I. Aroyo, and B. A. Bernevig, Phys. Rev. B **97**, 035139 (2018).

[52] S. Ono, H. C. Po, and H. Watanabe, Science Advances **6**, eaaz8367 (2020).

[53] F. Tang, H. C. Po, A. Vishwanath, and X. Wan, Nature Physics **15**, 470 (2019).

[54] M. G. Vergniory, L. Elcoro, C. Felser, N. Regnault, B. A. Bernevig, and Z. Wang, Nature **566**, 480 (2019).

[55] T. Zhang, Y. Jiang, Z. Song, H. Huang, Y. He, Z. Fang, H. Weng, and C. Fang, Nature **566**, 475 (2019).

[56] W. A. Benalcazar, J. C. Teo, and T. L. Hughes, Phys. Rev. B **89**, 224503 (2014).

[57] S. Ono and H. Watanabe, Phys. Rev. B **98**, 115150 (2018).

[58] S. Ono, Y. Yanase, and H. Watanabe, Phys. Rev. Research **1**, 013012 (2019).

[59] A. Skurativska, T. Neupert, and M. H. Fischer, Phys. Rev. Research **2**, 013064 (2020).

[60] F. Schindler, B. Bradlyn, M. H. Fischer, and T. Neupert, Phys. Rev. Lett. **124**, 247001 (2020).

[61] E. Khalaf, Phys. Rev. B **97**, 205136 (2018).

[62] J. C. Y. Teo and C. L. Kane, Phys. Rev. B **82**, 115120 (2010).

[63] M. Sitte, A. Rosch, E. Altman, and L. Fritz, Phys. Rev. Lett. **108**, 126807 (2012).

[64] F. Zhang, C. L. Kane, and E. J. Mele, Phys. Rev. Lett. **110**, 046404 (2013).

[65] F. Schindler, A. M. Cook, M. G. Vergniory, Z. Wang, S. S. P. Parkin, B. A. Bernevig, and T. Neupert, Sci. Adv. **4**, eaat0346 (2018).

[66] Z. Song, Z. Fang, and C. Fang, Phys. Rev. Lett. **119**, 246402 (2017).

[67] W. A. Benalcazar, B. A. Bernevig, and T. L. Hughes, Phys. Rev. B **96**, 245115 (2017).

[68] W. A. Benalcazar, B. A. Bernevig, and T. L. Hughes, Science **357**, 61 (2017).

[69] J. Langbehn, Y. Peng, L. Trifunovic, F. Von Oppen, and P. W. Brouwer, Phys. Rev. Lett. **119**, 246401 (2017).

[70] R. D. King-Smith and D. Vanderbilt, Phys. Rev. B **47**, 1651 (1993).

[71] W. A. Benalcazar, T. Li, and T. L. Hughes, Phys. Rev. B **99**, 245151 (2019).

[72] S. Ghosh, A. Shekhter, F. Jerzembeck, N. Kikugawa, D. A. Sokolov, M. Brando, A. P. Mackenzie, C. W. Hicks, and B. J. Ramshaw, Nature Physics **17**, 199 (2021).

[73] S. Benhabib, C. Lupien, I. Paul, L. Berges, M. Dion, M. Nardone, A. Zitouni, Z. Q. Mao, Y. Maeno, A. Georges, L. Taillefer, and C. Proust, Nature Physics **17**, 194 (2021).

[74] S. Acharya, D. Pashov, C. Weber, H. Park, L. Sponza, and M. V. Schilfgaarde, Commun. Phys. **2**, 163 (2019).

[75] R. M. Lutchyn, J. D. Sau, and S. Das Sarma, Phys. Rev. Lett. **105**, 077001 (2010).

[76] Y. Oreg, G. Refael, and F. von Oppen, Phys. Rev. Lett. **105**, 177002 (2010).

[77] V. Mourik, K. Zuo, S. M. Frolov, S. R. Plissard, E. P. A. M. Bakkers, and L. P. Kouwenhoven, Science **336**, 1003 (2012).

[78] S. Vaitiekėnas, G. Winkler, B. van Heck, T. Karzig, M.-T. Deng, K. Flensberg, L. Glazman, C. Nayak, P. Krogstrup, R. Lutchyn, *et al.*, Science **367** (2020).

[79] H. Zhang, C.-X. Liu, S. Gazibegovic, D. Xu, J. A. Logan, G. Wang, N. Van Loo, J. D. Bommer, M. W. De Moor, D. Car, *et al.*, Nature **556**, 74 (2018).

[80] H. Zhang, C.-X. Liu, S. Gazibegovic, D. Xu, J. A. Logan, G. Wang, N. van Loo, J. D. Bommer, M. W. de Moor, D. Car, *et al.*, Nature **591**, E30 (2021).

[81] J. C. Budich, S. Walter, and B. Trauzettel, Phys. Rev. B **85**, 121405 (2012).

[82] P. Bonderson and C. Nayak, Phys. Rev. B **87**, 195451 (2013).

[83] K. T. Law, P. A. Lee, and T. K. Ng, Phys. Rev. Lett. **103**, 237001 (2009).

[84] K. Flensberg, Phys. Rev. B **82**, 180516 (2010).

[85] A. Vuik, B. Nijholt, A. R. Akhmerov, and M. Wimmer, SciPost Physics **7**, 061 (2019).

[86] G. Kells, D. Meidan, and P. W. Brouwer, Phys. Rev. B **86**, 100503 (2012).

[87] C. Moore, C. Zeng, T. D. Stanescu, and S. Tewari, Phys. Rev. B **98**, 155314 (2018).

[88] A. R. Akhmerov, J. P. Dahlhaus, F. Hassler, M. Wimmer, and C. W. J. Beenakker, Phys. Rev. Lett. **106**, 057001 (2011).

[89] B. M. Fregoso, A. M. Lobos, and S. Das Sarma, Phys. Rev. B **88**, 180507 (2013).

[90] P. Szumniak, D. Chevallier, D. Loss, and J. Klinovaja, Phys. Rev. B **96**, 041401 (2017).

[91] B. Béri and N. R. Cooper, Phys. Rev. Lett. **109**, 156803 (2012).

[92] J. Manousakis, C. Wille, A. Altland, R. Egger, K. Flensberg, and F. Hassler, Phys. Rev. Lett. **124**, 096801 (2020).

[93] Y. Oreg and F. von Oppen, Annu. Rev. Condens. Matter Phys. **11**, 397 (2020).

[94] T. Karzig, C. Knapp, R. M. Lutchyn, P. Bonderson, M. B. Hastings, C. Nayak, J. Alicea, K. Flensberg, S. Plugge, Y. Oreg, C. M. Marcus, and M. H. Freedman, Phys. Rev. B **95**, 235305 (2017).

[95] B. van Heck, A. R. Akhmerov, F. Hassler, M. Burrello, and C. W. J. Beenakker, New J. Phys. **14**, 035019 (2012).

[96] D. Aasen, M. Hell, R. V. Mishmash, A. Higginbotham, J. Danon, M. Leijnse, T. S. Jespersen, J. A. Folk, C. M. Marcus, K. Flensberg, and J. Alicea, Phys. Rev. X **6**, 031016 (2016).

[97] Y. You, D. Litinski, and F. von Oppen, Phys. Rev. B **100**, 054513 (2019).

[98] S. M. Girvin, in *Quantum Machines: Measurement and Control of Engineered Quantum Systems: Lecture Notes of the Les Houches Summer School: Volume 96, July 2011* (Oxford University Press, 2014).

[99] F. Arute, K. Arya, R. Babbush, D. Bacon, J. C. Bardin, R. Barends, R. Biswas, S. Boixo, F. G. S. L. Brandão, D. A. Buell, *et al.*, Nature **574**, 505 (2019).

[100] F. Pientka, A. Keselman, E. Berg, A. Yacoby, A. Stern, and B. I. Halperin, Phys. Rev. X **7**, 021032 (2017).

[101] M. Hell, M. Leijnse, and K. Flensberg, Phys. Rev. Lett. **118**, 107701 (2017).

[102] A. Fornieri, A. M. Whiticar, F. Setiawan, E. Portolés, A. C. C. Drachmann, A. Keselman, S. Gronin, C. Thomas, T. Wang, R. Kallaher, G. C. Gardner, E. Berg, M. J. Manfra, A. Stern, C. M. Marcus, and F. Nichele, Nature **569**, 89 (2019).

[103] H. Ren, F. Pientka, S. Hart, A. T. Pierce, M. Kosowsky, L. Lunczer, R. Schlereth, B. Scharf, E. M. Hankiewicz, L. W. Molenkamp, B. I. Halperin, and A. Yacoby, Nature **569**, 93 (2019).

[104] A. Blais, A. L. Grimsmo, S. M. Girvin, and A. Wallraff, Rev. Mod. Phys. **93**, 025005 (2021).

[105] U. Vool and M. Devoret, Int. J. Circuit Theory Appl. **45**, 897 (2017).

[106] B. D. Josephson, Physics Letters **1**, 251 (1962).

[107] M. Tinkham, *Introduction to Superconductivity: Second Edition*, Dover Books on Physics (Dover Publications, Mineola, NY, 2004).

[108] J. Koch, T. M. Yu, J. Gambetta, A. A. Houck, D. I. Schuster, J. Majer, A. Blais, M. H. Devoret, S. M. Girvin, and R. J. Schoelkopf, Phys. Rev. A **76**, 042319 (2007).

[109] S. Coleman, *Aspects of Symmetry: Selected Erice Lectures* (Cambridge University Press, Cambridge, 1985).

[110] R. Rajaraman, *Solitons and Instantons: An Introduction to Solitons and Instantons in Quantum Field Theory* (North-Holland, Amsterdam; Oxford, 1982).

[111] T. Schäfer and E. V. Shuryak, Rev. Mod. Phys. **70**, 323 (1998).

[112] H. Forkel, "A Primer on Instantons in QCD," (2002), arXiv:hep-ph/0009136.

[113] L. Fu and C. L. Kane, Phys. Rev. B **79**, 161408 (2009).

[114] A. Altland and B. D. Simons, *Condensed Matter Field Theory*, 2nd ed. (Cambridge University Press, Cambridge, 2010).

[115] H. Kleinert, *Path Integrals in Quantum Mechanics, Statistics, Polymer Physics, and Financial Markets* (World Scientific, 2009).

[116] R. Rodríguez-Mota, S. Vishveshwara, and T. Pereg-Barnea, Phys. Rev. B **99**, 024517 (2019).

[117] S. Ryu, J. E. Moore, and A. W. Ludwig, Phys. Rev. B **85**, 045104 (2012).

[118] L. Fu, Phys. Rev. Lett. **106**, 106802 (2011).

[119] A. Alexandradinata, C. Fang, M. J. Gilbert, and B. A. Bernevig, Phys. Rev. Lett. **113**, 116403 (2014).

[120] T. Morimoto and A. Furusaki, Phys. Rev. B **88**, 125129 (2013).

[121] J. C. Y. Teo and T. L. Hughes, Phys. Rev. Lett. **111**, 047006 (2013).

[122] X.-J. Liu, J. J. He, and K. T. Law, Phys. Rev. B **90**, 235141 (2014).

[123] C. Fang, M. J. Gilbert, and B. A. Bernevig, Phys. Rev. B **86**, 115112 (2012).

[124] C. Fang, M. J. Gilbert, and B. A. Bernevig, Phys. Rev. B **87**, 035119 (2013).

[125] Y. Hatsugai, Phys. Rev. Lett. **71**, 3697 (1993).

[126] M. Z. Hasan and C. L. Kane, Rev. Mod. Phys. **82**, 3045 (2010).

[127] X.-L. Qi and S.-C. Zhang, Rev. Mod. Phys. **83**, 1057 (2011).

[128] F. K. Kunst, G. van Miert, and E. J. Bergholtz, Phys. Rev. B **97**, 241405 (2018).

[129] L. Trifunovic and P. W. Brouwer, Phys. Rev. X **9**, 11012 (2019).

[130] G. Van Miert and C. Ortix, Phys. Rev. B **98**, 081110 (2018).

[131] N. Bultinck, B. A. Bernevig, and M. P. Zaletel, Phys. Rev. B **99**, 125149 (2019).

[132] F. Schindler, Z. Wang, M. G. Vergniory, A. M. Cook, A. Murani, S. Sengupta, A. Y. Kasumov, R. Deblock, S. Jeon, I. Drozdov, H. Bouchiat, S. Guéron, A. Yazdani, B. A. Bernevig, and T. Neupert, Nat. Phys. **14**, 918 (2018).

[133] V. Dwivedi, C. Hickey, T. Eschmann, and S. Trebst, Phys. Rev. B **98**, 054432 (2018).

[134] M. Rodriguez-Vega, A. Kumar, and B. Seradjeh, Phys. Rev. B **100**, 085138 (2019).

[135] S. Chaudhary, A. Haim, Y. Peng, and G. Refael, Phys. Rev. Research **2**, 043431 (2020).

[136] S. A. A. Ghorashi, X. Hu, T. L. Hughes, and E. Rossi, Phys. Rev. B **100**, 020509 (2019).

[137] A. Agarwala, V. Juričić, and B. Roy, Phys. Rev. Research **2**, 012067 (2020).

[138] D. Varjas, A. Lau, K. Pöyhönen, A. R. Akhmerov, D. I. Pikulin, and I. C. Fulga, Phys. Rev. Lett. **123**, 196401 (2019).

[139] R. Chen, C.-Z. Chen, J.-H. Gao, B. Zhou, and D.-H. Xu, Phys. Rev. Lett. **124**, 036803 (2020).

[140] M. Serra-Garcia, V. Peri, R. Süsstrunk, O. R. Bilal, T. Larsen, L. G. Villanueva, and S. D. Huber, Nature **555**, 342 (2018).

[141] S. N. Kempkes, M. R. Slot, J. J. van den Broeke, P. Capiod, W. A. Benalcazar, D. Vanmaekelbergh, D. Bercioux, I. Swart, and C. Morais Smith, Nat. Mater. **18**, 1292 (2019).

[142] S. Imhof, C. Berger, F. Bayer, J. Brehm, L. W. Molenkamp, T. Kiessling, F. Schindler, C. H. Lee, M. Greiter, T. Neupert, and R. Thomale, Nat. Phys. **14**, 925 (2018).

[143] C. W. Peterson, W. A. Benalcazar, T. L. Hughes, and G. Bahl, Nature **555**, 346 (2018).

[144] F. Schindler, M. Brzezińska, W. A. Benalcazar, M. Iraola, A. Bouhon, S. S. Tsirkin, M. G. Vergniory, and T. Neupert, Phys. Rev. Research **1**, 033074 (2019).

[145] K. Shiozaki, arXiv:1907.13632 [cond-mat] (2019).

[146] I. Mondragon-Shem and T. L. Hughes, arXiv:1906.11847 [cond-mat] (2019).

[147] A. Alexandradinata, X. Dai, and B. A. Bernevig, Phys. Rev. B **89**, 155114 (2014).

[148] A. Alexandradinata, Z. Wang, and B. A. Bernevig, Phys. Rev. X **6**, 021008 (2016).

[149] W. P. Su, J. R. Schrieffer, and A. J. Heeger, Phys. Rev. Lett. **42**, 1698 (1979).

[150] C. Fang and L. Fu, Sci. Adv. **5**, eaat2374 (2019).

[151] L. Fu and C. L. Kane, Phys. Rev. Lett. **100**, 096407 (2008).

[152] D. Călugăru, V. Juričić, and B. Roy, Phys. Rev. B **99**, 041301 (2019).

[153] A. O. Caldeira and A. J. Leggett, Phys. Rev. Lett. **46**, 211 (1981).

[154] A. Caldeira and A. Leggett, Ann. Phys. (N. Y). **149**, 374 (1983).

[155] H. Grabert, U. Weiss, and P. Hanggi, Phys. Rev. Lett. **52**, 2193 (1984).

[156] A. T. Dorsey, M. P. A. Fisher, and M. S. Wartak, Phys. Rev. A **33**, 1117 (1986).

[157] A. J. Leggett, S. Chakravarty, A. T. Dorsey, M. P. A. Fisher, A. Garg, and W. Zwerger, Rev. Mod. Phys. **59**, 1 (1987).

[158] V. Ambegaokar, U. Eckern, and G. Schön, Phys. Rev. Lett. **48**, 1745 (1982).

[159] A. I. Larkin and Y. N. Ovchinnikov, Phys. Rev. B **28**, 6281 (1983).

[160] Y. Makhlin, G. Schön, and A. Shnirman, Rev. Mod. Phys. **73**, 357 (2001).

[161] A. Kampf and G. Schön, Phys. B Condens. Matter **152**, 239 (1988).

[162] G. Schön and A. Zaikin, Phys. Rep. **198**, 237 (1990).

[163] D. M. Badiane, L. I. Glazman, M. Houzet, and J. S. Meyer, Comptes Rendus Phys. **14**, 840 (2013).

[164] D. V. Averin, Phys. Rev. Lett. **82**, 3685 (1999).

[165] A. Bargerbos, W. Uilhoorn, C.-K. Yang, P. Krogstrup, L. P. Kouwenhoven, G. de Lange, B. van Heck, and A. Kou, Phys. Rev. Lett. **124**, 246802 (2020).

[166] H.-J. Kwon, K. Sengupta, and V. M. Yakovenko, Eur. Phys. J. B - Condens. Matter **37**, 349 (2004).

[167] B. van Heck, F. Hassler, A. R. Akhmerov, and C. W. J. Beenakker, Phys. Rev. B **84**, 180502 (2011).

[168] D. Pekker, C.-Y. Hou, D. L. Bergman, S. Goldberg, I. Adagideli, and F. Hassler, Phys. Rev. B **87**, 064506 (2013).

[169] B. A. Bernevig and T. L. Hughes, *Topological Insulators and Topological Superconductors* (Princeton University Press, Princeton, NJ, 2013).

[170] J. K. Asbóth, L. Oroszlány, and A. Pályi, *A Short Course on Topological Insulators*, Lecture Notes in Physics, Vol. 919 (Springer, Basel, Switzerland, 2016).

[171] A. Belavin, A. Polyakov, A. Schwartz, and Y. Tyupkin, Phys. Lett. B **59**, 85 (1975).

[172] C. Callan, R. Dashen, and D. Gross, Phys. Lett. B **63**, 334 (1976).

[173] Y. V. Nazarov and Y. M. Blanter, *Quantum Transport: Introduction to Nanoscience* (Cambridge University Press, Cambridge, U.K., 2009).

[174] P. W. Anderson, in *Lectures on the Many-body Problems*, edited by E. R. Caianiello (Elsevier, Cambridge, M.A., 1964) pp. 113–135.

[175] Y. N. Ovchinnikov, A. Barone, and A. A. Varlamov, Phys. Rev. Lett. **99**, 037004 (2007).

[176] Y. N. Ovchinnikov, A. Barone, and A. A. Varlamov, Phys. Rev. B **78**, 054521 (2008).

[177] A. Stern and E. Berg, Phys. Rev. Lett. **122**, 107701 (2019).

[178] B. Douçot and J. Vidal, Phys. Rev. Lett. **88**, 227005 (2002).

[179] L. B. Ioffe and M. V. Feigel'man, Phys. Rev. B **66**, 224503 (2002).

[180] N. W. Ashcroft and N. D. Mermin, *Solid State Physics* (Brooks/Cole, 1976).

[181] E. M. Harrell, Commun. Math. Phys. **75**, 239 (1980).

[182] M. Arzamasovs and B. Liu, Eur. J. Phys. **38**, 065405 (2017).

[183] J. A. Schreier, A. A. Houck, J. Koch, D. I. Schuster, B. R. Johnson, J. M. Chow, J. M. Gambetta, J. Majer, L. Frunzio, M. H. Devoret, S. M. Girvin, and R. J. Schoelkopf, Phys. Rev. B **77**, 180502 (2008).

[184] J. Zinn-Justin, *Quantum Field Theory and Critical Phenomena*, 4th ed. (Oxford University Press, Oxford, 2002) p. 1074.

[185] B. de Wit and J. Smith, *Field Theory in Particle Physics*, N H Personal Library, Vol 1 (North-Holland, Amsterdam, 1986).

[186] A. P. Schnyder, S. Ryu, A. Furusaki, and A. W. W. Ludwig, Phys. Rev. B **78**, 195125 (2008).

[187] F. Charmchi and S. Gousheh, Phys. Rev. D **89**, 025002 (2014).

[188] R. F. Dashen, B. Hasslacher, and A. Neveu, Phys. Rev. D **12**, 2443 (1975).

[189] C. W. J. Beenakker, Rev. Mod. Phys. **69**, 731 (1997).

[190] H. Tamura and T. Ando, Phys. Rev. B **44**, 1792 (1991).

[191] P. A. Mello, P. Pereyra, and N. Kumar, Ann. Phys. (N. Y). **181**, 290 (1988).

[192] T. Martin and R. Landauer, Phys. Rev. B **45**, 1742 (1992).

[193] L. Jiang, C. L. Kane, and J. Preskill, Phys. Rev. Lett. **106**, 130504 (2011).

[194] P. Bonderson and R. M. Lutchyn, Phys. Rev. Lett. **106**, 130505 (2011).

[195] F. Hassler, A. R. Akhmerov, and C. W. J. Beenakker, New J. Phys. **13**, 095004 (2011).

[196] T. Hyart, B. van Heck, I. C. Fulga, M. Burrello, A. R. Akhmerov, and C. W. J. Beenakker, Phys. Rev. B **88**, 035121 (2013).

[197] N. P. Mitchell, L. Nash, D. Hexner, A. M. Turner, and W. T. Irvine, Nature Physics **14**, 380 (2016).

[198] A. Agarwala and V. B. Shenoy, Phys. Rev. Lett. **118**, 236402 (2017).

[199] E. Prodan, New J. Phys. **12**, 065003 (2010).

[200] R. Bianco and R. Resta, Phys. Rev. B **84**, 241106 (2011).

[201] Z. Ringel, Y. E. Kraus, and A. Stern, Phys. Rev. B **86**, 045102 (2012).

[202] I. C. Fulga, B. van Heck, J. M. Edge, and A. R. Akhmerov, Phys. Rev. B **89**, 155424 (2014).

[203] A. Wendl, H. Eisenlohr, F. Rucker, C. Duvinage, M. Kleinhans, M. Vojta, and C. Pfleiderer, Nature **609 7925**, 65 (2022).

[204] C. M. Goringe, D. R. Bowler, and E. Hernández, Reports Prog. Phys. **60**, 1447 (1997).

[205] E. Khalaf, W. A. Benalcazar, T. L. Hughes, and R. Queiroz, Phys. Rev. Research **3**, 013239 (2021).

[206] F. Charmchi and S. Gousheh, Nucl. Phys. B **883**, 256 (2014).

[207] S. Jana, A. Saha, and S. Das, Phys. Rev. B **100**, 085428 (2019).

Appendix A

Additional Derivations for Bulk-Boundary Correspondence

A.1 Restrictions on Choice of Unit Cell

The bulk classification of Ref. [56] of rotationally symmetric superconductors employed in the main text relies on having momentum-independent matrices r_n that rotate the momentum-space tight-binding Hamiltonian, cf. Eq. (2.2). Generally, the form of the tight-binding Hamiltonian depends on the choice of the basis functions. In particular, using orbitals $\varphi_{\mathbf{R},\alpha}(\mathbf{r}-\mathbf{R}-\mathbf{d}_\alpha)$ for each orbital α at the position $\mathbf{R}+\mathbf{d}_\alpha$ with the Bravais lattice vector $\mathbf{R}$ and atomic position $\mathbf{d}_\alpha$ enables us to construct basis functions [204, 148]

$$\bar{\phi}_{\mathbf{k},\alpha}(\mathbf{r}) = \frac{1}{\sqrt{N}} \sum_{\mathbf{R}} e^{-i\mathbf{k}\cdot(\mathbf{R}+\mathbf{d}_\alpha)} \varphi_{\mathbf{R},\alpha}(\mathbf{r}-\mathbf{R}-\mathbf{d}_\alpha) \tag{A.1}$$

where the sum goes over all N unit cells at positions $\mathbf{R}$. The resulting tight-binding Hamiltonian

$$\bar{H}_{\alpha\beta}(\mathbf{k}) = \int d^2\mathbf{r}\, \bar{\phi}^*_{\mathbf{k},\alpha}(\mathbf{r}) \hat{H} \bar{\phi}_{\mathbf{k},\beta}(\mathbf{r}) \tag{A.2}$$

with the operator $\hat{H}$ acting on the basis functions is not periodic under a shift of a reciprocal lattice vector $\mathbf{G}$, but rather transforms [147, 148]

$$\bar{H}(\mathbf{k}+\mathbf{G}) = \mathcal{V}^\dagger(\mathbf{G}) \bar{H}(\mathbf{k}) \mathcal{V}(\mathbf{G}). \tag{A.3}$$

The unitary matrix $\mathcal{V}(\mathbf{G})$ takes into account the momentum-dependence of the different atomic sites at $\mathbf{d}_\alpha$ within each unit cell. The matrix is diagonal with elements $\mathcal{V}_{\alpha\beta}(\mathbf{G}) = e^{-i\mathbf{d}_\alpha\cdot\mathbf{G}}\delta_{\alpha\beta}$.

The benefit of this basis choice is that matrix representations of symmorphic symmetries, such as rotation, are always momentum-independent. For example, a rotation $\hat{R}$ that rotates to $R_n(\mathbf{R}+\mathbf{d}_\alpha) = \mathbf{R}'+\mathbf{d}_\beta$ changes the creation operators of the orbital at $\mathbf{R}+\mathbf{d}_\alpha$ [124]

$$\hat{R}\bar{c}^\dagger_\alpha(\mathbf{R}+\mathbf{d}_\alpha)\hat{R}^{-1} = \bar{c}^\dagger_\beta(\mathbf{R}'+\mathbf{d}_\beta)\mathcal{R}_{\beta\alpha} \tag{A.4}$$

where the unitary matrix $\mathcal{R}_{\alpha\beta}$ accounts for rotation of atomic orbitals, as already used in the main text. This implies for the momentum-space representation of the annihilation operator [148]

$$\hat{R}\bar{c}^\dagger_\alpha(\mathbf{k})\hat{R}^{-1} = \hat{R}\sum_{\mathbf{R}}\bar{c}^\dagger_\alpha(\mathbf{R}+\mathbf{d}_\alpha)e^{i\mathbf{k}\cdot(\mathbf{R}+\mathbf{d}_\alpha)}\hat{R}^{-1} \tag{A.5}$$

$$= \sum_{\mathbf{R}}\bar{c}^\dagger_\beta(\mathbf{R}'+\mathbf{d}_\beta)\mathcal{R}_{\beta\alpha}e^{i\mathbf{k}\cdot(\mathbf{R}+\mathbf{d}_\alpha)}. \tag{A.6}$$

Using $\mathbf{R}+\mathbf{d}_\alpha = R_n^T(\mathbf{R}'+\mathbf{d}_\beta)$ and changing the summation from $\mathbf{R}\to\mathbf{R}'$ gives

$$\hat{R}\bar{c}^\dagger_\alpha(\mathbf{k})\hat{R}^{-1} = \sum_{\mathbf{R}'}\bar{c}^\dagger_\beta(\mathbf{R}'+\mathbf{d}_\beta)e^{i(R_n\mathbf{k})\cdot(\mathbf{R}'+\mathbf{d}_\beta)}\mathcal{R}_{\beta\alpha} \tag{A.7}$$

$$= \bar{c}^\dagger_\beta(R_n\mathbf{k})\mathcal{R}_{\beta\alpha}. \tag{A.8}$$

The Hamiltonian $\hat{H} = \sum_{\mathbf{k}}\bar{c}^\dagger_\alpha(\mathbf{k})\bar{H}_{\alpha\beta}(\mathbf{k})\bar{c}_\beta(\mathbf{k})$ is invariant under the rotation $\hat{R}$, giving [124]

$$\begin{aligned}\hat{R}\hat{H}\hat{R}^{-1} &= \sum_{\mathbf{k}}\bar{c}^\dagger_\alpha(R_n\mathbf{k})\mathcal{R}_{\alpha\alpha'}\bar{H}_{\alpha'\beta'}(\mathbf{k})\mathcal{R}_{\beta\beta'}\bar{c}_\beta(R_n\mathbf{k}) \\ &= \sum_{\mathbf{k}}\bar{c}^\dagger_\alpha(R_n\mathbf{k})\bar{H}_{\alpha\beta}(R_n\mathbf{k})\bar{c}_\beta(R_n\mathbf{k}) = \hat{H}\end{aligned} \tag{A.9}$$

which implies $\mathcal{R}\bar{H}(\mathbf{k})\mathcal{R}^\dagger = \bar{H}(R_n\mathbf{k})$ for the tight-binding Hamiltonian. For superconducting BdG Hamiltonians, the structure of the Nambu spinors needs to be taken into account, which promotes the operator $\mathcal{R}$ to

$$r_n = \begin{pmatrix}\mathcal{R} & \\ & \mathcal{R}^*\end{pmatrix}, \tag{A.10}$$

cf. Eq. (2.2). These operators are always independent of momentum; cf. Ref. [148] for a more general discussion that includes both symmorphic and nonsymmorphic symmetries.

In the main text, we implicitly use a different set of basis functions that gives the tight-binding Hamiltonian

$$H(\mathbf{k}) = \mathcal{V}(\mathbf{k})\bar{H}(\mathbf{k})\mathcal{V}^\dagger(\mathbf{k}). \tag{A.11}$$

This different basis choice has the advantage that the tight-binding Hamiltonian is invariant upon a shift by a reciprocal lattice vector, especially that $\mathcal{H}$ is identical at certain HSPs $\mathbf{\Pi}^{(n)}$ and their rotated counterparts $R_n\mathbf{\Pi}^{(n)}$, e.g., at $\mathbf{M}$ and $R_4\mathbf{M}$ in C_4-symmetric lattices. However, as pointed out in the main text, the operator r_n is generally momentum-dependent, in particular,

$$H(R\mathbf{k}) = \mathcal{V}(R_n\mathbf{k})r_n\mathcal{V}^\dagger(\mathbf{k})H(\mathbf{k})\mathcal{V}(\mathbf{k})r_n^\dagger\mathcal{V}^\dagger(R_n\mathbf{k}) \tag{A.12}$$

$$= r_n'(\mathbf{k})H(\mathbf{k})r_n'^\dagger(\mathbf{k}) \tag{A.13}$$

with $r_n'(\mathbf{k}) = \mathcal{V}(R_n\mathbf{k})r_n\mathcal{V}^\dagger(\mathbf{k})$. We restore Eq. (2.2) when $r_n\mathcal{V}^\dagger(\mathbf{k}) = \mathcal{V}^\dagger(R_n\mathbf{k})r_n$. This relation is only true when each atomic position $\mathbf{d}_\alpha$ is rotated to a (not necessarily different) position $\mathbf{d}_\beta$ *within the same unit cell*. We realize this by computing the action of r_n on $\mathcal{V}^\dagger(\mathbf{k})$ explicitly. The matrix r_n shifts all atomic sites $\mathbf{d}_\alpha \to R_n\mathbf{d}_\alpha$ and transforms the internal degrees of freedom on each $\mathbf{d}_\alpha$ (for example, p_x orbitals are transformed into p_y orbitals under a C_4 rotation). The matrix elements of r_n can thus be written

$$r_n^{\alpha\beta} = \tilde{r}_{\alpha\beta}\delta_{\mathbf{d}_\alpha, R_n\mathbf{d}_\beta}, \tag{A.14}$$

where $\tilde{r}$ transforms the internal degrees of freedom and the Kronecker delta ensures that all sites $\mathbf{d}_\beta$ are changed to $R_n\mathbf{d}_\beta$. Then,

$$\begin{aligned} r_n\mathcal{V}^\dagger(\mathbf{k})\big|_{\alpha\beta} &= \tilde{r}_{\alpha\alpha'}\delta_{\mathbf{d}_\alpha, R_n\mathbf{d}_{\alpha'}}e^{i\mathbf{k}\cdot\mathbf{d}_{\alpha'}}\delta_{\alpha'\beta} = e^{i\mathbf{k}\cdot R_n^T\mathbf{d}_\alpha}\tilde{r}_{\alpha\beta}\delta_{\mathbf{d}_\alpha, R_n\mathbf{d}_\beta} \\ &= e^{i(R_n\mathbf{k})\cdot\mathbf{d}_\alpha}\delta_{\alpha\alpha'}\tilde{r}_{\alpha'\beta}\delta_{\mathbf{d}_{\alpha'}, R_n\mathbf{d}_\beta} = \mathcal{V}^\dagger(R_n\mathbf{k})r_n\big|_{\alpha\beta}, \end{aligned} \tag{A.15}$$

i.e., the operator r_n acting on the tight-binding Hamiltonian $H(\mathbf{k})$ is momentum-independent. This derivation relies on a rotationally invariant unit cell, since each unit cell must contain both atomic positions $\mathbf{d}_\alpha$ and $R\mathbf{d}_\alpha$.

Not every rotationally invariant lattice allows us to define unit cells that respect rotational invariance individually, as we demonstrate using Fig. A.1. The lattice shown in Fig. A.1(a) is C_4-symmetric lattice with four atomic sites in each unit cell. Two different choices of unit cells respect rotational invariance individually and are compatible with a finite system. Similarly, the lattice shown in Fig. A.1(b) and (c) is C_4-symmetric, however, any finite system that respect C_4 symmetry is incompatible with a C_4-symmetric unit cell. While the unit cell in Fig. A.1(b) is rotationally invariant, it contains fractional atomic sites. Any lattice boundary must therefore contain additional partial unit cells. The unit cell choice in Fig. A.1(c) is compatible with a finite system, but the unit cell itself is not C_4-symmetric, such that $\mathbf{d}_\alpha$ and $R\mathbf{d}_\alpha$ are not contained in each unit cell. This gives some additional momentum-dependent

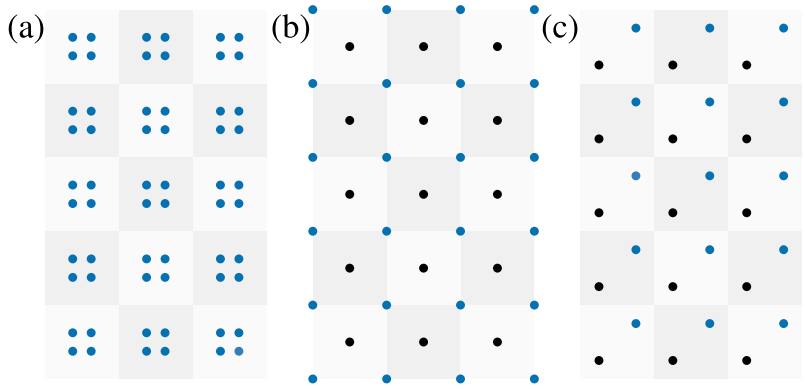

Fig. A.1 Different C_4-symmetric lattices. (a) Each unit cell respects C_4 symmetry individually and is compatible with a finite lattice. (b) Each unit cell respects C_4 symmetry, but contains fractional atomic sites and is therefore incompatible with a finite lattice. (c) For the same lattice as in (b), we can define a different unit cell that is compatible with a finite system, but does not respect C_4 symmetry.

contribution to $r_n'(\mathbf{k}) = \mathcal{V}(R\mathbf{k}) r_n \mathcal{V}^\dagger(\mathbf{k})$, which in turn spoils the bulk classification used in the main text that relies on $[r_n, H(\mathbf{\Pi}^{(n)})] = 0$ [56]. The momentum-dependent contribution is generally model-dependent, such that a classification is beyond the scope of this work.

A.2 Derivation of The Edge Theory

In this Appendix, we show explicitly how each pair of bands in the stack of Dirac Hamiltonians give rise to chiral edge modes, in a description that allows for smooth (on the scale of the lattice spacing) variations of the boundary. We follow a similar prescription to Refs. [46, 37], in which we project onto the low-energy subspace of states localized to the edge of the material. This gives rise to explicit forms of the rotation operator and PH operator on the edge—although overall signs are generally basis-dependent, certain signatures that determine the presence of corner modes are independent of the choice of basis; cf. Appendix A.2.2.

A.2.1 Effective Boundary Hamiltonian

For each Dirac model in the stack, allow the mass term to vary spatially $m_\alpha \to m_\alpha(\mathbf{r})$ and decompose momentum into components parallel and perpendicular to the boundary. For the unit vector $\hat{\mathbf{n}}_\mathbf{r} = (\cos\varphi, \sin\varphi)$ normal to the edge (which varies as a function of position $\mathbf{r}$ along the boundary), decompose $\mathbf{k} = k_\parallel \hat{\mathbf{n}}_\parallel + k_\perp \hat{\mathbf{n}}_\mathbf{r}$ and take $\hat{\mathbf{n}}_\parallel = (-\sin\varphi, \cos\varphi)$ to follow the edge in a counterclockwise direction such that $k_\parallel$ may be positive or negative. (We also define $\mathbf{k}_\parallel = k_\parallel \hat{\mathbf{n}}_\parallel$ for convenience.) Let λ be a coordinate along the edge normal, where $\lambda = 0$

denotes the position of the boundary where $m_\alpha(\lambda = 0) = 0$ changes sign. When a transition is realized through many simultaneous gap closings, all gap closings $m_\alpha(\mathbf{r}) = 0$ happen at the same boundary. In this notation, each Hamiltonian in the stack reads

$$\mathcal{H}^\alpha(\mathbf{k}) = m_\alpha(\lambda)\sigma_3 + v_\alpha \mathbf{k}_\parallel \cdot \boldsymbol{\sigma} - i v_\alpha \hat{\mathbf{n}}_\mathbf{r} \cdot \boldsymbol{\sigma} \partial_\lambda \tag{A.16}$$

with $v_\alpha > 0$ as also used in the main text. In principle, since the normal vectors $\hat{\mathbf{n}}_\mathbf{r}$ and $\hat{\mathbf{n}}_\parallel$ depend on the position $\mathbf{r}$ along the boundary, the momentum operator $\mathbf{k}_\parallel$ does not commute with them. As we only want to consider slowly varying normal vectors, we can neglect this nonzero commutator. Similarly, this approach does not cover sharp changes of the normal vectors [205], which appear directly at the corners of a sample. This does not limit our analysis, as the description away from these sharp changes remains valid and allows to observe differences between smooth edges.

When a mass term changes sign as $\mathrm{sgn}(m_\alpha(\lambda)) = \mathrm{sgn}(\lambda)$ along the transition, chiral modes localized to the edge may be found using the ansatz

$$\Psi_\alpha(\mathbf{k}_\parallel, \lambda) = e^{-\int_0^\lambda d\lambda' m_\alpha(\lambda')/v_\alpha} \psi_\alpha(\mathbf{k}_\parallel). \tag{A.17}$$

Substituting this ansatz into the Hamiltonian, we obtain

$$\left(2m_\alpha(\lambda)\sigma_3 P_+ + v_\alpha \mathbf{k}_\parallel \cdot \boldsymbol{\sigma}\right) \psi_\alpha(\mathbf{k}_\parallel) = E_{\mathbf{k}_\parallel} \psi_\alpha(\mathbf{k}_\parallel), \tag{A.18}$$

with the projector $P_\pm = \frac{1}{2}(1 \pm i\sigma_3 \hat{\mathbf{n}}_\mathbf{r} \cdot \boldsymbol{\sigma}) = \frac{1}{2}(1 \mp \hat{\mathbf{n}}_\parallel \cdot \boldsymbol{\sigma})$. The wave function $\psi_\alpha(\mathbf{k}_\parallel)$ is only a λ-independent solution when $P_+\psi_\alpha(\mathbf{k}_\parallel) = 0$. As $P_+\psi_\alpha(\mathbf{k}_\parallel) = 0$ implies $P_-\psi_\alpha(\mathbf{k}_\parallel) = \psi_\alpha(\mathbf{k}_\parallel)$, the solution satisfies

$$v_\alpha \mathbf{k}_\parallel \cdot \boldsymbol{\sigma} \psi_\alpha(\mathbf{k}_\parallel) = v_\alpha k_\parallel \psi_\alpha(\mathbf{k}_\parallel). \tag{A.19}$$

Had the bulk mass changed in the opposite way as $\mathrm{sgn}(m_\alpha(\lambda)) = -\mathrm{sgn}(\lambda)$, the ansatz would have a different sign in the exponent, and the solutions $P_-\psi_\alpha(\mathbf{k}_\parallel) = 0$ would propagate in the opposite direction.

Here we switch to a more convenient basis, generated by $V_{\mathbf{r}\rightarrow}$ such that

$$V_{\mathbf{r}\rightarrow}^\dagger P_+ V_{\mathbf{r}\rightarrow} = \frac{1}{2}(1 - \sigma_3), \tag{A.20a}$$

$$V_{\mathbf{r}\rightarrow}^\dagger (v_\alpha \mathbf{k}_\parallel \cdot \boldsymbol{\sigma}) V_{\mathbf{r}\rightarrow} = v_\alpha k_\parallel \sigma_3. \tag{A.20b}$$

This can be achieved by choosing $V_{\mathbf{r}\rightarrow} \propto \exp\left(i\frac{\pi}{4}\hat{\mathbf{n}}_\mathbf{r} \cdot \boldsymbol{\sigma}\right)$, where we shall fix this constant of proportionality below using PH symmetry. This allows the 1×1 edge Hamiltonian to be easily procured by applying a projector $p_+ = (1, 0)^T$ to pick out the correct subspace. Explicitly

performing these steps, we end up with a low-energy edge Hamiltonian for right-movers

$$h^{\alpha\rightarrow}_{\mathbf{r},\mathbf{k}} \equiv p_+^T V^\dagger_{\mathbf{r}\rightarrow} \mathcal{H}^\alpha(\mathbf{k}) V_{\mathbf{r}\rightarrow} p_+ \tag{A.21a}$$

$$= v_\alpha k_\parallel. \tag{A.21b}$$

Performing similar steps for left-moving ansätze, differing in the choice of basis $V_{\mathbf{r}\leftarrow}$ and projected component $p_- = (0,1)^T$—though one still has $V_{\mathbf{r}\leftarrow} \propto \exp\left(i\frac{\pi}{4}\hat{\mathbf{n}}_\mathbf{r}\cdot\boldsymbol{\sigma}\right)$—we obtain a similar edge Hamiltonian dispersing with opposite velocity

$$h^{\beta\leftarrow}_{\mathbf{r},\mathbf{k}} \equiv p_-^T V^\dagger_{\mathbf{r}\leftarrow} \mathcal{H}^\beta(\mathbf{k}) V_{\mathbf{r}\leftarrow} p_- \tag{A.22a}$$

$$= -v_\beta k_\parallel. \tag{A.22b}$$

A.2.2 Surface Projections of Rotation Representations

The advantage of the transformation that projects on boundary modes [Eqs. (A.21) and (A.22)] is that it allows to track the transformation of edge modes, as we show in this section. We first discuss how to fix a basis requiring PH symmetry before computing the edge projections of rotation and PH symmetry.

Choice of Basis

The transformation $V_{\mathbf{r}\rightarrow}$ that rotates the projector P_+ into $V^\dagger_{\mathbf{r}\rightarrow} P_+ V_{\mathbf{r}\rightarrow} = \frac{1}{2}(1-\sigma_3)$ is only defined up to a phase, $V_{\mathbf{r}\rightarrow} \propto \exp\left(i\frac{\pi}{4}\hat{\mathbf{n}}_\mathbf{r}\cdot\boldsymbol{\sigma}\right)$. Here, we fix this phase by requiring that the eigenstates $\psi_\alpha(\mathbf{k}) = V_{\mathbf{r}\rightarrow} p_+$ respect PH symmetry, i.e., $\Xi\psi_\alpha(-\mathbf{k}_\parallel) = \psi_\alpha(\mathbf{k}_\parallel)$ with $\Xi = \sigma_1\mathcal{K}$. Further using $p_+ = (1,0)^T$ gives

$$V_{\mathbf{r}\rightarrow} = e^{-i(\pi/4+\varphi/2)} \exp\left(i\frac{\pi}{4}\hat{\mathbf{n}}_\mathbf{r}\cdot\boldsymbol{\sigma}\right). \tag{A.23}$$

Note that this is the same as requiring

$$r_n^\star V_{\mathbf{r}\rightarrow} p_+ = V_{R_n\mathbf{r}\rightarrow} p_+, \tag{A.24}$$

where $r_n^\star = e^{-i\sigma_3\pi/n}$ is the positively signed rotation representation. For left-moving modes, the basis rotation operator is chosen as

$$V_{\mathbf{r}\leftarrow} = e^{-i(\pi/4-\varphi/2)} \exp\left(i\frac{\pi}{4}\hat{\mathbf{n}}_\mathbf{r}\cdot\boldsymbol{\sigma}\right) \tag{A.25}$$

for the same reasons.

Surface Rotation Representations from Bulk

Using the notation introduced above, we show how to derive the edge rotation representation from the bulk representation along the lines of Ref. [37]. For some gap closings, e.g., at $\mathbf{\Gamma}$ and $\mathbf{M}$ in C_4-invariant systems, each Dirac Hamiltonian from the stack respects rotational invariance via $r_n^\alpha \mathcal{H}^\alpha(\mathbf{k}) r_n^{\alpha\dagger} = \mathcal{H}^\alpha(R_n\mathbf{k})$; cf. Eq. (2.23). The edge Hamiltonian for right-moving states, Eq. (A.21), thus transforms as

$$\begin{aligned} h^{\alpha\rightarrow}_{\mathbf{r},\mathbf{k}} =& p_+^T V^\dagger_{\mathbf{r}\rightarrow} \mathcal{H}^\alpha(\mathbf{k}) V_{\mathbf{r}\rightarrow} p_+ \\ =& p_+^T V^\dagger_{\mathbf{r}\rightarrow} r^{\alpha\dagger}_{n,\mathbf{c}} V_{R_n\mathbf{r}\rightarrow} V^\dagger_{R_n\mathbf{r}\rightarrow} \mathcal{H}^\alpha(R_n\mathbf{k}) V_{R_n\mathbf{r}\rightarrow} V^\dagger_{R_n\mathbf{r}\rightarrow} r^\alpha_{n,\mathbf{c}} V_{\mathbf{r}\rightarrow} p_+, \end{aligned} \tag{A.26}$$

where we inserted $1 = V_{R_n\mathbf{r}\rightarrow} V^\dagger_{R_n\mathbf{r}\rightarrow}$. Using that $p_+^T p_+ = 1$ and $[p_+ p_+^T, V^\dagger_{\mathbf{r}\rightarrow} r^{\alpha\dagger}_{n,\mathbf{c}} V_{R_n\mathbf{r}\rightarrow}] = 0$, we obtain

$$\begin{aligned} h^{\alpha\rightarrow}_{\mathbf{r},\mathbf{k}} =& p_+^T p_+ p_+^T V^\dagger_{\mathbf{r}\rightarrow} r^{\alpha\dagger}_{n,\mathbf{c}} V_{R_n\mathbf{r}\rightarrow} V^\dagger_{R_n\mathbf{r}\rightarrow} \mathcal{H}^\alpha(R_n\mathbf{k}) \\ & \times V_{R_n\mathbf{r}\rightarrow} V^\dagger_{R_n\mathbf{r}\rightarrow} r^\alpha_{n,\mathbf{c}} V_{\mathbf{r}\rightarrow} p_+ p_+^T p_+ \\ =& (p_+^T V^\dagger_{\mathbf{r}\rightarrow} r^{\alpha\dagger}_{n,\mathbf{c}} V_{R_n\mathbf{r}\rightarrow} p_+)\, h^{\alpha\rightarrow}_{R_n\mathbf{r},R_n\mathbf{k}}\, (p_+^T V^\dagger_{R_n\mathbf{r}\rightarrow} r^\alpha_{n,\mathbf{c}} V_{\mathbf{r}\rightarrow} p_+) \\ \equiv& u^{\alpha\dagger}_{n,\mathbf{c}}\, h^{\alpha\rightarrow}_{R_n\mathbf{r},R_n\mathbf{k}}\, u^\alpha_{n,\mathbf{c}}. \end{aligned} \tag{A.27}$$

The equivalent result for left-movers is the same with $(+,\rightarrow)$ replaced by $(-,\leftarrow)$. Using Eq. (A.24), we see that $r^\alpha_{n,\mathbf{c}} = \eta_\alpha e^{-i\sigma_3\pi/n}$ implies

$$u^\alpha_{n,\mathbf{c}} = p_+^T V^\dagger_{R_n\mathbf{r}\rightarrow} r^\alpha_{n,\mathbf{c}} V_{\mathbf{r}\rightarrow} p_+ = \eta_\alpha. \tag{A.28}$$

Thus each $u^\alpha_{n,\mathbf{c}}$ is simply a sign. Since the sign itself is basis-dependent, only differences in sign can be of physical importance, as we discussed in the main text.

Other High Symmetry Points

When a Dirac Hamiltonian at a HSP does not transform into itself, but to another HSP under rotation, the rotation representation must account for this. For example, in a C_4-symmetric system, the Dirac Hamiltonian at $\mathbf{X}$ transforms to $\mathbf{X}'$ and vice versa. As discussed in the main text, these Dirac Hamiltonians must be combined into a 4×4 Hamiltonian

$$\mathcal{H}^\oplus(\mathbf{k}) \equiv \mathcal{H}^\alpha_{\mathbf{X}}(\mathbf{k}) \oplus \mathcal{H}^{\alpha+1}_{\mathbf{X}'}(\mathbf{k}). \tag{A.29}$$

Denoting the space of the two stacked Dirac Hamiltonians by τ_μ, two choices of rotation representation are consistent with PH symmetry,

$$r^{\oplus}_{4,\mathbf{c}} = \begin{cases} e^{-i\sigma_3\pi/4} \otimes i\tau_2 \\ e^{-i\sigma_3\pi/4} \otimes \tau_1, \end{cases} \tag{A.30}$$

where we neglect an inconsequential possibility for an overall sign. The projection onto an edge is a straightforward generalization of the approach we discussed above. Both projector $p_\pm$ and basis rotation $V_{\mathbf{r}s_\alpha}$ (with $s_\alpha \in \{\leftarrow, \rightarrow\}$) must be stacked. While the projector is stacked via

$$p_+^T = \begin{pmatrix} 1 & 0 & 0 & 0 \\ 0 & 0 & 1 & 0 \end{pmatrix}, \qquad p_-^T = \begin{pmatrix} 0 & 1 & 0 & 0 \\ 0 & 0 & 0 & 1 \end{pmatrix}, \tag{A.31}$$

where the inner degree of freedom corresponds to the σ_μ space and the outer degree of freedom to the τ_ν space, two choices to stack $V_{\mathbf{r}s_\alpha}$ are consistent with PH symmetry, $V_{\mathbf{r}s_\alpha} \oplus (s_\nu V_{\mathbf{r}s_\alpha})$ with the sign $s_\nu = \pm 1$. The projection $h^{\oplus s_\alpha}_{\mathbf{r},\mathbf{k}}$ of the Hamiltonian onto the edge at $\mathbf{r}$ is thus a 2×2 matrix. As the mass terms at $\mathbf{X}$ and $\mathbf{X}'$ must have the same sign, the two modes of $h^{\oplus s_\alpha}_{\mathbf{r},\mathbf{k}}$ are always copropagating, $h^{\oplus\rightarrow}_{\mathbf{r},\mathbf{k}} = v_\alpha k_\parallel \tau_0$ and $h^{\oplus\leftarrow}_{\mathbf{r},\mathbf{k}} = -v_\alpha k_\parallel \tau_0$.

Following the derivation in Sec. A.2.2, the resulting representation of the rotation on the edge is

$$u^{\alpha}_{4,\mathbf{c}} = \begin{cases} s_\nu i\tau_2 & \text{for } r^{\oplus}_{4,\mathbf{c}} = e^{-i\sigma_3\pi/4} \otimes i\tau_2 \\ s_\nu \tau_1 & \text{for } r^{\oplus}_{4,\mathbf{c}} = e^{-i\sigma_3\pi/4} \otimes \tau_1. \end{cases} \tag{A.32}$$

Since the overall sign s_ν does not change $\det u^{\alpha}_{4,\mathbf{c}} = \pm 1$, it can be safely neglected as we do in the main text.

A.2.3 Edge Projection of Particle-Hole Operator

Since the phase of the chiral edge modes $\psi_\alpha(\mathbf{k}_\parallel)$ is chosen such these states respect bulk PH symmetry, the edge projection of PH symmetry simply becomes complex conjugation. We realize this by writing the edge Hamiltonian in second-quantized notation for a position $\mathbf{r}$ on the boundary

$$\hat{h}_{\mathbf{r}} = \sum_{\mathbf{k}_\parallel,\alpha\beta} \hat{\gamma}^\dagger_\alpha(\mathbf{k}_\parallel)\, h^{\alpha\beta}_{\mathbf{r},\mathbf{k}_\parallel}\, \hat{\gamma}_\beta(\mathbf{k}_\parallel) \tag{A.33}$$

with operators $\hat{\gamma}_\alpha(\mathbf{k}_\parallel) = \psi^*_\alpha(\mathbf{k}_\parallel) \cdot \hat{\xi}_\alpha(\mathbf{k}_\parallel)$ and the Nambu spinor $\hat{\xi}_\alpha(\mathbf{k}) = (\hat{c}_\alpha(\mathbf{k}), \hat{c}^\dagger_\alpha(-\mathbf{k}))$. As the wave function respects PH symmetry, $\psi^*_\alpha(\mathbf{k}_\parallel) = \sigma_x \psi_\alpha(-\mathbf{k}_\parallel)$, we realize that the

annihilation operator $\hat{\gamma}_\alpha(\mathbf{k}_\parallel)$ equals the corresponding creation operator at its negative momentum,

$$\hat{\gamma}_\alpha(\mathbf{k}_\parallel) = \psi_\alpha(-\mathbf{k}_\parallel) \cdot (\sigma_x \hat{\xi}_\alpha(\mathbf{k}_\parallel)) = \psi_\alpha(-\mathbf{k}_\parallel) \cdot \hat{\xi}^\dagger_\alpha(-\mathbf{k}_\parallel) \tag{A.34}$$

$$= \hat{\gamma}^\dagger_\alpha(-\mathbf{k}_\parallel), \tag{A.35}$$

where we used that $\sigma_x \hat{\xi}_\alpha(\mathbf{k}) = \hat{\xi}^\dagger_\alpha(-\mathbf{k})$. This implies that the $\hat{\gamma}_\alpha(\mathbf{k}_\parallel)$ are in fact (Fourier-transformed) Majorana fields. Further using $\mathrm{Tr}\left[h_{\mathbf{r},\mathbf{k}_\parallel=\mathbf{0}}\right] = 0$, the second-quantized Hamiltonian reads

$$\hat{h}_\mathbf{r} = -\sum_{\mathbf{k}_\parallel,\alpha\beta} \hat{\gamma}^\dagger_\alpha(\mathbf{k}_\parallel) h^{\beta\alpha}_{\mathbf{r},-\mathbf{k}} \hat{\gamma}_\beta(\mathbf{k}_\parallel). \tag{A.36}$$

This implies that $h^{\beta\alpha}_{\mathbf{r},-\mathbf{k}_\parallel} = -h^{\alpha\beta}_{\mathbf{r},\mathbf{k}_\parallel}$, or using the Hermiticity of $h_{\mathbf{r},\mathbf{k}_\parallel}$, that

$$h_{\mathbf{r},\mathbf{k}_\parallel} = -\mathcal{K} h_{\mathbf{r},-\mathbf{k}_\parallel} \mathcal{K}, \tag{A.37}$$

i.e., PH symmetry simply reduces to complex conjugation when projected to an edge.

Appendix B

Additional Proofs about The Fermionic Determinant

B.1 Jackiw-Rebbi Derivation of Edge Mode Spectrum

In this Appendix, we derive the edge mode spectrum associated with an instanton using a Jackiw-Rebbi-like ansatz [31]. We shall use the momentum-space representation $\mathcal{H}_\phi(k)$ of the 1D model [Eq. (3.1)] to write the Lagrangian

$$\mathcal{L}(\tau,k) = \partial_\tau + \mathcal{H}_{\phi_\tau}(k). \tag{B.1}$$

Recall that a sign change of $\cos\phi_\tau$ corresponds to a topological phase transition of $\mathcal{H}_{\phi_\tau}(k)$. As in the main text, we consider the Hermitian Hamiltonian $\tilde{\mathcal{H}}(\tau,k) = i\sigma_1\mathcal{L}(\tau,k)$.

We deal solely with the case of unequal gaps on both sides of the transition because this encompasses the case of equal gaps. To this end, we modify the gap at $\phi = 0$ as $\Delta \to \Delta' = \eta\Delta$, where $\eta \in (0,1]$ is a parameter describing the asymmetry of the gap. Separating out the ϕ_τ dependence, the Hermitian Hamiltonian is now

$$\begin{aligned}\tilde{\mathcal{H}}(\tau,k) =& \frac{\Delta}{2}\cos\phi_\tau\left[(\eta+\cos k)\,\sigma_2 - \sin k\,\sigma_3\right] \\ &+ \frac{\Delta}{2}\left[(\eta-\cos k)\,\sigma_2 + \sin k\,\sigma_3\right] + i\partial_\tau\sigma_1.\end{aligned} \tag{B.2}$$

Suppose that there is an instanton located at τ_0 which closes the gap: $\cos\phi_{\tau<\tau_0} > 0$ and $\cos\phi_{\tau>\tau_0} < 0$. One might propose an ansatz

$$\Psi(k,\tau) \stackrel{?}{=} \exp\left[\Delta\cos(k/2)\int_{\tau_0}^{\tau} d\tau'\cos\phi_{\tau'}\right]\psi_k \tag{B.3}$$

localized at τ_0, where the sign change of $\cos\phi_\tau$ ensures that the solution remains normalizable on both sides of the transition. Such an ansatz fails for $\eta \neq 1$ because the decay of the bound state needs to be different in regions with a different gap [206, 207]. We therefore try a judicious rewriting of the Hamiltonian (B.2) that immediately suggests a better ansatz, namely

$$\begin{aligned}\tilde{\mathcal{H}} =& i\partial_\tau\sigma_1 + \frac{\Delta}{2}(\alpha_k + \cos\phi_\tau)\left[(\eta+\cos k)\,\sigma_2 - \sin k\sigma_3\right] \\ &+\frac{\Delta}{2}\left[(\eta(1-\alpha_k) - (1+\alpha_k)\cos k)\,\sigma_2 + (1+\alpha_k)\sin k\sigma_3\right],\end{aligned} \tag{B.4}$$

where we introduce a parameter α_k to label the reshuffling. We will soon see that only one choice of α_k makes the ansatz work. This new form suggests the ansatz

$$\Psi = \exp\left[\frac{\Delta}{2}\sqrt{1+\eta^2+2\eta\cos k}\int_{\tau_0}^{\tau} d\tau'(\alpha_k+\cos\phi_{\tau'})\right]\psi_k \tag{B.5}$$

that factorizes the Hamiltonian as

$$\tilde{\mathcal{H}}\psi_k = \left[i\Delta(\alpha_k+\cos\phi_\tau)\sqrt{1+\eta^2+2\eta\cos k}\sigma_1 Q_k + h_k\right]\psi_k. \tag{B.6}$$

with the projector

$$Q_k = \frac{1}{2}\left[\sigma_0 + \frac{(\eta+\cos k)\,\sigma_3 + \sin k\sigma_2}{\sqrt{1+\eta^2+2\eta\cos k}}\right] = Q_k^2, \tag{B.7}$$

and the τ-independent term

$$h_k = \frac{\Delta}{2}\left[(\eta(1-\alpha_k) - (1+\alpha_k)\cos k)\,\sigma_2 + (1+\alpha_k)\sin k\sigma_3\right]. \tag{B.8}$$

To get τ-independent solutions we project onto the $Q_k\psi_k^+ = 0$ subspace in which the Hamiltonian is simply $\tilde{\mathcal{H}}\psi_k^+ = h_k\psi_k^+$. For this to be valid, we need ψ_k^+ to be a simultaneous eigenstate of both the projector and the remaining effective Hamiltonian, i.e. $[Q_k, h_k] = 0$, which holds if

$$\alpha_k = \frac{\eta^2-1}{1+\eta^2+2\eta\cos k}. \tag{B.9}$$

A crucial observation is that α_k monotonically decreases from $\alpha_{k=0} = (\eta-1)/(\eta+1)$ to $\alpha_{k=\pi} = (\eta+1)/(\eta-1)$, which means that there exists a range of k for which $\alpha_k < -1$ and the ansatz of Eq. (B.5) is no longer normalizable. Thus bound states only exist in the range $|k| \leq \arccos(-\eta)$, for which the dispersion is given by

$$E_\parallel^\pm(k) = \frac{\Delta}{2}\sqrt{(1+\alpha_k)^2 + \eta^2(1-\alpha_k)^2 - 2\eta(1-\alpha_k^2)\cos k}, \tag{B.10}$$

saturating at the value of the reduced gap $\Delta' = \eta\Delta$. Setting $\eta = 1$ recovers the equal gap case, which has bound states for all k with simple dispersion

$$E_{\parallel}^{\pm}(k) = \Delta \sin(k/2) \tag{B.11}$$

quoted in the main text. We have thus derived the spectrum of the chiral edge mode along the spatial direction, bound to each instanton. Had $\cos\phi_\tau$ changed sign in the opposite direction (as for an anti-instanton), the ansatz in Eq. (B.5) would need a minus sign in the exponent to be normalizable, and we would have derived an edge mode of opposite chirality.

Recall from Sec. 3.4.1 that for the OBC case to have symmetric wells, one tunes the gap inequality parameter to be $\eta = 1 - \frac{1}{L}$, which we may substitute into the above expressions to find the chiral edge mode spectrum associated with each instanton.

B.2 Proof that Fermions Guarantee Suppression

In this appendix we prove that the effect of eigenstate evolution is always to suppress tunnelling. We will do this by showing that the fermionic potential $\tilde{U}_{\mathrm{f}}[\phi_\tau]$ is always greater than or equal to its naïve equivalent $\tilde{U}_{\mathrm{n}}[\phi_\tau]$. Recall from Eq. (3.36) in the main text that the primary object of interest is the time ordered exponential, which we can express as the $\Delta\tau = \frac{\beta}{N} \to 0$ continuum limit of the product

$$\mathsf{M} \equiv \mathcal{T}\exp\left[-\int_0^\beta d\tau\, \mathcal{H}_{\phi_\tau}\right] = e^{-\mathcal{H}_{\phi_N}\Delta\tau} e^{-\mathcal{H}_{\phi_{N-1}}\Delta\tau} \cdots e^{-\mathcal{H}_{\phi_2}\Delta\tau} e^{-\mathcal{H}_{\phi_1}\Delta\tau}. \tag{B.12}$$

The fermionic potential follows from the eigenvalues $\rho_m(\mathsf{M})$ of this $2L \times 2L$ matrix M. Specifically, we want to consider the magnitude of

$$\left|\exp\left\{-2\tilde{U}_{\mathrm{f}}[\phi_\tau]\right\}\right| = 2^{-2L}\prod_m \left|\sqrt{\rho_m(\mathsf{M})} + \frac{1}{\sqrt{\rho_m(\mathsf{M})}}\right| \leq 2^{-2L}\prod_m \left(\sqrt{|\rho_m(\mathsf{M})|} + \frac{1}{\sqrt{|\rho_m(\mathsf{M})|}}\right), \tag{B.13}$$

where the right-hand side follows from the triangle inequality. We also recognise that the naïve potential follows the same calculation but with the Hamiltonians replaced by only their spectral parts: $\mathcal{H}_{\phi_\tau} \to \oplus_m \varepsilon^+_{\phi_\tau,m}\sigma_3$. Let the corresponding naive product be labelled M_{n}, noting that it is much easier to calculate because each matrix in the product commutes.

We start by getting an inequality for the eigenvalues in the fermionic and naïve cases. Let M's eigenvalues $\rho_m(\mathsf{M})$ be nonincreasingly ordered as $|\rho_1(\mathsf{M})| \geq \cdots \geq |\rho_{2L}(\mathsf{M})|$, and let its

singular values[1] $\sigma_m(\mathsf{M})$ be ordered similarly as $\sigma_1(\mathsf{M}) \geq \cdots \geq \sigma_{2L}(\mathsf{M})$. The first step is to invoke Weyl's inequality:

$$\prod_{m=1}^{k} |\rho_m(\mathsf{M})| \leq \prod_{m=1}^{k} \sigma_m(\mathsf{M}), \tag{B.14}$$

for $k = 1, 2, \ldots, 2L$. For generic complex matrices $\mathsf{A}, \mathsf{B} \in \mathbb{C}^{2L\times 2L}$, there also holds an inequality between the singular values of products of matrices:

$$\prod_{m=1}^{k} \sigma_m(\mathsf{AB}) \leq \prod_{m=1}^{k} \sigma_m(\mathsf{A})\,\sigma_m(\mathsf{B}). \tag{B.15}$$

We can use Eqs. (B.14) and (B.15) recursively on the product definition Eq. (B.12) to conclude that

$$\prod_{m=1}^{k} |\rho_m(\mathsf{M})| \leq \prod_{m=1}^{k}\prod_{i=1}^{N} \sigma_m(\exp\{-\mathcal{H}_{\phi_i}\Delta\tau\}) = \prod_{m=1}^{k}\prod_{i=1}^{N} \exp\{\varepsilon_{\phi_i,m}\Delta\tau\}, \tag{B.16}$$

where the last equality follows because each time-slice contains a positive definite Hermitian matrix (and we order energies as $\varepsilon_{\phi,1} \geq \cdots \geq \varepsilon_{\phi,2L}$). We may recognise the right-hand side as the eigenvalues of the naïve product M_n, therefore

$$\prod_{m=1}^{k} |\rho_m(\mathsf{M})| \leq \prod_{m=1}^{k} \rho_m(\mathsf{M}_\mathrm{n}). \tag{B.17}$$

By PH symmetry, $\rho_m(\mathsf{M}) = [\rho_{2L-m+1}(\mathsf{M})]^{-1}$, we also have

$$\prod_{m=1}^{2L} |\rho_m(\mathsf{M})| = \prod_{m=1}^{2L} \rho_m(\mathsf{M}_\mathrm{n}) = 1. \tag{B.18}$$

We can therefore say that the ordered vector $\mathbf{n} = [\log\rho_1(\mathsf{M}_\mathrm{n}), \ldots, \log\rho_{2L}(\mathsf{M}_\mathrm{n})]$ *majorises* the ordered vector $\mathbf{f} = [\log|\rho_1(\mathsf{M})|, \ldots, \log|\rho_{2L}(\mathsf{M})|]$, written $\mathbf{f} \prec \mathbf{n}$.

Next, we aim to show, using convex analysis, that an inequality for the fermionic and naive potentials follows from the majorisation relation between these vectors. Consider a function $u(\mathbf{x})$ on real vectors $\mathbf{x} \in \mathbb{R}^d$. Such a function is called *Schur-convex* if an inequality follows from majorisation of its argument, i.e.,

$$u(\mathbf{x}) \quad \text{is Schur-convex iff} \quad \mathbf{x} \prec \mathbf{y} \implies u(\mathbf{x}) \leq u(\mathbf{y}). \tag{B.19}$$

[1] Recall that singular values are given by $\sigma(\mathsf{A}) = \sqrt{\rho(\mathsf{A}^\dagger\mathsf{A})}$.

According to the Schur-Ostrowski condition, $u(\mathbf{x})$ is Schur-convex if and only if

$$(x_m - x_n)\left(\frac{\partial u}{\partial x_m} - \frac{\partial u}{\partial x_n}\right) \geq 0 \qquad \forall \mathbf{x} \in \mathbb{R}^d. \tag{B.20}$$

Now specify the function to be $u(\mathbf{x}) = \prod_{m=1}^{2L} \cosh[x_m/2]$, in which case we can verify that

$$(x_m - x_n)\left(\frac{\partial u}{\partial x_m} - \frac{\partial u}{\partial x_n}\right) = \frac{1}{2}(x_m - x_n)\sinh\left[\frac{1}{2}(x_m - x_n)\right]\prod_{l\neq m,n}\cosh\left[\frac{1}{2}x_l\right] \geq 0, \tag{B.21}$$

so $u(\mathbf{x})$ is Schur-convex. We selected this form of $u(\mathbf{x})$ because, by Eq. (B.13), $u(\mathbf{n}) = \exp\{-2\tilde{U}_\mathrm{n}[\phi_\tau]\}$ and $u(\mathbf{f}) = \exp\{-2\,\mathrm{Re}\,\tilde{U}_\mathrm{f}[\phi_\tau]\}$. Using the majorisation relation $\mathbf{f} \prec \mathbf{n}$ we have already proven and Schur-convexity, we therefore have $u(\mathbf{f}) \leq u(\mathbf{n})$ and

$$\mathrm{Re}\,\tilde{U}_\mathrm{f}[\phi_\tau] \geq \tilde{U}_\mathrm{n}[\phi_\tau]. \tag{B.22}$$

That is, the real part of the fermionic potential is provably greater than or equal to the naïve potential. (For the chiral symmetric case in the main text, where we calculated $\tilde{U}_\mathrm{f}[\phi_\tau]$ from the spectrum of a Hermitian Hamiltonian, we can further choose $\tilde{U}_\mathrm{f}[\phi_\tau]$ to be real.) Thus, including fermions properly always suppresses the tunnelling amplitude compared to the naïve calculation.